

**NUMERICAL COMPUTATION OF THE
FLOW AND HEAT TRANSFER OVER TWO
ROTATING CIRCULAR CYLINDERS**

Jakgrit Sompong

**A Thesis Submitted in Partial Fulfillment of the Requirements for the
Degree of Doctor of Philosophy in Applied Mathematics
Suranaree University of Technology
Academic Year 2008**

การคำนวณเชิงตัวเลขของการไหลและการถ่ายเทความร้อน
ผ่านทรงกระบอกกลมที่กำลังหมุนสองแท่ง

นายจักรกฤษณ์ สมพงษ์

วิทยานิพนธ์นี้เป็นส่วนหนึ่งของการศึกษาตามหลักสูตรปริญญาวิทยาศาสตรดุษฎีบัณฑิต
สาขาวิชาคณิตศาสตร์ประยุกต์
มหาวิทยาลัยเทคโนโลยีสุรนารี
ปีการศึกษา 2551

**NUMERICAL COMPUTATION OF THE FLOW AND
HEAT TRANSFER OVER TWO ROTATING
CIRCULAR CYLINDERS**

Suranaree University of Technology has approved this thesis submitted in partial fulfillment of the requirements for a Doctoral Degree.

Thesis Examining Committee

(Assoc. Prof. Dr. Prapasri Asawakun)

Chairperson

(Assoc. Prof. Dr. Nikolay Moshkin)

Member (Thesis Advisor)

(Prof. Dr. Sergey Meleshko)

Member

(Asst. Prof. Dr. Eckart Schulz)

Member

(Assoc. Prof. Dr. Ekachai Juntasaro)

Member

(Prof. Dr. Pairote Sattayatham)

Vice Rector for Academic Affairs

(Assoc. Prof. Dr. Prapan Manyum)

Dean of Institute of Science

จักรกฤษณ์ สมพงษ์ : การคำนวณเชิงตัวเลขของการไหลและการถ่ายเทความร้อนผ่าน
ทรงกระบอกกลมที่กำลังหมุนสองแท่ง (NUMERICAL COMPUTATION OF THE
FLOW AND HEAT TRANSFER OVER TWO ROTATING CIRCULAR CYLINDERS)
อาจารย์ที่ปรึกษา : รองศาสตราจารย์ ดร.นิโกลัสน์ มอสกิน, 99 หน้า.

งานวิจัยนี้ศึกษาการไหลของของไหลแบบสมมาตรที่มีความหนืดแบบไม่ยุบตัวและการถ่ายเทความร้อนโดยการพาความร้อนแบบบังคับผ่านทรงกระบอกกลมซึ่งกำลังหมุนสองแท่งด้วยการเรียงตัวแบบเคียงข้างกัน ค่าคงที่ของความเร็วเชิงมุมและอุณหภูมิภายในทรงกระบอกถูกนำมาพิจารณา ผลเฉลยเชิงตัวเลขได้มาโดยพิกัดทรงกระบอกสองขั้ว วิธีผลต่างอันดับถูกนำมาใช้เพื่อให้สมการแบบจำลองเชิงคณิตศาสตร์เป็นวิฤตซึ่งอยู่ในรูปของตัวแปรปฐมฐาน เราได้ตรวจสอบความถูกต้องขั้นต้นวิธีเชิงตัวเลขโดยการเปรียบเทียบผลเฉลยเชิงตัวเลขของเรากับข้อมูลจากห้องปฏิบัติการจำลองทางฟิสิกส์และผลเฉลยเชิงตัวเลขอื่นๆ ที่ทำได้ และอิทธิพลของตัวแปรเสริมในแบบจำลองของการไหลและการถ่ายเทความร้อนได้แก่ เลขเรย์โนลด์ส์ เลขพรันด์เทิล อัตราเร็วของการหมุนทรงกระบอกและช่องห่างระหว่างทรงกระบอกกลมได้ถูกนำเสนอ

สาขาวิชาคณิตศาสตร์
ปีการศึกษา 2551

ลายมือชื่อนักศึกษา _____
ลายมือชื่ออาจารย์ที่ปรึกษา _____

JAKGRIT SOMPONG : NUMERICAL COMPUTATION OF THE
FLOW AND HEAT TRANSFER OVER TWO ROTATING CIRCULAR
CYLINDERS. THESIS ADVISOR : ASSOC. PROF. NIKOLAY
MOSHKIN, Ph.D. 99 PP.

VISCOUS INCOMPRESSIBLE FLUID/ HEAT TRANSFER/ BIPOLAR
CYLINDRICAL COORDINATES/ FINITE DIFFERENCE METHOD.

The present study numerically investigates the steady, viscous incompressible fluid flow and forced convection heat transfer over two rotating circular cylinders in side-by-side arrangement. The constant angular velocity and the constant temperature inside the cylinders are considered. Numerical solutions in bipolar cylindrical coordinates are obtained. The finite difference method is used to discretize the equations of the mathematical model in terms of primitive variables. The numerical algorithm has been verified by comparing our numerical results with available data from laboratory physical modeling and other numerical results. The influence of the model parameters such as Reynolds number (Re), Prandtl number (Pr), rotational speed of cylinders and gap spacing between circular cylinders on the flow and heat transfer are presented.

School of Mathematics

Academic Year 2008

Student's Signature_____

Advisor's Signature_____

ACKNOWLEDGEMENTS

I am profoundly grateful to my thesis advisor Assoc. Prof. Dr. Nikolay Moshkin for his support, patient help and offering many useful suggestions.

I would like to acknowledge all the lecturers who taught and helped me during the course of studies at Suranaree University of Technology. They are Assoc. Prof. Dr. Prapasri Asawakun, Prof. Dr. Sergey Meleshko and Asst. Prof. Dr. Eckart Schulz.

I also would like to express my appreciation to Assoc. Prof. Dr. Ekachai Juntasaro and Assoc. Prof. Dr. Varangrat Juntasaro for their valuable discussions and comments.

I would like to express my appreciation to all who have helped me. These include Asst. Prof. Dr. Jessada Tanthanuch and all of my friends at Suranaree University of Technology.

I acknowledge the financial support of the Ministry of University Affairs of Thailand (MUA). I am indebted to Department of Mathematics, Naresuan University for grants to support my studies throughout.

Finally, I am deeply grateful to my parents and my brother for support, understanding encouragement, and love.

Jakgrit Sompong

CONTENTS

	Page
ABSTRACT IN THAI	II
ABSTRACT IN ENGLISH	III
ACKNOWLEDGEMENTS	IV
CONTENTS	V
LIST OF TABLES	VII
LIST OF FIGURES	VIII
 CHAPTER	
I INTRODUCTION	1
II MATHEMATICAL FORMULATION OF PROBLEM	7
2.1 Physical assumptions	7
2.2 Basic equations	8
2.3 Boundary condition	12
2.4 Drag and lift coefficients	12
2.5 Heat Transfer (Nusselt number)	14
III NUMERICAL METHODS	18
3.1 Transformation of the governing equations	18
3.2 Discretization of the governing equations	21
3.2.1 Description of grid	21
3.2.2 Discretization of Navier-Stokes equations	21
3.3 Discretization of the energy equation	33

CONTENTS (Continued)

	Page
3.4 Computation of flow characteristics	38
3.4.1 Drag and lift coefficients	38
3.4.2 Vorticity on the cylinder surfaces	39
3.4.3 Nusselt number	39
IV VALIDATION	41
4.1 Characteristics of flow and heat transfer over two circular cylinders without rotation in large gap spacing	42
4.2 Characteristics of flow and heat transfer over two rotating circular cylinders in large gap spacing	54
V NUMERICAL RESULTS	58
5.1 Effect of gap spacing (zero rotation)	58
5.2 Large gap spacing (effect of rotation)	60
5.3 Small gap spacing ($g \lesssim 3$) and non zero rate of rotation	65
VI CONCLUSIONS	82
REFERENCES	85
APPENDICES	
APPENDIX A THE ELIMINATION METHOD FOR THREE- POINT EQUATIONS	92
APPENDIX B THE CYCLIC ELIMINATION METHOD	96
CURRICULUM VITAE	100

LIST OF TABLES

Table		Page
4.1	Validation of the numerical algorithm; comparison study for flow over two side-by-side circular cylinders at $g = 14$ with flow over a single cylinder.	44
4.2	Validations of the numerical algorithm; comparison study for flow over two side-by-side circular cylinder at $g = 14$ with flow over a single cylinder.	45
4.3	Effect of grid refinement upon C_D , C_{D_p} , C_{D_f} , and average Nusselt number Nu for $Re = 20$ and $g = 14$	46
4.4	Comparison of the average Nusselt number at $Pr = 0.7$, $g = 14$, $\alpha = 0$ for grid 21×21 , 41×41 , and 81×81 with the values found in the literature.	49
4.5	Comparison of the average Nusselt numbers for cylinders with constant temperature for $g = 14$	50
4.6	Hydrodynamic parameters of flow over a rotating circular cylinder at $Re = 20$ with $g = 14$	57
5.1	Variation of the average Nusselt number at $Re = 20$ and $\alpha = 0$. . .	61
5.2	Variation of average Nusselt number at $g = 14$	64
5.3	Variation of average Nusselt number at $g = 2$	71
5.4	Variation of average Nusselt number at $g = 1$	77

LIST OF FIGURES

Figure		Page
2.1	Schematics of problem.	9
2.2	Convective heat transfer from a surface.	15
3.1	Sketch of the meshes in physical and computational domain.	19
3.2	Staggered arrangement of v , u , p and T	22
3.3	The location of known velocity field at the infinity boundary.	27
3.4	The flow chart of the numerical algorithm.	30
3.5	The structure of velocity in ξ -direction that used for compute $\frac{\partial v}{\partial \eta}$ on the left and right boundary.	32
3.6	The cell at far boundary.	34
3.7	Location grid of temperature.	36
3.8	Structure of grid: using compute force acting on cylinders surface.	39
4.1	(a) Pressure coefficient over cylinder surface, (b) the vorticity distribution over cylinder surface, for the left cylinder at $Re =$ 20 , 40 , and $g = 14$	43
4.2	1^{st} -column: Streamline patterns, 2^{nd} -column: pressure fields of flow over two circular cylinders for $g = 14$, $\alpha = 0$ at 1^{st} -row: $Re = 20$, 2^{nd} -row: $Re = 40$	47
4.3	The temperature contours for 1^{st} -column: $Re = 20$ and 2^{nd} -column: $Re = 40$ of flow over two circular cylinders for $g = 14$, $\alpha = 0$ at 1^{st} -row: $Pr = 1$, 2^{nd} -row: $Pr = 10$, and 3^{rd} -row: $Pr = 20$	48

LIST OF FIGURES (Continued)

Figure		Page
4.4	Colburn j-factor as a function of the Reynolds number at different Prandtl number.	51
4.5	Colburn j-factor as a function of the Reynolds number at different Prandtl number.	52
4.6	Local Nusselt number variation on the surface of the circular cylinders for $\alpha = 0$, $g = 14$, and (a) $Re = 10$, (b) $Re = 20$, (c) $Re = 40$ at various Prandtl numbers.	53
4.7	Local Nusselt number variation on the surface of the circular cylinders at $Pr = 1$, $g = 14$ at various Reynolds numbers.	54
4.8	Local Nusselt number on the sequence of grids for $Re = 20$, $g = 14$, and $Pr = 1$	55
4.9	(a-b) Streamline patterns, (c-d) pressure fields and (e-f) temperature contours of flow over two circular cylinders at $Re = 20$, $g = 14$, and $Pr = 1.0$, left column: $\alpha = 0.1$, right column: $\alpha = 1.0$	56
5.1	Local Nusselt number for different gap spacing at $Re = 20$, $\alpha = 0$, and (a) $Pr = 0.7$, (b) $Pr = 1$, (c) $Pr = 10$, and (d) $Pr = 20$	60
5.2	Average Nusselt number for different gap spacing at $Re = 20$, $\alpha = 0$	61
5.3	Local Nusselt number variation on the surface of the circular cylinders at $Re = 20$, $g = 14$, $\alpha = 0, 0.1, 0.5, 1$, and 2 for (a) $Pr = 0.7$, (b) $Pr = 1$, (c) $Pr = 10$, and (d) $Pr = 20$	63
5.4	Streamline patterns at $Re = 20$, $g = 14$, $\alpha = 0.1, 1.0$, and 2.0 , and for $Pr = 1$	65

LIST OF FIGURES (Continued)

Figure		Page
5.5	Temperature contours over two circular cylinders at $Re = 20$, $g = 14$, $\alpha = 0.1, 1.0, 2.0$, and for $Pr = 1, 10$, and 20	66
5.6	Nusselt number at (a) $Re = 10$, (b) $Re = 20$, and (c) $Re = 40$, and $g = 14$ for different Prandtl number Pr	67
5.7	Local Nusselt number at $Re = 20$, $\alpha = 1$, and (a) $Pr = 1$, (b) $Pr = 5$, (c) $Pr = 10$, and (d) $Pr = 20$	69
5.8	Streamline patterns (left column) and temperature contours (right column) of flow over two circular cylinders at $Re = 20$, $\alpha = 1$, and $g = 1$ - first row, $g = 2$ - second row, $g = 3$ - third row, $g = 4$ - fourth row, and $g = 5$ - fifth row.	70
5.9	Local Nusselt number at $Re = 20$, $\alpha = 1$, and (a) $g = 1$, (b) $g = 2$, (c) $g = 3$, and (d) $g = 4$	72
5.10	Nusselt number at (a) $Re = 10$, (b) $Re = 20$, and (c) $Re = 40$, and $g = 2$ for different Prandtl number Pr	73
5.11	Local Nusselt number variation on the surface of the circular cylinders at $Pr = 1$, $g = 1$, $\alpha = 0, 0.5, 1, 1.5, 2$, and 2.5 for (a) $Re = 10$, (b) $Re = 20$, and (c) $Re = 40$	75
5.12	Streamlines contours over two circular cylinders at $Re = 10$ (left column), and $Re = 20$ (right column), $Pr = 1$, $g = 1$, and $\alpha = 0.5, 1.0, 1.5$, and 2.0	78
5.13	Temperature contours over two circular cylinders at $Re = 10$, $g = 1$, $Pr = 1, 10, 20$, and $\alpha = 0.5, 1.0, 1.5$, and 2.0	79

LIST OF FIGURES (Continued)

Figure		Page
5.14	Temperature contours over two circular cylinders at $Re = 20$, $g =$ 1, $Pr = 1, 10, 20$, and $\alpha = 0.5, 1.0, 1.5$, and 2.0	80
5.15	Nusselt number at (a) $Re = 10$, (b) $Re = 20$, and (c) $Re = 40$, and $g = 1$ for different Prandtl number Pr	81

CHAPTER I

INTRODUCTION

The flow of fluids and forced convection across a heated bluff body has been the subject of considerable research interest because of its relevance in many engineering applications. The flow past a cylinder is considered to be an ideal bluff body to study the important phenomena of heat and mass transfer. For instance, the knowledge of the hydrodynamic forces experienced by submerged cylindrical objects such as off-shore pipelines is essential for the design of such structures. On the other hand because of changing process and climatic conditions, one also needs to determine the rate of heat transfer from such structures. Industrial processes where heat and mass transfer from an isolated cylinder plays an important role include anemometry and chemical or radioactive contamination/purification, glass cooling, plastic and industrial devices and many other processes. Because of the importance of these applications, there has been a great deal of interest in the fluid flow and the heat transfer across a single cylinder from the experimental, analytical and numerical approaches (e.g. Bharti *et al.* (2007), Soares *et al.* (2005), see also excellent the reviews Morgan (1975), Lange *et al.* (1998), and Zdravkovich (1997, 2003))

Heat transfer and fluid flow around a single rotating cylinder has been studied by several researchers, see for example the recent work of Mahfouz (1999a, 1999b), Kang (1999), Badr (1989), Stojković (2002), Gshwendtner (2004), and Mittal (2003). The flow around two stationary or rotating circular cylinders can be considered as an elementary flow which is helpful to understanding the

flow patterns and hydrodynamic characteristics around multiple bluff bodies in engineering practice. The arrangement of the cylinders with respect to the free stream flow direction can be

- tandem (or in-line): the free stream flow direction is parallel with the line of the centers of the cylinders;
- transverse (or side-by-side): the free stream flow direction is perpendicular to the line of the cylinders centers;
- staggered.

The incompressible flow around pairs of circular cylinders in tandem arrangements was investigated in many papers. Many previous investigations have revealed complex flow behavior, different flow patterns and wake interferences depending upon the relative positioning of the two cylinders. For example, in a series of work by Juncu (2007a, 2007b), a numerical study of natural and forced convection heat transfer around two tandem circular cylinders at low Reynolds numbers is presented. The steady flow of incompressible power-law fluids over a pair of cylinders in tandem arrangement has been studied numerically by Patil *et al.* (2008). The governing equations have been solved using a finite volume method based solver (Fluent 6.2). In particular, the effect of the power-law index ($0.4 \leq n \leq 1.8$), Reynolds number ($1 \leq Re \leq 40$) and the gap ratio between the two cylinders ($2 \leq g \leq 10$) on the local and global flow characteristics such as streamline profiles, center line velocity, surface pressure coefficient and individual and total drag coefficients has been studied in detail. The heat transfer around two spheres in tandem at moderate Reynolds number was investigated numerically by Juncu (2006). The above mentioned papers comprise an excellent review on problems of heat/mass transfer on flow around two tandem circular cylinders.

In case of a cylinder pair in side-by-side arrangements, experimental works

of Bearman (1973), Zdravkovich (1985), and Williamson (1985) concluded that the flow could be summarized into two major regimes and a complex transition region between them. As the two cylinders are in very close proximity, the flow is periodic and wake is a single Karman vortex street as in the flow past a single bluff body. When the two cylinders are in longer distances, coupled and synchronized vortex streets in the wake have been observed.

Research on numerical computations for the flow over multiple cylinders has become active near the last decade of last century. Chang and Song (1990) used a vorticity-stream function method to compute the flow past a pair of cylinders in side-by-side and tandem arrangements at $Re = 100$. Flow visualization and force coefficients were shown to be in good agreement with experiments. Mittal *et al.* (1997) used a finite element method to simulate three configurations, side-by-side, tandem and staggered arrangements of the cylinder pair at $Re = 100$ and 1000. Again, the results compared well with experiments. Recently, Kang (2003) numerically investigated the characteristics of flow over two side-by-side circular cylinders in the range of low Reynolds number defined as $Re = U_\infty D/\nu$ where U_∞ and ν are the free-stream velocity and kinematic viscosity, over the range of $40 \leq Re \leq 160$ and the normalized gap spacing $g^* < 5$; he identified six kinds of wake patterns ($g^* = g/D$, where g and D are the distance between two cylinders surfaces and the cylinder diameter, respectively).

The flow past a rotating cylinder can be considered as the elementary problem related to the topic of present thesis. The rotation of a cylinder has been adopted not only to understand the wake dynamics but also to control the vortical structure in the wake by the numerous researches. As is well known, when a cylinder rotates, the lift force is obtained by the Magnus effect which occurs due to lower pressure on the flow accelerated side than on the flow decelerated

side. Therefore, the flow changes considerably because of the rotation of the cylinder. As a parameter representing this problem, α is the rotational speed at the cylinder surface normalized by the free-stream velocity, accordingly α is defined as $\alpha = \omega D/2U_\infty$, where ω is the angular velocity of the cylinder. The other important parameter is the Reynolds number. Kang *et al.* (1999) researched the flows for $60 \leq Re \leq 160$ in the range of $0 \leq \alpha \leq 2.5$. Their results showed that the vortex shedding completely disappears when $\alpha > \alpha_L$, where α_L is the critical rotational speed which was found to be a logarithmic function of Re . As α increases, the mean lift increases linearly. In contrast, the mean drag decreases with increasing α and has a relatively strong dependence on Re . Stojković *et al.* (2002) calculated the unsteady flow for one characteristic Reynolds number ($Re = 100$) in the typical 2D vortex shedding regime with α varying up to very high rotational speed ($0 \leq \alpha \leq 12$). In the case of low rotational speeds of $0 \leq \alpha \leq 2$, vortex shedding completely is suppressed beyond $\alpha_L = 1.8$ obtained their numerical calculation. In the range of $0 \leq \alpha \leq \alpha_L$ and $Re = 100$ the mean values of drag and lift decreases and increases with increasing α , respectively. Consequently, Stojković *et al.* (2002) fairly confirmed the findings of Kang *et al.* (1999) in the case of unsteady flow at $Re = 100$ for low rotational speeds of $0 \leq \alpha \leq 2$. Mittal and Kumar (2003) numerically investigated the flow past a rotating circular cylinder at $Re = 200$ for various rotational speeds ($0 \leq \alpha \leq 5$). They showed that the vortex shedding ceases beyond $\alpha_L \approx 1.9$.

The problem of flow passing two rotating cylinders in side-by-side arrangement has not been investigated widely. The thesis of Sungnul (2006) is devoted to the study the self-motion of two rotating circular cylinders. Author of this thesis has found only two recent studies of Yoon (2007, 2009) dealing with flow around two rotating circular cylinders in side-by-side arrangement in the range of $|\alpha| \leq 2$

for different gap spacing at $Re = 100$. Only one paper by Joucaviel (2008) has been found, which studies the thermal behavior of an assembly of rotating cylinders aligned in a cross-flow. The objective of Joucaviel (2008) was to maximize the heat transfer rate density of the assembly. A numerical model was used to solve the governing equation. Two configurations were studied: (i) the cylinders rotating in the same direction and (ii) consecutive cylinders rotating in opposite direction. The second configuration proved to be the more efficient.

As reviewed above, the effect of rotation for single cylinder and of gap spacing between two stationary cylinder in side-by-side arrangement on corresponding flow and heat transfer has been studied by numerous researcher. The problem of flow passing two rotating cylinders in a side-by-side arrangement has been studied only by a few researchers. However, the heat transfer and fluid flow past a pair of rotating circular cylinders in side-by-side arrangement has not yet been addressed.

This thesis presents a numerical investigation of the characteristics of the two-dimensional heat transfer and laminar flow around two rotating circular cylinders in side-by-side arrangements. In order to consider the combined effects of the rotation and the spacing between two cylinders on the flow and heat transfer, numerical simulations are performed at a various range of absolute rotational speeds ($|\alpha| \leq 2.5$) for different gap spacing at range of Reynolds number $Re \leq 40$. Quantitative information about the flow and heat transfer variables such as the local and average Nusselt number, pressure and friction coefficients on the cylinder surfaces is highlighted. The pattern of flow and temperature fields are analysed for a wide range of parameters.

The mathematical formulation of the heat/mass transfer problem of flow past two rotating circular cylinders is described in Chapter II. The problem is recast in terms of a cylindrical bipolar coordinate system. Chapter III presents

the details of the numerical algorithm based on the projection method to approximate solution of the momentum equation and the fractional step stabilizing correction method to approximate the solution of the energy equation. In Chapter IV, we represent the validation results of our numerical algorithm by comparison with available numerical and experimental data. The results of various numerical experiments are reported and discussed in Chapter V. Finally some general comments, a summary of the achievements of this work and some ideas on how this research could be continued are provided in Chapter VI.

CHAPTER II

MATHEMATICAL FORMULATION OF PROBLEM

2.1 Physical assumptions

This study assumes the following design considerations:

1. Flow is steady, laminar and two dimensional.

Steady flow shows that there is no variation with time either of the external flow or of flow within the boundary layer. The restriction on the Reynolds number ensures that the flow is laminar.

2. The fluid is considered incompressible with constant properties.

From experiments, it is observed that enormous changes of pressure are required to produce measurable changes in the volumes and densities of liquids (Evans, 1968). Since the flow conditions in this study will not contain such extreme pressure differences, liquids can be regarded as incompressible. In a gaseous medium, experiments have shown that the effects of the compressible nature of the medium begin to appear at high speeds (speed of sound). Since laminar flow is assumed in this study, where the fluid velocity is well below high speeds, the assumption of incompressibility for gases is also retained. The assumption of constant properties also appears to be soundly based because experimental measurements do confirm that for most common gases and liquids, the coefficients of viscosity are changed very small.

3. Body forces are negligible.

The effects of gravitational or buoyancy forces are omitted due to forced convection. Any effects produced by the buoyancy of the fluid due to temperature differences will be assumed to be very small.

4. There are no slip at cylinders surface.

The condition of no slip is confirmed by previous experimental studies and it is acceptable, at least for the fluid flows considered in this study.

5. Viscous dissipation is neglected

The ranges of dimension, velocities and temperatures adopted in this study allow the neglect of viscous dissipation and natural convection effects.

6. Radiation heat transfer is negligible.

7. Temperature differences are small.

A large temperature difference between the fluid and the cylinder surface over which it flows could produce extraneous effects which are avoided in this study.

2.2 Basic equations

Consider the flow of a viscous incompressible fluid with a constant far away streaming velocity (U_∞) and temperature (T_∞), along the y -direction normal to the line between centers of rotating circular cylinders. The cylinders rotate about their axes at angular velocities ω_L and ω_R , assuming that a positive value corresponds to counter-clockwise rotation. The sketch of flow geometry, coordinate system and notations are shown in Figure 2.1. Since the present study is restricted to long cylinders and flow conditions of $Re \leq 40$, the flow across the cylinders is

steady and two-dimensional; i.e., all flow variables are independent of the z - coordinate and are, therefore, functions of the coordinates x and y alone. Furthermore, the thermodynamical properties (density, heat capacity c_p , thermal conductivity k) are assumed to be independent of temperature. Under these conditions, the momentum and energy equations are not coupled.

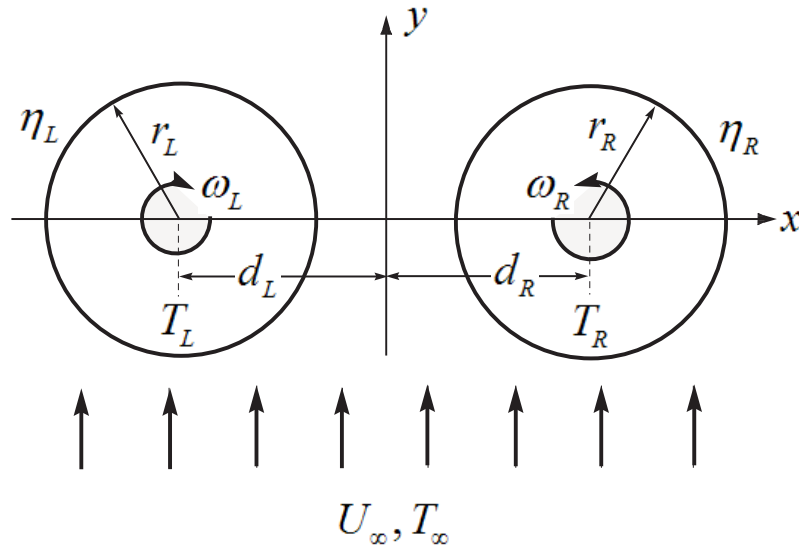


Figure 2.1 Schematics of problem.

From the above circumstances the flow of fluid is governed by the conservation of momentum, mass and energy:

$$\rho \left(\frac{\partial \vec{v}}{\partial t} + (\vec{v} \cdot \nabla) \vec{v} \right) = -\nabla p + \mu \Delta \vec{v}, \quad (2.1)$$

$$\text{div } \vec{v} = 0, \quad (2.2)$$

$$\rho c_p \left(\frac{\partial T}{\partial t} + (\vec{v} \cdot \nabla) T \right) = k \Delta T, \quad (2.3)$$

where \vec{v} denotes the velocity vector, p is the pressure, t is time, T is the fluid temperature, c_p is the heat capacity, μ is the viscosity of the fluid, and k is the thermal conductivity.

When studying fluid flow and heat transfer passing two cylinders, the rea-

sonable coordinate system is the cylindrical bipolar coordinate system. The common definition of cylindrical bipolar coordinates (ξ, η, z) is

$$x = \frac{a \sinh \eta}{\cosh \eta - \cos \xi}, \quad y = \frac{a \sin \xi}{\cosh \eta - \cos \xi}, \quad z = z, \quad (2.4)$$

where $\xi \in [0, 2\pi)$, $\eta \in (-\infty, \infty)$, and $z \in (-\infty, \infty)$, a is a characteristic length in the cylindrical bipolar coordinate system and is positive. The following identities show that curves of constant ξ and η are circles in xy -space

$$\begin{aligned} x^2 + (y - a \cot \xi)^2 &= a^2 \csc^2 \xi, \\ (x - a \coth \eta)^2 + y^2 &= a^2 \operatorname{csch}^2 \eta. \end{aligned} \quad (2.5)$$

The coordinate surfaces $\eta = \text{const}$ and $\xi = \text{const}$ corresponds to a family of cylinders whose centers lie along the x and y axes, respectively. Figure 2.1 shows two cylinders that are chosen to be $\eta = \eta_R$ (with $\eta_R > 0$) and $\eta = \eta_L$ (with $\eta_L < 0$). The cylinders' radii r_L and r_R and the distances of their centers from the origin d_L and d_R are given by

$$r_i = a \operatorname{csch} |\eta_i|, \quad d_i = a \coth |\eta_i|, \quad i = L, R. \quad (2.6)$$

The center to center distance between the cylinders equals $d = d_L + d_R$. If r_L, r_R , and d are given, one can find a , η_L , and η_R from relations (2.4)-(2.6) as follows

$$\begin{aligned} \eta_{R,L} &= \ln \left[\left(\frac{d^2 + r_R^2 - r_L^2}{2dr_R} \right) \pm \sqrt{\left(\frac{d^2 + r_R^2 - r_L^2}{2dr_R} \right)^2 - 1} \right], \\ a &= \sqrt{\frac{d^4 - 2d^2(r_R^2 + r_L^2) + (r_R^2 - r_L^2)^2}{4d^2}}. \end{aligned} \quad (2.7)$$

The two-dimensional governing equations (2.1)-(2.3) describing the flow and heat transfer for viscous incompressible fluid will be studied. For goodest generality, we usually nondimensionalize a given fluid flow and heat transfer problem with the aid of appropriate scales of length, time and other involved properties.

The nondimensional form of the governing equations (2.1)-(2.3) may be expressed in the cylindrical bipolar coordinate system as follows:

$$\begin{aligned} & \frac{\partial v_\xi}{\partial t} + \frac{1}{h} \left(v_\xi \frac{\partial v_\xi}{\partial \xi} + v_\eta \frac{\partial v_\xi}{\partial \eta} \right) - \frac{1}{a} (\sinh \eta (v_\xi v_\eta) - \sin \xi (v_\eta)^2) \\ &= -\frac{1}{h} \frac{\partial p}{\partial \xi} + \frac{1}{h} \frac{2}{Re} \left[\frac{1}{h} \left(\frac{\partial^2 v_\xi}{\partial \xi^2} + \frac{\partial^2 v_\xi}{\partial \eta^2} \right) - \frac{1}{a} \left(\sinh \eta \frac{\partial v_\eta}{\partial \xi} - \sin \xi \frac{\partial v_\eta}{\partial \eta} \right) \right] \\ & - \frac{1}{h} \frac{2}{Re} \left(\frac{\cosh \eta + \cos \xi}{a} \right) v_\xi, \end{aligned} \quad (2.8)$$

$$\begin{aligned} & \frac{\partial v_\eta}{\partial t} + \frac{1}{h} \left(v_\xi \frac{\partial v_\eta}{\partial \xi} + v_\eta \frac{\partial v_\eta}{\partial \eta} \right) + \frac{1}{a} (\sinh \eta (v_\xi)^2 - \sin \xi (v_\xi v_\eta)) \\ &= -\frac{1}{h} \frac{\partial p}{\partial \eta} + \frac{1}{h} \frac{2}{Re} \left[\frac{1}{h} \left(\frac{\partial^2 v_\eta}{\partial \xi^2} + \frac{\partial^2 v_\eta}{\partial \eta^2} \right) + \frac{1}{a} \left(\sinh \eta \frac{\partial v_\xi}{\partial \xi} - \sin \xi \frac{\partial v_\xi}{\partial \eta} \right) \right] \\ & - \frac{1}{h} \frac{2}{Re} \left(\frac{\cosh \eta + \cos \xi}{a} \right) v_\eta, \end{aligned} \quad (2.9)$$

$$\frac{1}{h^2} \left[\frac{\partial (h v_\xi)}{\partial \xi} + \frac{\partial (h v_\eta)}{\partial \eta} \right] = 0, \quad (2.10)$$

$$\frac{\partial T}{\partial t} + \frac{1}{h} \left[v_\xi \frac{\partial T}{\partial \xi} + v_\eta \frac{\partial T}{\partial \eta} \right] = \frac{2}{Re Pr} \frac{1}{h^2} \left[\frac{\partial^2 T}{\partial \xi^2} + \frac{\partial^2 T}{\partial \eta^2} \right], \quad (2.11)$$

where v_ξ and v_η are the velocity components in ξ and η directions, respectively, in the cylindrical bipolar coordinate system, and $h = a/(\cosh \eta - \cos \xi)$. In the above equations, the velocities are nondimensional with free stream velocity U_∞ , all lengths with the radius r_R of right cylinder, time with $(r_R)/(U_\infty)$, pressure by ρU_∞^2 , and temperature by $(T - T_\infty)/(T_R - T_\infty)$. The two nondimensional parameters which appear in the above equations are

- *Reynolds number:*

$$Re = \frac{2U_\infty r_R}{\mu},$$

- *Prandtl number:*

$$Pr = \frac{c_p \mu}{k}.$$

2.3 Boundary condition

The physically realistic boundary conditions for this flow are expressed as follows. On the cylinder surfaces, the usual no-slip condition is applied. The two commonly used thermal boundary conditions at the surfaces of the solid cylinders are the constant temperature condition and the constant heat flux condition. The nondimensional boundary conditions are as follows:

- **On the cylinders surfaces**, the no-slip boundary condition will be used for all solid surfaces of the cylinders ($\eta = \eta_L$ and $\eta = \eta_R$)

$$v_\xi = \alpha_i, \quad v_\eta = 0, \quad \text{at } \eta = \eta_i, \quad \xi \in [0, 2\pi), \quad i = L, R, \quad (2.12)$$

where $\alpha_i = \frac{\omega_i r_i}{U_\infty}$, $i = L, R$ are the nondimensional angular velocities of left and right circular cylinders.

- **At infinity**, the constant streamwise velocity is used,

$$\vec{v} = (v_x, v_y) = (0, 1), \quad \text{as } x^2 + y^2 \rightarrow \infty. \quad (2.13)$$

For the temperature field, we will employ the boundary conditions as follows:

- **On the left and right cylinders surfaces**, constant temperature are

$$T|_{\eta=\eta_L} = \frac{T_L - T_\infty}{T_R - T_\infty}, \quad \text{and} \quad T|_{\eta=\eta_R} = 1. \quad (2.14)$$

- **At infinity**, the uniform temperature will be used,

$$T = 0, \quad \text{as } x^2 + y^2 \rightarrow \infty. \quad (2.15)$$

2.4 Drag and lift coefficients

The two most important characteristic quantities of the flow around a cylinders are the drag and lift coefficients. When a solid body is placed in a fluid flow, the direction of the force on the body does not coincide with the direction of the

(undisturbed) flow. It is convenient to decompose the force into components F_L and F_D perpendicular and parallel to the flow direction. The component F_L is called the lift force. The component F_D is called the drag force (the resistance). The lift F_L and drag F_D forces are usually expressed with the help of nondimensional coefficients in the following form

$$F_L = 0.5C_L\rho AU_\infty^2,$$

$$F_D = 0.5C_D\rho AU_\infty^2,$$

where C_L and C_D are called lift and drag coefficient, ρ is fluid density, A is the reference area (the choice of reference area A affects the value of C_D and C_L). The dependence of drag and lift forces for a single circular cylinder has been well studied in many research articles. In the region of small Reynolds number, the drag coefficient varies strongly with Re . The contribution of the viscous and pressure forces to the drag are very similar in this flow regime. When separation starts at the cylinder and the recirculation region developed behind it at $Re \geq 5$, the contribution of pressure and viscous forces to the drag get out of balance. The accuracy of the computations in this flow regime is commonly verified by a comparison with experimental and numerical data as no analytical results are available.

Let us turn back to the fluid flow past two cylinders. If F_{x_i} and F_{y_i} , $i = L, R$ are the lift and drag on the cylinders, the lift and drag coefficients are defined by

$$C_{L_i} = \frac{F_{x_i}}{2\rho U_\infty r_R}, \quad C_{D_i} = \frac{F_{y_i}}{2\rho U_\infty r_R}, \quad i = L, R, \quad (2.16)$$

and each consists of components due to the friction forces and the pressure. Hence

$$C_L = C_{L_f} + C_{L_p}, \quad C_D = C_{D_f} + C_{D_p}, \quad (2.17)$$

where

$$C_{L_p} = -\frac{1}{\rho U_\infty D} \int_{\Sigma} p \vec{n} \cdot \vec{i}_x dS, \quad (2.18)$$

$$C_{L_f} = -\frac{1}{\rho U_\infty D} \int_{\Sigma} \mu(\vec{n} \times \vec{\omega}) \cdot \vec{i}_x dS, \quad (2.19)$$

$$C_{D_p} = -\frac{1}{\rho U_\infty D} \int_{\Sigma} p \vec{n} \cdot \vec{i}_y dS, \quad (2.20)$$

$$C_{D_f} = -\frac{1}{\rho U_\infty D} \int_{\Sigma} \mu(\vec{n} \times \vec{\omega}) \cdot \vec{i}_y dS, \quad (2.21)$$

Here \vec{i}_x , and \vec{i}_y are unit vectors in x and y axes directions, respectively, and \vec{n} is the outward unit normal to surface vector.

These non-dimensional coefficients C_L and C_D are evaluated by integration around the cylinders walls. The formulas for coefficients in cylindrical bipolar coordinates are the following

$$\begin{aligned} C_{L_p} &= -\int_0^{2\pi} hp \left[\left(-\frac{h}{a} \sinh \eta \sin \xi \right) n_\xi + \left(-\frac{h}{a} (\cosh \eta \cos \xi - 1) \right) n_\eta \right] d\xi, \\ C_{L_f} &= -\int_0^{2\pi} h\mu\omega \left[\left(-\frac{h}{a} \sinh \eta \sin \xi \right) n_\eta + \left(-\frac{h}{a} (\cosh \eta \cos \xi - 1) \right) n_\xi \right] d\xi, \\ C_{D_p} &= -\int_0^{2\pi} hp \left[\left(\frac{h}{a} (\cosh \eta \cos \xi - 1) \right) n_\xi + \left(-\frac{h}{a} \sinh \eta \sin \xi \right) n_\eta \right] d\xi, \\ C_{D_f} &= -\int_0^{2\pi} h\mu\omega \left[\left(\frac{h}{a} (\cosh \eta \cos \xi - 1) \right) n_\eta + \left(-\frac{h}{a} \sinh \eta \sin \xi \right) n_\xi \right] d\xi, \end{aligned} \quad (2.22)$$

where n_ξ and n_η are the components of the outward unit normal vectors in ξ and η direction, respectively, $\vec{n} = (n_\xi, n_\eta)$ and ω is the component of vorticity in z direction,

$$\omega = -\frac{1}{h} \left[\frac{\partial v}{\partial \eta} - \frac{\partial u}{\partial \xi} - \frac{h}{a} (\sinh \eta v - \sin \xi u) \right]. \quad (2.23)$$

2.5 Heat Transfer (Nusselt number)

The important parameter of interest in mass and heat transfer problems is the heat transfer rate per unit area from the cylinder wall to the ambient fluid. At the surface, the relative velocity between the fluid and surface is generally taken as

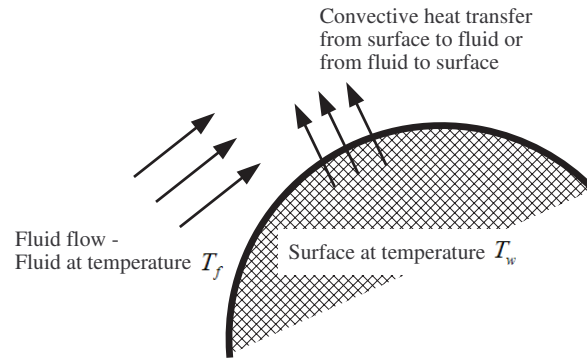


Figure 2.2 Convective heat transfer from a surface.

zero, as a consequence of the no-slip conditions that usually employed. Therefore, the heat transfer at the surface is given by Fourier's Law as:

$$q|_w = -k \left(\frac{\partial T}{\partial n} \right)_w = -k(\nabla T \cdot \vec{n})_w, \quad (2.24)$$

where q is the heat lost by the material at surface, $\left(\frac{\partial T}{\partial n} \right)_w$ is the gradient in the normal to fluid direction evaluated at the surface, and k is the thermal conductivity of the fluid. Instead of equation (2.24), engineers and technicians require an expression based upon measurable quantities. The heat transfer coefficient h may be evaluated from:

$$q|_w = h(T_w - T_f), \quad (2.25)$$

where T_w is the surface temperature and T_f is the fluid temperature. Here, h is a function of the temperature and location on the surface.

The local heat transfer coefficient h is generally presented in terms of the local Nusselt number. In 1915, Nusselt analyzed the heat transfer from cylinders to air in order to find a similarity condition between different flow cases. To establish this similarity he used a normalized form of the specific heat flux called the Nusselt

number

$$Nu = \frac{q_w}{q_{ref}} = \frac{-k_w \left[\frac{\partial(T - T_w)}{\partial r} \right]_w}{\dot{k} \frac{(T_w - T_\infty)}{D}} = \frac{k_w}{\dot{k}} \left[\frac{\partial \left(\frac{T_w - T}{T_w - T_\infty} \right)}{\partial \left(\frac{r}{D} \right)} \right]_w, \quad (2.26)$$

where q_{ref} is a reference heat flux, \dot{k} the thermal conductivity at a reference temperature, k_w is the thermal conductivity of the fluid at cylinder temperature, and the subscript w indicates that quantities are evaluated at the cylinder wall. The Nusselt number is used to obtain the actual heat flux either from equation (2.26) or equation (2.25). Usually just the mean value of the Nusselt number is needed namely when no local effect on the cylinder surface is of particular interest. In this case, the value of Nu is averaged over the whole body surface. The average heat transfer coefficient \bar{h} is obtained by averaging the local heat transfer coefficient over the entire surface. Thus,

$$\bar{h} = \frac{1}{A} \int_A h \, dS, \quad (2.27)$$

where A is the surface area. In our particular case (flow past cylinders) the value of \bar{h} is averaged over the whole cylinder perimeter

$$\bar{h} = \frac{1}{L} \int_0^L h \, d\mathcal{S}, \quad \mathcal{S} \in [0, L], \quad (2.28)$$

where L is the perimeter of cylinder and \mathcal{S} is parametrization of the cylinder surface. An average Nusselt number \overline{Nu} can similarly be defined as

$$\overline{Nu} = \frac{\bar{h}L}{k}. \quad (2.29)$$

The heat transfer rate per unit area measured in the normal direction is

$$-k \left(\frac{\partial T}{\partial n} \right)_w = h(T_w - T_f). \quad (2.30)$$

In the following, the dimensionless variables are denoted by the superscript “*”.

Taking into account that $T^* = \frac{T - T_f}{T_w - T_f}$ and $n^* = \frac{n}{L}$ (L is the characteristic

length), we get

$$\left(\frac{\partial T}{\partial n}\right)_w = \frac{T_w - T_f}{L} \left(\frac{\partial T^*}{\partial n^*}\right)_w. \quad (2.31)$$

Equation (2.30) can be recast as

$$-\frac{k(T_w - T_f)}{L} \left(\frac{\partial T^*}{\partial n^*}\right)_w = h(T_w - T_f). \quad (2.32)$$

Hence, the local Nusselt number can be found as the normal derivative of non-dimensional temperature

$$Nu = - \left(\frac{\partial T^*}{\partial n^*}\right)_w.$$

The average Nusselt number is

$$\overline{Nu} = -\frac{1}{L} \int_0^L \left(\frac{\partial T^*}{\partial n^*}\right)_w dS.$$

In our work, the local Nusselt number in the cylindrical bipolar coordinate system based on the diameter of the cylinder is

$$\begin{aligned} Nu &= - \left(\frac{\partial T}{\partial n}\right) \\ &= -\nabla T \cdot \vec{n} \\ &= -\frac{1}{h} \frac{\partial T}{\partial \eta} \\ &= - \left(\frac{\cosh \eta - \cos \xi}{a}\right) \frac{\partial T}{\partial \eta}. \end{aligned} \quad (2.33)$$

The average Nusselt number can be calculated by the relations:

$$\overline{Nu} = -\frac{1}{2\pi} \int_0^{2\pi} \frac{\partial T}{\partial \eta} d\xi, \quad \xi \in [0, 2\pi]. \quad (2.34)$$

Note that this formula is used for computing the local Nusselt number on the left cylinder and we use the plus sign instead of minus sign for the computation on right cylinder.

CHAPTER III

NUMERICAL METHODS

3.1 Transformation of the governing equations

The first step in computing a numerical solution to the Navier-Stokes equations is the construction of a grid. A well-constructed grid ensures the accuracy and quality of the solution. For the construction of a finite difference scheme the new independent variables are introduced

$$\xi = \chi_1(\hat{\xi}), \quad \eta = \chi_2(\hat{\eta}), \quad (3.1)$$

or by implication

$$\hat{\xi} = \varphi_1(\xi), \quad \hat{\eta} = \varphi_2(\eta), \quad J = \frac{\partial(\xi, \eta)}{\partial(\hat{\xi}, \hat{\eta})} \neq 0. \quad (3.2)$$

This mapping is used to transform the nonuniform mesh in physical space (ξ, η) into a uniform rectangular mesh in computational domain $(\hat{\xi}, \hat{\eta})$. The sketch of the meshes in physical and computational domain can be seen in Figure 3.1.

The functions φ_1 and φ_2 establish a one-to-one correspondence between the nodes of the uniform mesh in the computational domain and the nodes of the nonuniform mesh in the physical domain. The functions φ_1 and φ_2 are constructed by tabularly assigning points in the physical domain to the corresponding points in computational domain. The choice of mapping (3.1) and (3.2) enables us to condense the mesh node near solid boundaries and in the neighborhood of the lines $\eta = 0$ and $\xi = 0$ ($\xi = 2\pi$). In the computational domain $(\hat{\xi}, \hat{\eta})$, the nodes of the mesh are distributed uniformly (see Figure 3.1b).

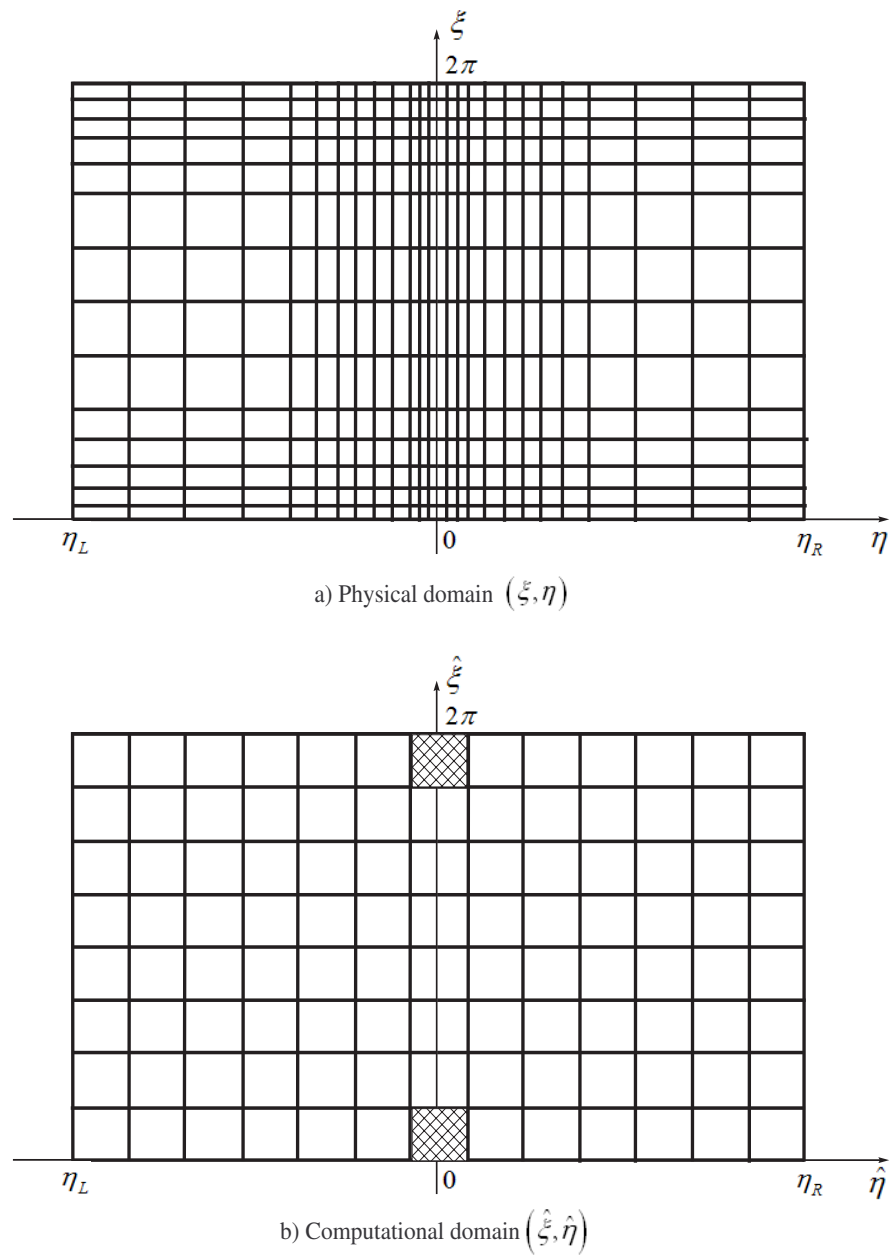


Figure 3.1 Sketch of the meshes in physical and computational domain.

It is not convenient to solve the governing equations over a nonuniform grid. The governing equations (2.8)-(2.11) recast according mesh transformation (3.1) and (3.2) are

$$\begin{aligned} & \frac{\partial v}{\partial t} + \frac{1}{h} \frac{1}{J} \left(v \eta_{\hat{\eta}} \frac{\partial v}{\partial \hat{\xi}} + u \xi_{\hat{\xi}} \frac{\partial v}{\partial \hat{\eta}} \right) - \frac{1}{a} (\sinh(\eta)(vu) - \sin(\xi)(u)^2) \\ &= -\frac{1}{h} \frac{1}{J} \eta_{\hat{\eta}} \frac{\partial p}{\partial \hat{\xi}} + \frac{1}{h^2} \frac{1}{J} \frac{2}{Re} \left[\frac{\partial}{\partial \hat{\xi}} \left(\frac{\eta_{\hat{\eta}}}{\xi_{\hat{\xi}}} \frac{\partial v}{\partial \hat{\xi}} \right) + \frac{\partial}{\partial \hat{\eta}} \left(\frac{\xi_{\hat{\xi}}}{\eta_{\hat{\eta}}} \frac{\partial v}{\partial \hat{\eta}} \right) \right] \\ & - \frac{1}{h} \frac{2}{Re} \left[\frac{1}{J} \frac{1}{2a} \left(\sinh(\eta) \eta_{\hat{\eta}} \frac{\partial u}{\partial \hat{\xi}} - \sin(\xi) \xi_{\hat{\xi}} \frac{\partial u}{\partial \hat{\eta}} \right) + \left(\frac{\cosh(\eta) + \cos(\xi)}{a} \right) v \right], \end{aligned} \quad (3.3)$$

$$\begin{aligned} & \frac{\partial u}{\partial t} + \frac{1}{h} \frac{1}{J} \left(v \eta_{\hat{\eta}} \frac{\partial u}{\partial \hat{\xi}} + u \xi_{\hat{\xi}} \frac{\partial u}{\partial \hat{\eta}} \right) + \frac{1}{a} (\sinh(\eta)(v)^2 - \sin(\xi)(vu)) \\ &= -\frac{1}{h} \frac{1}{J} \xi_{\hat{\xi}} \frac{\partial p}{\partial \eta} + \frac{1}{h^2} \frac{1}{J} \frac{2}{Re} \left[\frac{\partial}{\partial \hat{\xi}} \left(\frac{\eta_{\hat{\eta}}}{\xi_{\hat{\xi}}} \frac{\partial u}{\partial \hat{\xi}} \right) + \frac{\partial}{\partial \hat{\eta}} \left(\frac{\xi_{\hat{\xi}}}{\eta_{\hat{\eta}}} \frac{\partial u}{\partial \hat{\eta}} \right) \right] \\ & + \frac{1}{h} \frac{2}{Re} \left[\frac{1}{J} \frac{1}{2a} \left(\sinh(\eta) \eta_{\hat{\eta}} \frac{\partial v}{\partial \hat{\xi}} - \sin(\xi) \xi_{\hat{\xi}} \frac{\partial v}{\partial \hat{\eta}} \right) - \left(\frac{\cosh(\eta) + \cos(\xi)}{a} \right) u \right], \end{aligned} \quad (3.4)$$

$$\frac{1}{h^2} \frac{1}{J} \left[\eta_{\hat{\eta}} \frac{\partial(hv)}{\partial \hat{\xi}} + \xi_{\hat{\xi}} \frac{\partial(hu)}{\partial \hat{\eta}} \right] = 0, \quad (3.5)$$

$$\frac{\partial T}{\partial t} + \frac{1}{h} \frac{1}{J} \left[v \eta_{\hat{\eta}} \frac{\partial T}{\partial \hat{\xi}} + u \xi_{\hat{\xi}} \frac{\partial T}{\partial \eta} \right] = \frac{2}{RePr} \frac{1}{h^2} \frac{1}{J} \left[\frac{\partial}{\partial \hat{\xi}} \left(\frac{\eta_{\hat{\eta}}}{\xi_{\hat{\xi}}} \frac{\partial T}{\partial \hat{\xi}} \right) + \frac{\partial}{\partial \hat{\eta}} \left(\frac{\xi_{\hat{\xi}}}{\eta_{\hat{\eta}}} \frac{\partial T}{\partial \hat{\eta}} \right) \right], \quad (3.6)$$

where u and v denote velocity components in η and ξ -directions, respectively, J is the Jacobian of the transformation

$$J \stackrel{\text{def}}{=} \begin{vmatrix} \xi_{\hat{\xi}} & \xi_{\hat{\eta}} \\ \eta_{\hat{\xi}} & \eta_{\hat{\eta}} \end{vmatrix} \stackrel{\text{def}}{=} \begin{vmatrix} \xi_{\hat{\xi}} & 0 \\ 0 & \eta_{\hat{\eta}} \end{vmatrix} = \xi_{\hat{\xi}} \eta_{\hat{\eta}}. \quad (3.7)$$

The subscripts indicate the partial derivatives with respect to the subscript variables

$$\xi_{\hat{\xi}} = \frac{\partial \xi}{\partial \hat{\xi}} = \frac{\partial \chi_1(\hat{\xi})}{\partial \hat{\xi}}, \quad \eta_{\hat{\eta}} = \frac{\partial \eta}{\partial \hat{\eta}} = \frac{\partial \chi_2(\hat{\eta})}{\partial \hat{\eta}}. \quad (3.8)$$

3.2 Discretization of the governing equations

3.2.1 Description of grid

The properties of computations are sensitive to the way in which convective and diffusive terms are discretized. In the present work a central difference scheme is used for discretization of both convective and diffusive terms. The grid employed in computations is shown in Figure 3.2. In computational domain, we discretized the flow field into cells of size $\Delta\eta \times \Delta\xi$ with cell centres being identified by integers indexes i and j in the η and ξ directions respectively, $\xi_j = (j - 0.5)\Delta\xi$ and $\eta_i = \eta_L + (i - 0.5)\Delta\eta$ ($\Delta\xi = 2\pi/n$, $\Delta\eta = (\eta_R - \eta_L)/m$). A staggered placement of variables is used with velocity components u located on the vertical sides of each cell and components v on the horizontal sides of each cell. We used the fractional indexes to denote grid values of velocity components $u_{i+1/2,j} = u(\eta_{i+1/2}, \xi_j)$ and $v_{i,j+1/2} = v(\eta_i, \xi_{j+1/2})$ where $\eta_{i+1/2} = \eta_i + 0.5\Delta\eta$, $\xi_{j+1/2} = \xi_j + 0.5\Delta\xi$. The pressure p and temperature T are represented at cell centres (see Figure 3.2), $p_{i,j} = p(\eta_i, \xi_j)$, $T_{i,j} = T(\eta_i, \xi_j)$. The upper index n denotes values of variables at time $t_n = n\tau$, where τ is the small step size in time.

3.2.2 Discretization of Navier-Stokes equations

Description of the projection method

Simulating incompressible flows presents a difficulty of satisfying the property of mass conservation. The velocity field must satisfy the incompressibility constraint, which reflects the inability of pressure to do compression work. For developing numerical approximations to this problem, it is natural to exploit the techniques of the fractional step projection method of Chorin (1968, 1969) and Temam (1969, 1977). The main idea of the fractional step projection method is

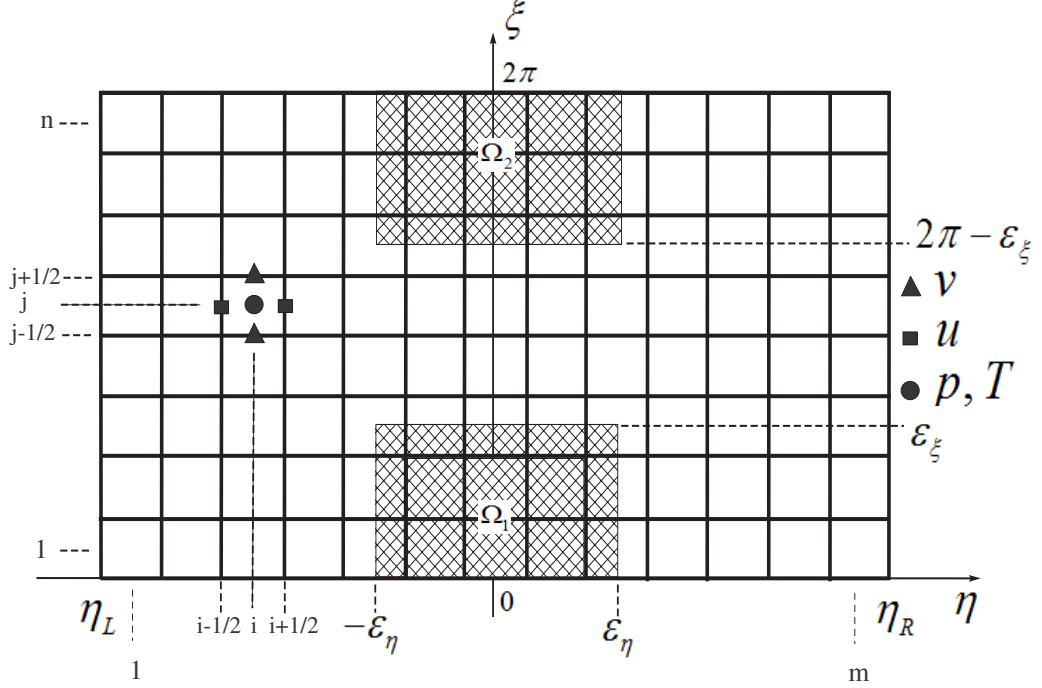


Figure 3.2 Staggered arrangement of v , u , p and T .

the splitting of the viscosity effect from the incompressibility, which are dealt with in two separate subsequent steps. During the first fractional step the problem of viscous (advection-diffusion) step is solved to determine the intermediate velocity \tilde{u}^{n+1} . No pressure is involved in this stage,

$$\frac{\tilde{u}^{n+1} - \bar{u}^n}{\Delta t} = \frac{1}{Re} \Delta \bar{u}^n - (\bar{u}^n \cdot \nabla) \bar{u}^n. \quad (3.9)$$

Finally, having determined the intermediate velocity \tilde{u}^{n+1} , we have to perform the projection step

$$\begin{aligned} \frac{\bar{u}^{n+1} - \tilde{u}^{n+1}}{\Delta t} + \nabla p^{n+1} &= 0, \\ \nabla \cdot \bar{u}^{n+1} &= 0, \end{aligned} \quad (3.10)$$

to determine the end-of-step velocity \bar{u}^{n+1} and the pressure p^{n+1} .

Navier-Stokes equation

The time derivatives are represented by forward differences. In case of a steady solution, time is considered as artificial (iterative time). If the integer n represents the time level, then the intermediate velocity field can be calculated from

$$\tilde{v}_{i,j+\frac{1}{2}} = v_{i,j+\frac{1}{2}}^n - \tau(CONV)_{i,j+\frac{1}{2}}^n + \frac{\tau}{Re}(DIFFV)_{i,j+\frac{1}{2}}^n, \quad (3.11)$$

$$\tilde{u}_{i+\frac{1}{2},j} = u_{i+\frac{1}{2},j}^n - \tau(CONU)_{i+\frac{1}{2},j}^n + \frac{\tau}{Re}(DIFFU)_{i+\frac{1}{2},j}^n. \quad (3.12)$$

Here we used the following notation for convective and diffusive terms

$$\begin{aligned} CONV &= \frac{1}{h} \frac{1}{J} \left(v \eta_{\hat{\eta}} \frac{\partial v}{\partial \hat{\xi}} + u \xi_{\hat{\xi}} \frac{\partial v}{\partial \hat{\eta}} \right) - \frac{1}{a} (\sinh(\eta)(vu) - \sin(\xi)(u)^2), \\ CONU &= \frac{1}{h} \frac{1}{J} \left(v \eta_{\hat{\eta}} \frac{\partial u}{\partial \hat{\xi}} + u \xi_{\hat{\xi}} \frac{\partial u}{\partial \hat{\eta}} \right) + \frac{1}{a} (\sinh(\eta)(v)^2 - \sin(\xi)(vu)), \\ DIFFV &= \frac{1}{h^2} \frac{1}{J} \frac{2}{Re} \left[\frac{\partial}{\partial \hat{\xi}} \left(\frac{\eta_{\hat{\eta}}}{\xi_{\hat{\xi}}} \frac{\partial v}{\partial \hat{\xi}} \right) + \frac{\partial}{\partial \hat{\eta}} \left(\frac{\xi_{\hat{\xi}}}{\eta_{\hat{\eta}}} \frac{\partial v}{\partial \hat{\eta}} \right) \right] \\ &\quad - \frac{1}{h} \frac{2}{Re} \left[\frac{1}{J} \frac{1}{2a} \left(\sinh(\eta) \eta_{\hat{\eta}} \frac{\partial u}{\partial \hat{\xi}} - \sin(\xi) \xi_{\hat{\xi}} \frac{\partial u}{\partial \hat{\eta}} \right) \right] \\ &\quad + \frac{1}{h} \frac{2}{Re} \left[\left(\frac{\cosh(\eta) + \cos(\xi)}{a} \right) v \right], \\ DIFFU &= \frac{1}{h^2} \frac{1}{J} \frac{2}{Re} \left[\frac{\partial}{\partial \hat{\xi}} \left(\frac{\eta_{\hat{\eta}}}{\xi_{\hat{\xi}}} \frac{\partial u}{\partial \hat{\xi}} \right) + \frac{\partial}{\partial \hat{\eta}} \left(\frac{\xi_{\hat{\xi}}}{\eta_{\hat{\eta}}} \frac{\partial u}{\partial \hat{\eta}} \right) \right] \\ &\quad + \frac{1}{h} \frac{2}{Re} \left[\frac{1}{J} \frac{1}{2a} \left(\sinh(\eta) \eta_{\hat{\eta}} \frac{\partial v}{\partial \hat{\xi}} - \sin(\xi) \xi_{\hat{\xi}} \frac{\partial v}{\partial \hat{\eta}} \right) \right] \\ &\quad - \frac{1}{h} \frac{2}{Re} \left[\left(\frac{\cosh(\eta) + \cos(\xi)}{a} \right) u \right]. \end{aligned}$$

The velocity components, $\tilde{v}_{i,j+\frac{1}{2}}$ and $\tilde{u}_{i+\frac{1}{2},j}$ are computed for all faces of the cell except one, where the velocity components are given by the boundary condition. Figure 3.3 shows the location of grid points where velocity components are known from the no-slip boundary condition or the boundary condition at infinity. The boundary condition at infinity is shifted on the boundary of finite domain. The convection and diffusion terms in (3.11)-(3.12) are given by the following equations

$$\begin{aligned}
(CONV)_{i,j+\frac{1}{2}}^n &= \frac{1}{h_{i,j+1/2}} \frac{1}{J_{i,j+1/2}} \left(v_{i,j+1/2}^n \left(\frac{\partial v}{\partial \xi} \right)_{i,j+1/2}^n + u_{i,j+1/2}^n \left(\frac{\partial v}{\partial \eta} \right)_{i,j+1/2}^n \right) \\
&\quad - \frac{1}{a} \left(\sinh(\eta_i) (v_{i,j+1/2}^n u_{i,j+1/2}^n) - \sin(\xi_{j+1/2}) (u_{i,j+1/2}^n)^2 \right),
\end{aligned}$$

$$\begin{aligned}
(CONU)_{i+\frac{1}{2},j}^n &= \frac{1}{h_{i+1/2,j}} \frac{1}{J_{i+1/2,j}} \left(v_{i+1/2,j}^n \left(\frac{\partial u}{\partial \xi} \right)_{i+1/2,j}^n + u_{i+1/2,j}^n \left(\frac{\partial u}{\partial \eta} \right)_{i+1/2,j}^n \right) \\
&\quad + \frac{1}{a} \left(\sinh(\eta_{i+1/2}) (v_{i+1/2,j}^n)^2 - \sin(\xi_j) (v_{i+1/2,j}^n u_{i+1/2,j}^n) \right),
\end{aligned}$$

$$\begin{aligned}
(DIFFV)_{i,j+\frac{1}{2}}^n &= \frac{2}{Re} \frac{1}{h_{i,j+1/2}^2} \frac{1}{J_{i,j+1/2}} \left[\left(\frac{\partial^2 v}{\partial \xi^2} \right)_{i,j+1/2}^n + \left(\frac{\partial^2 v}{\partial \eta^2} \right)_{i,j+1/2}^n \right] \\
&\quad - \frac{1}{Re} \frac{1}{h_{i,j+1/2}} \frac{1}{J_{i,j+1/2}} \frac{1}{a} \sinh(\eta_i) \left(\frac{\partial u}{\partial \xi} \right)_{i,j+1/2}^n \\
&\quad + \frac{1}{Re} \frac{1}{h_{i,j+1/2}} \frac{1}{J_{i,j+1/2}} \sin(\xi_{j+1/2}) \left(\frac{\partial u}{\partial \eta} \right)_{i,j+1/2}^n \\
&\quad - \frac{2}{Re} \frac{1}{h_{i,j+1/2}} \left[\left(\frac{\cosh \eta + \cos \xi}{a} \right)_{i,j+1/2} v_{i,j+1/2}^n \right],
\end{aligned}$$

$$\begin{aligned}
(DIFFU)_{i+\frac{1}{2},j}^n &= \frac{2}{Re} \frac{1}{h_{i+1/2,j}^2} \frac{1}{J_{i+1/2,j}} \left[\left(\frac{\partial^2 u}{\partial \xi^2} \right)_{i+1/2,j}^n + \left(\frac{\partial^2 u}{\partial \eta^2} \right)_{i+1/2,j}^n \right] \\
&\quad + \frac{1}{Re} \frac{1}{h_{i+1/2,j}} \frac{1}{J_{i+1/2,j}} \frac{1}{a} \sinh(\eta_{i+1/2}) \left(\frac{\partial v}{\partial \xi} \right)_{i+1/2,j}^n \\
&\quad - \frac{1}{Re} \frac{1}{h_{i+1/2,j}} \frac{1}{J_{i+1/2,j}} \frac{1}{a} \sin(\xi_j) \left(\frac{\partial v}{\partial \eta} \right)_{i+1/2,j}^n \\
&\quad + \frac{2}{Re} \frac{1}{h_{i+1/2,j}} \left[\left(\frac{\cosh \eta + \cos \xi}{a} \right)_{i+1/2,j} u_{i+1/2,j}^n \right],
\end{aligned}$$

for the sake of simplicity we have introduced the following notations

$$u_{i,j+1/2} = \frac{1}{4}(u_{i+\frac{1}{2},j} + u_{i+\frac{1}{2},j-1} + u_{i-\frac{1}{2},j} + u_{i-\frac{1}{2},j-1}),$$

$$\left(\frac{\partial v}{\partial \xi}\right)_{i,j+1/2} = \frac{1}{J_{i,j+1/2}} \left(\frac{\eta_{i+1/2} - \eta_{i-1/2}}{\Delta \eta}\right) \left(\frac{v_{i,j+3/2} - v_{i,j-1/2}}{2\Delta \eta}\right),$$

$$\left(\frac{\partial v}{\partial \eta}\right)_{i,j+1/2} = \frac{1}{J_{i,j+1/2}} \left(\frac{\xi_{j+1} - \xi_j}{\Delta \xi}\right) \left(\frac{v_{i+1,j+1/2} - v_{i-1,j+1/2}}{2\Delta \eta}\right),$$

$$\begin{aligned} \left(\frac{\partial^2 v}{\partial \xi^2}\right)_{i,j+1/2} &= \frac{1}{J_{i,j+1/2}} \frac{1}{\Delta \xi^2} \left[\left(\frac{\eta_{i+1/2} - \eta_{i-1/2}}{\Delta \eta} \frac{\Delta \xi}{\xi_{j+3/2} - \xi_{j+1/2}}\right) (v_{i,j+3/2} - v_{i,j+1/2}) \right. \\ &\quad \left. - \left(\frac{\eta_{i+1/2} - \eta_{i-1/2}}{\Delta \eta} \frac{\Delta \xi}{\xi_{j+1/2} - \xi_{j-1/2}}\right) (v_{i,j+1/2} - v_{i,j-1/2}) \right], \end{aligned}$$

$$\begin{aligned} \left(\frac{\partial^2 v}{\partial \eta^2}\right)_{i,j+1/2} &= \frac{1}{J_{i,j+1/2}} \frac{1}{\Delta \eta^2} \left[\left(\frac{\xi_{j+1} - \xi_j}{\Delta \xi} \frac{\Delta \eta}{\eta_{i+1} - \eta_i}\right) (v_{i+1,j+1/2} - v_{i,j+1/2}) \right. \\ &\quad \left. - \left(\frac{\xi_{j+1} - \xi_j}{\Delta \xi} \frac{\Delta \eta}{\eta_i - \eta_{i-1}}\right) (v_{i,j+1/2} - v_{i-1,j+1/2}) \right], \end{aligned}$$

$$\begin{aligned} \left(\frac{\partial u}{\partial \xi}\right)_{i,j+1/2} &= \frac{1}{J_{i,j+1/2}} \left(\frac{\eta_{i+1/2} - \eta_{i-1/2}}{\Delta \eta}\right) [(u_{i+1/2,j+1} - u_{i-1/2,j+1}) \\ &\quad - (u_{i+1/2,j} - u_{i-1/2,j})]/2\Delta \xi, \end{aligned}$$

$$\begin{aligned} \left(\frac{\partial u}{\partial \eta}\right)_{i,j+1/2} &= \frac{1}{J_{i,j+1/2}} \left(\frac{\xi_{j+1} - \xi_j}{\Delta \xi}\right) [(u_{i+1/2,j+1} - u_{i+1/2,j}) \\ &\quad - (u_{i-1/2,j+1} - u_{i-1/2,j})]/2\Delta \eta, \end{aligned}$$

$$J_{i,j+1/2} = \left(\frac{\xi_{j+3/2} - \xi_{j-1/2}}{2\Delta \xi}\right) \left(\frac{\eta_{i+1} - \eta_{i-1}}{2\Delta \eta}\right),$$

$$h_{i,j+1/2} = \frac{a}{\cosh(\eta_i) - \cos(\xi_{j+1/2})},$$

$$v_{i+1/2,j} = \frac{1}{4}(v_{i+1,j+\frac{1}{2}} + v_{i,j+\frac{1}{2}} + v_{i+1,j-\frac{1}{2}} + v_{i,j-\frac{1}{2}}),$$

$$\left(\frac{\partial u}{\partial \xi}\right)_{i+1/2,j} = \frac{1}{J_{i+1/2,j}} \left(\frac{\eta_{i+1} - \eta_i}{\Delta \eta}\right) \left(\frac{u_{i+1/2,j+1} - u_{i+1/2,j-1}}{2\Delta \xi}\right),$$

$$\left(\frac{\partial u}{\partial \eta}\right)_{i+1/2,j} = \frac{1}{J_{i+1/2,j}} \left(\frac{\xi_{j+1/2} - \xi_{j-1/2}}{\Delta \xi}\right) \left(\frac{u_{i+3/2,j} - u_{i-1/2,j}}{2\Delta \eta}\right),$$

$$\begin{aligned} \left(\frac{\partial^2 u}{\partial \xi^2}\right)_{i+1/2,j} &= \frac{1}{J_{i+1/2,j}} \frac{1}{\Delta \xi^2} \left[\left(\frac{\eta_{i+1} - \eta_i}{\Delta \eta} \frac{\Delta \xi}{\xi_{j+1} - \xi_j}\right) (u_{i+1/2,j+1} - u_{i+1/2,j}) \right. \\ &\quad \left. - \left(\frac{\eta_{i+1} - \eta_i}{\Delta \eta} \frac{\Delta \xi}{\xi_j - \xi_{j-1}}\right) (u_{i+1/2,j} - u_{i+1/2,j-1}) \right], \end{aligned}$$

$$\begin{aligned} \left(\frac{\partial^2 u}{\partial \eta^2}\right)_{i+1/2,j} &= \frac{1}{J_{i+1/2,j}} \frac{1}{\Delta \eta^2} \left[\left(\frac{\xi_{j+1/2} - \xi_{j-1/2}}{\Delta \xi} \frac{\Delta \eta}{\eta_{i+3/2} - \eta_{i+1/2}}\right) (u_{i+3/2,j} - u_{i+1/2,j}) \right. \\ &\quad \left. - \left(\frac{\xi_{j+1/2} - \xi_{j-1/2}}{\Delta \xi} \frac{\Delta \eta}{\eta_{i+1/2} - \eta_{i-1/2}}\right) (u_{i+1/2,j} - u_{i-1/2,j}) \right], \end{aligned}$$

$$\begin{aligned} \left(\frac{\partial v}{\partial \xi}\right)_{i+1/2,j} &= \frac{1}{J_{i+1/2,j}} \left(\frac{\eta_{i+1} - \eta_i}{\Delta \eta}\right) [(v_{i+1,j+1/2} + v_{i,j+1/2}) \\ &\quad - (v_{i+1,j-1/2} + v_{i,j-1/2})]/2\Delta \xi, \end{aligned}$$

$$\begin{aligned} \left(\frac{\partial v}{\partial \eta}\right)_{i+1/2,j} &= \frac{1}{J_{i+1/2,j}} \left(\frac{\xi_{j+1/2} - \xi_{j-1/2}}{\Delta \xi}\right) [(v_{i+1,j+1/2} + v_{i+1,j-1/2}) \\ &\quad - (v_{i,j+1/2} + v_{i,j-1/2})]/2\Delta \eta, \end{aligned}$$

$$J_{i+1/2,j} = \left(\frac{\xi_{j+1} - \xi_{j-1}}{2\Delta \xi}\right) \left(\frac{\eta_{i+3/2} - \eta_{i-1/2}}{2\Delta \eta}\right),$$

$$h_{i+1/2,j} = \frac{a}{\cosh(\eta_{i+1/2}) - \cos(\xi_j)}.$$

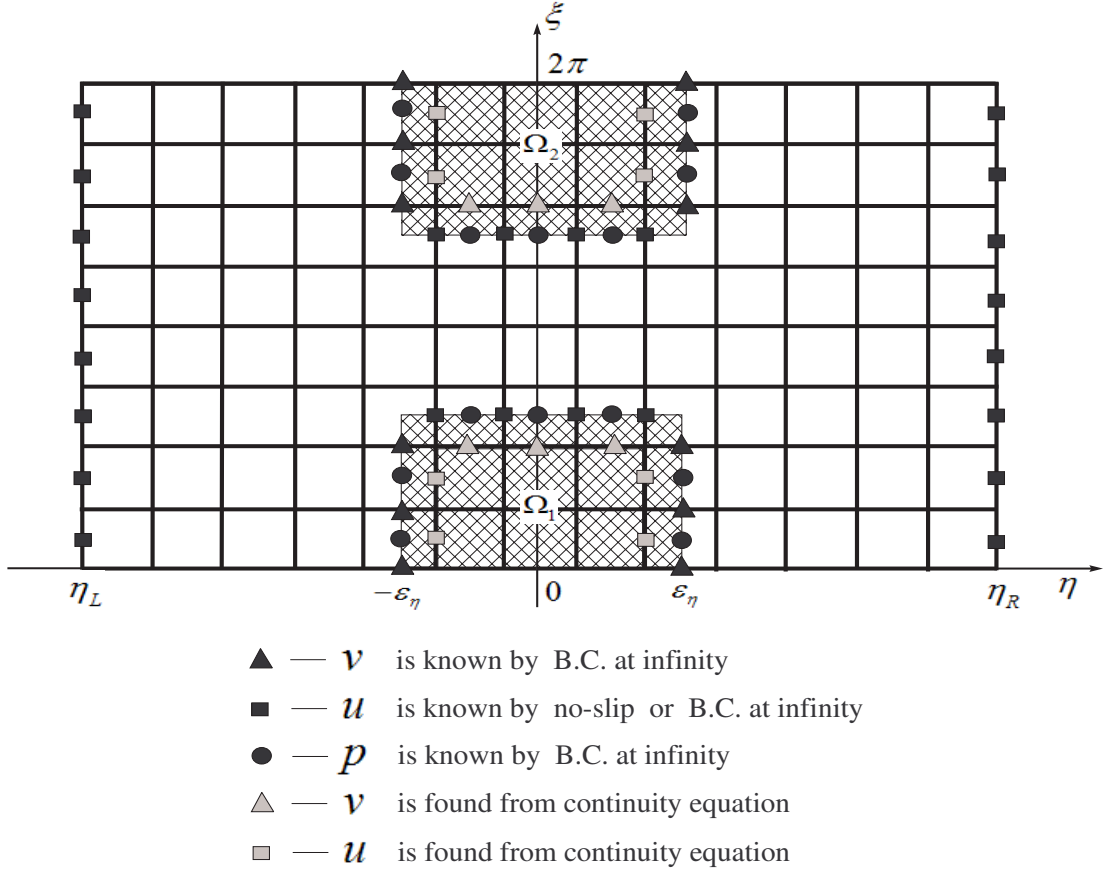


Figure 3.3 The location of known velocity field at the infinity boundary.

The artificial velocity components $\tilde{v}_{i,j+\frac{1}{2}}$ and $\tilde{u}_{i+\frac{1}{2},j}$ are obtained through solution of momentum equations (3.11)-(3.12). The explicit advanced tilde velocity may not necessarily lead to a flow field with zero mass divergence in each cell. This is because at this stage the pressure field not used. Terms with no superscript are taken at the n^{th} time level. Pressure p^{n+1} and velocity components u^{n+1} and v^{n+1} have to be computed simultaneously from the discrete analog of equation (3.10), in such a way that no net mass flow takes place in or out of a cell. In a such case, we make use of an iterative correction procedure in order to obtain a divergence

free velocity field. First, equation (3.10) can be recast in the following form

$$v_{i,j+1/2}^{n+1,s} = \tilde{v}_{i,j+1/2} - \frac{\tau}{h_{i,j+1/2}} \left(\frac{\partial p}{\partial \xi} \right)_{i,j+1/2}^{n+1,s-1}, \quad (3.13)$$

$$u_{i+1/2,j}^{n+1,s} = \tilde{u}_{i+1/2,j} - \frac{\tau}{h_{i+1/2,j}} \left(\frac{\partial p}{\partial \eta} \right)_{i+1/2,j}^{n+1,s-1}, \quad (3.14)$$

where

$$\begin{aligned} \left(\frac{\partial p}{\partial \xi} \right)_{i,j+1/2} &= \frac{1}{J_{i,j+1/2}} \left(\frac{\eta_{i+1/2} - \eta_{i-1/2}}{\Delta \eta} \right) \left(\frac{p_{i,j+1} - p_{i,j}}{\Delta \xi} \right), \\ \left(\frac{\partial p}{\partial \eta} \right)_{i+1/2,j} &= \frac{1}{J_{i+1/2,j}} \left(\frac{\xi_{j+1/2} - \xi_{j-1/2}}{\Delta \xi} \right) \left(\frac{p_{i+1,j} - p_{i,j}}{\Delta \eta} \right). \end{aligned}$$

The discretized form of continuity equation in (3.10) is

$$\begin{aligned} \operatorname{div}(u, v)_{i,j}^{n+1,s} &= \frac{1}{J_{i,j}} \frac{1}{h_{i,j}^2} \left[\left(\frac{\eta_{i+1} - \eta_{i-1}}{2\Delta \eta} \right) \left(\frac{(hv^{n+1,s})_{i,j+1/2} - (hv^{n+1,s})_{i,j-1/2}}{\Delta \xi} \right) \right. \\ &\quad \left. + \left(\frac{\xi_{j+1} - \xi_{j-1}}{2\Delta \xi} \right) \left(\frac{(hu^{n+1,s})_{i+1/2,j} - (hu^{n+1,s})_{i-1/2,j}}{\Delta \eta} \right) \right], \end{aligned} \quad (3.15)$$

where the index s is used to denote iteration number, $s = 1, 2, 3, \dots$. In the case $s = 1$, $p^{n+1,0} = p^n$. Substitution of (3.13) and (3.14) into equation (3.15) results into a system of linear equations for unknown pressure at all grid points. If some side of cell (i, j) coincides with a boundary where velocity components are known, we do not perform the substitution and use the velocity given by the boundary conditions. The point iterative pressure equation becomes

$$p_{i,j}^{n+1,s} = p_{i,j}^{n+1,s-1} - \frac{\beta}{\tau} (\operatorname{div}(u, v)_{i,j}^{n+1,s}), \quad (3.16)$$

where $\operatorname{div}(u, v)_{i,j}^{n+1,s}$ is the unsatisfied divergency at the $(i, j)^{th}$ cell due to incorrect velocities $\tilde{u}_{i+1/2,j}^{n+1}$ and $\tilde{v}_{i,j+1/2}^{n+1}$.

The pressure advanced equation (3.16) can be interpreted as Jacobi iterative method to solve the Poisson equation for pressure. In fact, taking the divergence operation on both sides of the first equation (3.10) and requiring that

$\nabla \cdot \bar{u}^{n+1} \equiv 0$, we get the following Poisson equation for pressure,

$$\operatorname{div}(\nabla p^{n+1}) = \frac{1}{\tau} \operatorname{div}(\tilde{u}, \tilde{v}). \quad (3.17)$$

Finite difference approximation of (3.17) results in an algebraic system with respect to the unknown vector $[\dots, p_{i-1,j}, p_{i,j}, p_{i+1,j}, p_{i,j-1}, p_{i,j+1}, \dots]$ which can be solved by the method of false transient

$$B \left(\frac{\partial p}{\partial \beta} \right)^{n+1} = \operatorname{div}(\nabla p^{n+1}) - \frac{1}{\tau} \operatorname{div}(\tilde{u}, \tilde{v}), \quad (3.18)$$

where β is an iterative parameter and B is any nonsingular operator (for example, $B = E - \text{identity operator}$). Equation (3.16) is a particular case of (3.18) where the forward finite difference is used to approximate the left-hand-side in (3.16),

$$\left(\frac{\partial p}{\partial \beta} \right)^{n+1,s+1} \approx \frac{p_{i,j}^{n+1,s+1} - p_{i,j}^{n+1,s}}{\beta}. \quad (3.19)$$

In our computation, instead (3.19) we also used the following approximation,

$$\left(\frac{\partial p}{\partial \beta} \right)^{n+1,s+1} \approx \frac{3 p_{i,j}^{n+1,s+1} - 4 p_{i,j}^{n+1,s} + p_{i,j}^{n+1,s-1}}{2 \beta}. \quad (3.20)$$

In some cases (3.20) results in faster convergence of the method of false transients. The pressure (velocity) equations explained above are to be iterated until the continuity equation is satisfied to the prescribed accuracy and then the computation proceeds to next time step (artificial time)

$$\operatorname{div}(u_{i,j}^{n+1,s}, v_{i,j}^{n+1,s}) \leq 10^{-6}. \quad (3.21)$$

The optimal value of the relaxation parameter β was found by trial and error.

The Figure 3.4 shows the flow chart of the numerical algorithm used.

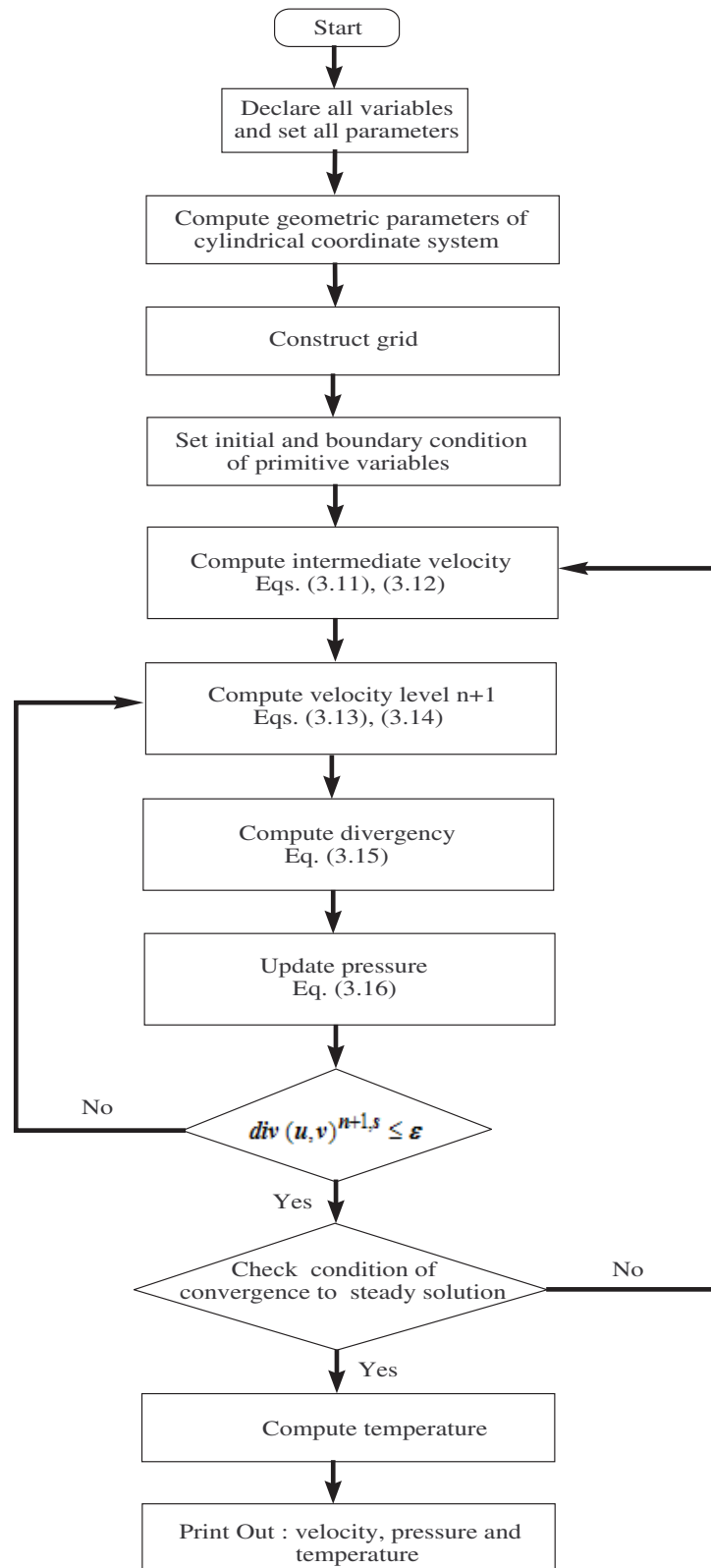


Figure 3.4 The flow chart of the numerical algorithm.

Boundary conditions

On the surface of the cylinders, the no-slip condition is applied, which is equivalent to setting the tangential velocity at the boundary to α_i ($i = L, R$) and the normal velocity to zero. In the present study, the left and right cylinders rotate in clockwise ($\alpha < 0$) and counterclockwise ($\alpha > 0$) directions, respectively. Implementation of no-slip and no penetration boundary conditions is straightforward. In all computations we assume that the boundary grid points are exactly located on solid boundary. Because of the staggered arrangement of the variables, we used second order one-side finite difference to approximate the derivatives $\frac{\partial v}{\partial \hat{\eta}}$ and $\frac{\partial}{\partial \hat{\eta}} \left(\frac{\xi_{\hat{\xi}}}{\eta_{\hat{\eta}}} \frac{\partial v}{\partial \hat{\eta}} \right)$ in equation (3.3) near the cylinder surfaces

$$\begin{aligned} \left(\frac{\partial v}{\partial \hat{\eta}} \right)_{1,j+1/2} &= \frac{\frac{1}{2}(v_{1,j+1/2} + v_{2,j+1/2}) - v_{\eta_L}}{\Delta \hat{\eta}}, \\ \left(\frac{\partial v}{\partial \hat{\eta}} \right)_{m,j+1/2} &= \frac{v_{\eta_R} - \frac{1}{2}(v_{m,j+1/2} + v_{m-1,j+1/2})}{\Delta \hat{\eta}}, \\ \left[\frac{\partial}{\partial \hat{\eta}} \left(\frac{\xi_{\hat{\xi}}}{\eta_{\hat{\eta}}} \frac{\partial v}{\partial \hat{\eta}} \right) \right]_{1,j+1/2} &= \frac{1}{\Delta \eta} \left[\left(\frac{\xi_{\hat{\xi}}}{\eta_{\hat{\eta}}} \frac{\partial v}{\partial \hat{\eta}} \right)_{\frac{3}{2},j+\frac{1}{2}} - \left(\frac{\xi_{\hat{\xi}}}{\eta_{\hat{\eta}}} \frac{\partial v}{\partial \hat{\eta}} \right)_{\eta_L,j+\frac{1}{2}} \right], \\ \left[\frac{\partial}{\partial \hat{\eta}} \left(\frac{\xi_{\hat{\xi}}}{\eta_{\hat{\eta}}} \frac{\partial v}{\partial \hat{\eta}} \right) \right]_{m,j+1/2} &= \frac{1}{\Delta \eta} \left[\left(\frac{\xi_{\hat{\xi}}}{\eta_{\hat{\eta}}} \frac{\partial v}{\partial \hat{\eta}} \right)_{\eta_R,j+\frac{1}{2}} - \left(\frac{\xi_{\hat{\xi}}}{\eta_{\hat{\eta}}} \frac{\partial v}{\partial \hat{\eta}} \right)_{m-\frac{1}{2},j+\frac{1}{2}} \right]. \end{aligned}$$

Here, we are approximated the derivative of velocity on the left and right boundaries by

$$\begin{aligned} \left(\frac{\partial v}{\partial \hat{\eta}} \right)_{\eta_L,j+\frac{1}{2}} &= \frac{1}{\Delta \eta} \left(-\frac{8}{3}v_{\eta_L} + 3v_{1,j+1/2} - \frac{1}{3}v_{2,j+1/2} \right), \\ \left(\frac{\partial v}{\partial \hat{\eta}} \right)_{\eta_R,j+\frac{1}{2}} &= \frac{1}{\Delta \eta} \left(\frac{8}{3}v_{\eta_R} - 3v_{m,j+1/2} + \frac{1}{3}v_{m-1,j+1/2} \right). \end{aligned}$$

The sketch of grid and location of velocity component in ξ -direction is represent in Figure 3.5.

Boundary condition at infinity

In a numerical simulation it is impossible to satisfy constant streamwise velocity as $x^2 + y^2 \rightarrow \infty$. Usual practice involves the placement of the conditions

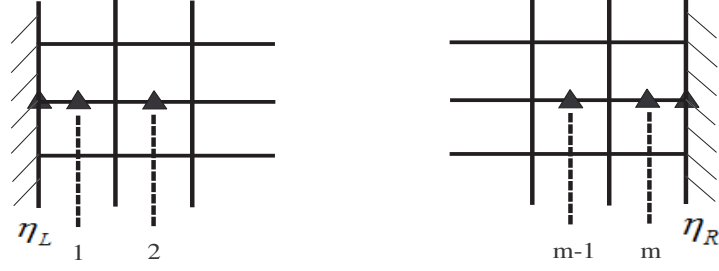


Figure 3.5 The structure of velocity in ξ -direction that used for compute $\frac{\partial v}{\partial \eta}$ on the left and right boundary.

at a far (“artificial”) boundary which is located at large distance from the body. The integral parameters, such as C_D , C_{D_p} , and C_{D_f} demonstrate an essential dependence on the relative size of the computational domain. In 1998, Lange pointed out that the Reynolds number may be seen as a ratio of two characteristic lengths: the cylinder diameter D and a viscous length scale represented by ν/U_∞ . This viscous length scale indicates the magnitude of the region influenced by diffusion of the cylinder momentum and it varies with Re^{-1} . If the boundary of the computational domain does not approximately accompany the expansion of the influence region at small Re , the error caused by the artificial boundary condition disturbs the solution, affecting even the vicinity of the cylinders. In our study we did not touch this range of small Re .

In our computation the far-field boundary coincides with lines $\xi = constant$ and $\eta = constant$ (recall that images of ∞ in computational domain are two points $(\xi = 0, \eta = 0)$ and $(\xi = 2\pi, \eta = 0)$). To be more exact, we choose far boundary

as the boundary of the following domain

$$\begin{aligned}\Omega_1 &= \{(\xi, \eta) | (\eta = \pm(k_w + 0.5)\Delta\eta \text{ and } 0 \leq \xi \leq (k_d + 0.5)\Delta\xi) \cup \\ &\quad (\xi = (k_d + 0.5)\Delta\xi \text{ and } -(k_w + 0.5)\Delta\eta \leq \eta \leq (k_w + 0.5)\Delta\eta)\}, \\ \Omega_2 &= \{(\xi, \eta) | (\eta = \pm(k_w + 0.5)\Delta\eta \text{ and } 2\pi - (k_d + 0.5)\Delta\xi \leq \xi \leq 2\pi) \cup \\ &\quad (\xi = 2\pi - (k_d + 0.5)\Delta\xi \text{ and } -(k_w + 0.5)\Delta\eta \leq \eta \leq (k_w + 0.5)\Delta\eta)\}\end{aligned}$$

where k_w, k_d are integer numbers. In Figure 3.3, a sketch of these domain Ω_1 and Ω_2 is shown by shadow regions.

At the nodes of the mesh which is located on the boundary of the regions Ω_1 and Ω_2 we assumed that

$$\begin{aligned}v &= \left(-\frac{h}{a} \sinh \eta \sin \xi\right)(v_x)_\infty + \left(\frac{h}{a} (\cosh \eta \cos \xi - 1)\right)(v_y)_\infty, \\ u &= \left(-\frac{h}{a} (\cosh \eta \cos \xi - 1)\right)(v_x)_\infty + \left(-\frac{h}{a} \sinh \eta \sin \xi\right)(v_y)_\infty, \\ p &= p_\infty.\end{aligned}\tag{3.22}$$

Here we have utilized the idea that prescribing tangent component of velocity and pressure gives a well-posed problem for the Navier-Stokes equations (Antontsev *et al.* (1990), Moshkin and Damrongsak (2009)). The normal to the boundary component of the velocity vector is computed from the requirement of continuity equation for the cells contained in this boundary. For example for the case shown in Figure 3.6.

$$\begin{aligned}div(u, v)^{n+1} &= 0, \\ \frac{u_E^{n+1} - u_W^{n+1}}{\Delta\eta} + \frac{v_N^{n+1} - v_S^{n+1}}{\Delta\xi} &= 0, \\ u_E^{n+1} &= u_W^{n+1} - \frac{\Delta\eta}{\Delta\xi}(v_N^{n+1} - v_S^{n+1}).\end{aligned}$$

3.3 Discretization of the energy equation

The momentum and energy equations are not coupled. The energy equation is solved separately from the Navier-Stokes equations. When the steady solution

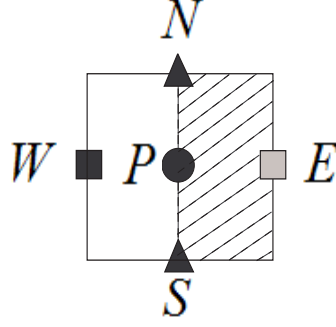


Figure 3.6 The cell at far boundary.

of Navier-Stokes equations are computed, the iterative method of stabilizing correction is used (see Yanenko (1971)) to find the steady distribution of temperature. The structure of the scheme of stabilizing correction is the following:

- the first fractional step produces absolute consistency with the energy equation,
- all succeeding fractional steps are corrections and serve to improve the stability.

For the 2D case, the scheme possesses strong stability and satisfies the property of complete consistency. The requirement of complete consistency guarantees convergence of the nonsteady solution to the steady solution for arbitrary time and space step size (Yanenko (1971)).

To describe the scheme of stabilizing correction, consider a two dimensional convection-diffusion equation in the form

$$(\vec{v} \cdot \nabla)T = \frac{2}{RePr} \Delta T, \quad (3.23)$$

where $T = T(\xi, \eta)$, $\vec{v} = (v_\xi, v_\eta)$, ∇ is the gradient operator, and Δ is the Laplace operator. To find the steady solution of (3.23) we use the method of false transient and consider the related nonsteady problem with “fiction” time

$$\frac{\partial T}{\partial t} = \Lambda_1 T + \Lambda_2 T, \quad (3.24)$$

where Λ_1, Λ_2 represent the derivatives in only one space direction (for example: $\Lambda_1 = -v \frac{\partial}{\partial \xi} + \frac{2}{RePr} \frac{\partial^2}{\partial \xi^2}$, $\Lambda_2 = -u \frac{\partial}{\partial \eta} + \frac{2}{RePr} \frac{\partial^2}{\partial \eta^2}$). For the solution of (3.24)

Douglas and Rachford (1956) proposed the following scheme

$$\frac{T^{k+1/2} - T^k}{\tau} = \Lambda_1 T^{k+1/2} + \Lambda_2 T^k, \quad (3.25)$$

$$\frac{T^{k+1} - T^{k+1/2}}{\tau} = \Lambda_2 (T^{k+1} - T^k). \quad (3.26)$$

Eliminating $T^{k+1/2}$ we can rewrite system (3.25) and (3.26) in the uniform form

$$\frac{T^{k+1} - T^k}{\tau} = \Lambda_1 T^{k+1} + \Lambda_2 T^{k+1} - \tau \Lambda_1 \Lambda_2 (T^{k+1} - T^k). \quad (3.27)$$

It follows that schemes (3.25) and (3.26), and the equivalent scheme (3.27) approximate equation (3.23) with the same accuracy as the scheme

$$\frac{T^{k+1} - T^k}{\tau} = \Lambda_1 T^{k+1} + \Lambda_2 T^{k+1}. \quad (3.28)$$

Details of discretization

Temperature references to nodes of main computational grid related with center of cells of discrete domain $\Omega_h = \{(\xi_j, \eta_i) | \xi_j = (j - 0.5)\Delta\xi, \eta_i = \eta_L + (i - 0.5)\Delta\eta, j = 0, 1, \dots, n+1, i = 0, 1, \dots, m+1\}$. A sketch of the grid for temperature in the computational domain is shown in Figure 3.7. It needs to be noted that on the boundary of the shadowed domains Ω_1 and Ω_2 the constant temperature of uniform stream $T = T_\infty$ is prescribed. The constant temperature of cylinder surfaces is approximated by the following

$$\begin{aligned} \frac{T_{0,j} + T_{1,j}}{2} &= T_L, \\ \frac{T_{m+1,j} + T_{m,j}}{2} &= T_R, \end{aligned}$$

where $T_{0,j}$ and $T_{m+1,j}$ are “ghost” points introduced for convenience in writing the computational code. The finite difference approximation of the first fractional

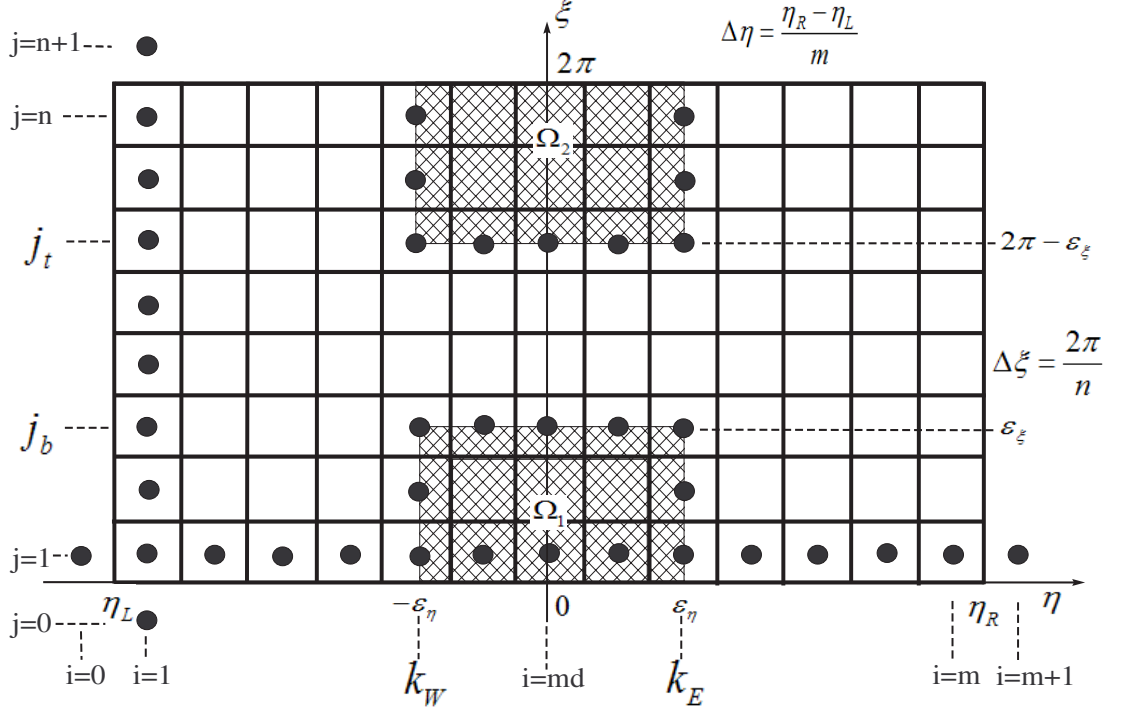


Figure 3.7 Location grid of temperature.

step (3.25) is

$$-A_i T_{i-1,j}^{k+1/2} + C_i T_{i,j}^{k+1/2} - B_i T_{i+1,j}^{k+1/2} = F_{i,j}, \quad (3.29)$$

$$i = 1, 2, \dots, k_W - 1, k_E + 1, \dots, m \quad \text{and} \quad j = 1, 2, \dots, j_b, j_t, \dots, n,$$

$$i = 1, 2, \dots, m \quad \text{and} \quad j = j_b + 1, \dots, j_t - 1$$

$$T_{0,j}^{k+1/2} = 2T_L - T_{1,j}^{k+1/2} \quad (3.30)$$

$$T_{m+1,j}^{k+1/2} = 2T_R - T_{m,j}^{k+1/2} \quad (3.31)$$

$$T_{k_W,j}^{k+1/2} = T_\infty, \quad j = 1, 2, \dots, j_b, j_t, \dots, n \quad (3.32)$$

$$T_{k_E,j}^{k+1/2} = T_\infty, \quad j = 1, 2, \dots, j_b, j_t, \dots, n \quad (3.33)$$

$$T_{i,j_b}^{k+1/2} = T_\infty, \quad i = k_W, \dots, k_E \quad (3.34)$$

$$T_{i,j_t}^{k+1/2} = T_\infty, \quad i = k_W, \dots, k_E \quad (3.35)$$

where

$$\begin{aligned}
A_i &= \frac{2\tau}{RePrJh^2\Delta\eta^2}, \\
B_i &= \frac{2\tau}{RePrJh^2\Delta\eta^2}, \\
C_i &= 1 + 2\frac{2\tau}{RePrJh^2\Delta\eta^2}, \\
F_{i,j} &= T_{i,j}^k + \frac{2\tau}{RePr}\Delta_{\xi\xi}T_{i,j}^k - \tau(\bar{v}^{m+1} \cdot \nabla)T_{i,j}^k.
\end{aligned}$$

For each fixed index j equations (3.29)-(3.35) are a system of linear algebraic equation with tridiagonal matrix. Algebraic system (3.29) is solved by LU factorization of tridiagonal matrix (“sweep” method, proposed by Yanenko (1971), Samarskii and Nikolaev (1989)). Details of the sweep method are represented in the Appendix A.

The finite difference approximation of the second fractional step (3.26) is

$$-\tilde{A}_j T_{i,j-1}^{k+1} + \tilde{C}_j T_{i,j}^{k+1} - \tilde{B}_j T_{i,j+1}^{k+1} = \tilde{F}_{i,j}, \quad (3.36)$$

$$i = 1, 2, \dots, k_W - 1, k_E + 1, \dots, m \quad \text{and} \quad j = 1, 2, \dots, n,$$

$$T_{i,j}^{k+1} = T_{i,j+n}^{k+1}, \quad (3.37)$$

and

$$-\tilde{A}_j T_{i,j-1}^{k+1} + \tilde{C}_j T_{i,j}^{k+1} - \tilde{B}_j T_{i,j+1}^{k+1} = \tilde{F}_{i,j}, \quad (3.38)$$

$$i = k_W, \dots, k_E \quad \text{and} \quad j = j_b + 1, \dots, j_t - 1,$$

$$T_{i,j_b}^{k+1} = T_\infty, \quad i = k_W, \dots, k_E, \quad (3.39)$$

$$T_{i,j_t}^{k+1} = T_\infty, \quad i = k_W, \dots, k_E, \quad (3.40)$$

where

$$\begin{aligned}\tilde{A}_j &= \frac{2\tau}{RePrJh^2\Delta\xi^2}, \\ \tilde{B}_j &= \frac{2\tau}{RePrJh^2\Delta\xi^2}, \\ \tilde{C}_j &= 1 + 2\frac{2\tau}{RePrJh^2\Delta\xi^2}, \\ \tilde{F}_{i,j} &= T_{i,j}^{k+1/2} + \frac{2\tau}{RePr}\Delta\xi\xi T_{i,j}^k.\end{aligned}$$

For each fixed index i equations (3.36) or (3.38) are represented by a system of linear algebraic equation with tridiagonal matrix. The algebraic system (3.36)-(3.37) is solved by the cyclic elimination method (Samarskii and Nikolaev (1989)). Algebraic system (3.38)-(3.40) is solved by the elimination method for three-point equation (Samarskii and Nikolaev (1989)). Details of cyclic elimination method are presented in Appendix B.

3.4 Computation of flow characteristics

3.4.1 Drag and lift coefficients

To evaluate the integrals in equation (2.22) we used the middle point rule, for example, in order to compute C_{D_p} we used formula:

$$C_{D_p}|_i = \sum_{j=1}^n \left\{ hp \left[\left(\frac{h}{a} (\cosh \eta \cos \xi - 1) \right) n_\xi + \left(-\frac{h}{a} \sinh \eta \sin \xi \right) n_\eta \right] \right\}_{i,j} \Delta\xi, \quad (3.41)$$

where $i = L, R$, that is, we computed the coefficient on the left and right cylinder surfaces, respectively. Here we approximated pressure on the cylinders by extrapolation from interior points (see in Figure 3.8):

$$p_{L,j} = \frac{15}{8}p_{1,j} - \frac{5}{4}p_{2,j} + \frac{3}{8}p_{3,j}, \quad (3.42)$$

$$p_{R,j} = -\frac{15}{8}p_{m,j} + \frac{5}{4}p_{m-1,j} - \frac{3}{8}p_{m-2,j}. \quad (3.43)$$

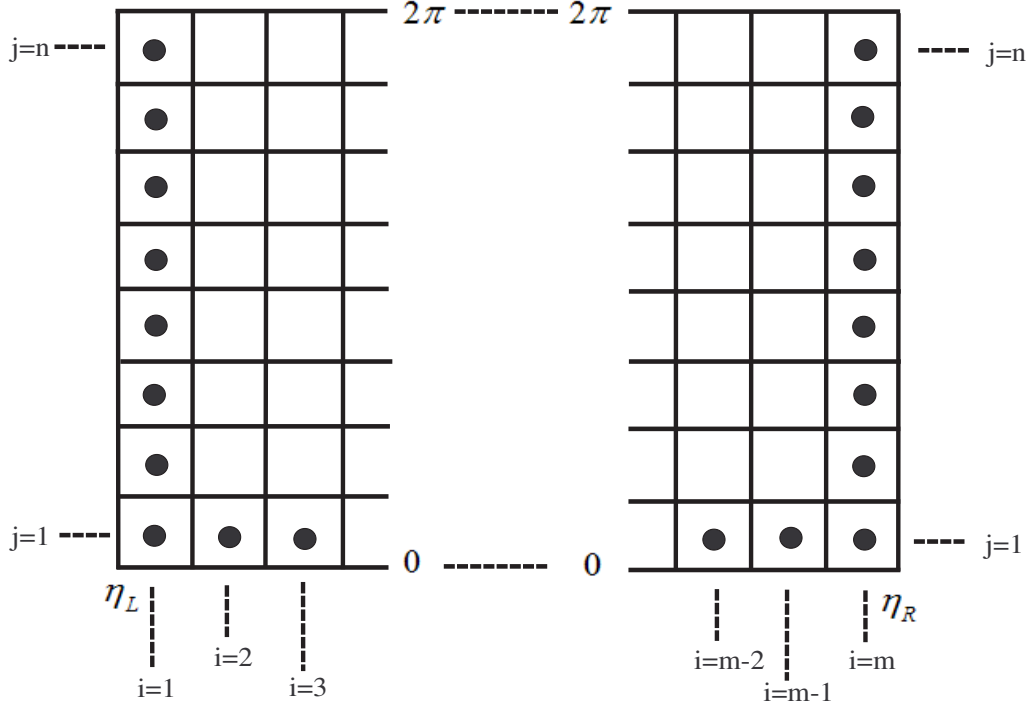


Figure 3.8 Structure of grid: using compute force acting on cylinders surface.

3.4.2 Vorticity on the cylinder surfaces

For finding the vorticity, we used the following formula

$$\omega = -\frac{1}{h} \left[\frac{\partial v}{\partial \eta} - \frac{\partial u}{\partial \xi} - \frac{h}{a} (\sinh \eta v - \sin \xi u) \right].$$

On the circular cylinder surfaces the spatial derivatives $\frac{\partial u}{\partial \xi} = 0$ and $\frac{\partial v}{\partial \eta}$ we approximated by one-side difference

$$\left(\frac{\partial v}{\partial \eta} \right)_{L,j} = -\frac{8}{3}v_L + 3v_{1,j}^{n+1} - \frac{1}{3}v_{2,j}^{n+1}, \quad (3.44)$$

$$\left(\frac{\partial v}{\partial \eta} \right)_{R,j} = \frac{8}{3}v_R - 3v_{m,j}^{n+1} + \frac{1}{3}v_{m-1,j}^{n+1}. \quad (3.45)$$

3.4.3 Nusselt number

In Chapter II, we gave the definition of the local Nusselt number as:

$$Nu = - \left(\frac{\partial T}{\partial n} \right)_{wall}.$$

In order to compute the average Nusselt number, we approximated the integral by the middle point rule (the index used here can see from the Figure 3.8):

$$\bar{Nu} = \sum_{j=1}^n \left[\frac{1}{2\pi} \frac{\partial T}{\partial \eta} \right]_{i,j} \Delta \xi, \quad i = L, R, \quad (3.46)$$

where

$$\left. \frac{\partial T}{\partial \eta} \right|_{L,j} = \frac{T_{1,j} - T_{0,j}}{\Delta \eta}, \quad (3.47)$$

$$\left. \frac{\partial T}{\partial \eta} \right|_{R,j} = \frac{T_{m+1,j} - T_{m,j}}{\Delta \eta}. \quad (3.48)$$

CHAPTER IV

VALIDATION

Validation is usually accomplished by benchmarking the numerical results against the available reliable numerical and/or experimental predictions for the analogous problem. In order to validate the computational code, two-dimensional simulations in a Reynolds number range $0 \leq Re \leq 45$ have been carried out. The Reynolds number is defined in terms of the right cylinder diameter D_R and the free stream velocity U_∞ , $Re = U_\infty D_R / \nu$. Since it is well known that for a large gap spacing between the surface of two cylinders the mutual influence between cylinders disappears, we can assume that the flow and heat transfer will be similar to flow and heat transfer over a single cylinder. Thus the comparisons of the characteristics of flow and heat transfer of our numerical results (gap spacing $g = 14, g = (d - r_L - r_R) / D_R$) with the published data for single cylinder were carried out. All computational experiments have been performed in a large domain in order to reduce the influence on the outer boundary. The sequence of the uniform grid is used. The wake behind the cylinder is steady in the flow regime $Re \leq 46 \pm 1$.

We divided our validation into two parts. In the first part we compared the characteristics of flow and heat transfer over two circular cylinders ($g = 14$) without rotation. In the second part, comparison of characteristics of flow past two rotating circular cylinders for large gap spacing ($g = 14$) are shown.

4.1 Characteristics of flow and heat transfer over two circular cylinders without rotation in large gap spacing

The numerical simulations are presented here for Reynolds numbers $Re = 10, 20, 30,$ and 40 where the flow is steady. Our data come from simulations with the grids size $21 \times 21, 41 \times 41,$ and 81×81 in the $\xi - \eta$ plane. In all of the comparisons in this section, we used large gap spacing $g = 14$ to compare the characteristics of flow. By symmetry assumption, for large gap spacing all our presentations are made for the left cylinder. The outer boundary is located far from the cylinders (greater than 40 cylinder diameters away from the cylinder). The numerical methodology used in our work has been validated extensively in terms of the total drag coefficient, pressure coefficient, vorticity on the cylinders surface, streamline, temperature pattern, local and average Nusselt number.

The hydrodynamic drag force exerted by the fluid on the solid cylinders is determined by the individual contributions due to the pressure and frictional forces acting on the cylinders and can be expressed in terms of dimensionless drag coefficients (frictional drag C_{D_f} , pressure drag C_{D_p} , and total drag C_D). The dependence of the drag coefficients on the Reynolds number is shown in Figure 4.1 and Tables 4.1, 4.2. Representative results showing the variation of the pressure coefficient (C_p) and vorticity (ω) on the surface of the left cylinder are plotted in Figure 4.1 for two values of the Reynolds number $Re = 20$ and 40 and for gap spacing $g = 14$.

Comparison of our numerical simulations is performed with the numerical results of Dennis and Chang (1970) for $Re = 20$ and 40 and with the experimental results of Thom for $Re = 36, 45$ and Apelt for $Re = 40$ (see in Batchelor (2000)). Our data come from simulations with the grid size 81×81 in the $\xi - \eta$ plane.

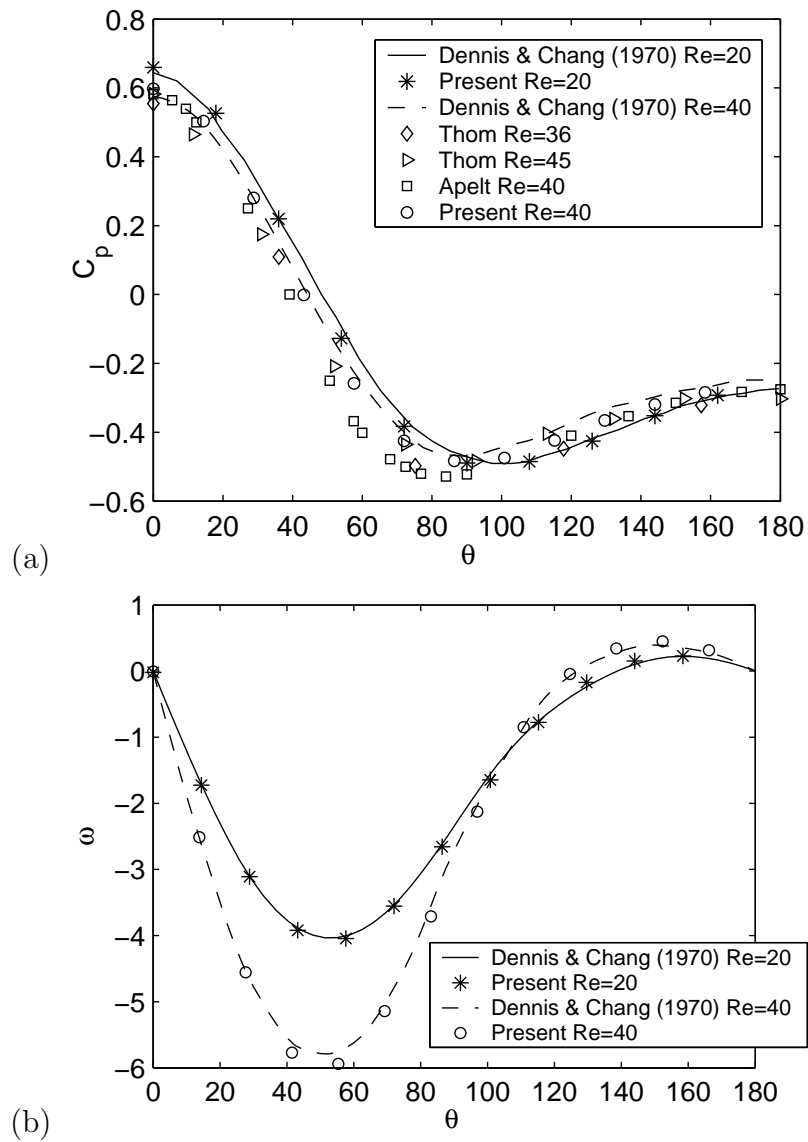


Figure 4.1 (a) Pressure coefficient over cylinder surface, (b) the vorticity distribution over cylinder surface, for the left cylinder at $Re = 20, 40$, and $g = 14$.

Table 4.1 Validation of the numerical algorithm; comparison study for flow over two side-by-side circular cylinders at $g = 14$ with flow over a single cylinder.

Re	Contribution	C_D	C_{D_p}	C_{D_f}	L_W/D
	Present study (81×81)	2.798	1.572	1.226	—
	Juncu (2007)	2.722	1.526	1.196	—
10	Soares <i>et al.</i> (2005)	2.760	1.550	1.210	0.25
	Dennis <i>et al.</i> (1970)	2.846	1.600	1.246	0.27
	Stålberg <i>et al.</i> (2006)	2.840	1.589	1.251	0.29
	Present study (81×81)	2.064	1.242	0.822	0.925
	Sungnul and Moshkin (2006)	2.120	1.270	0.850	0.934
	Relf (1913) (one cylinder)	2.160	—	—	—
	Tritton (1959) (one cylinder)	2.080	—	—	—
20	Chung (2006) (one cylinder)	2.050	—	—	0.960
	Ingham <i>et al.</i> (1990) (one cylinder)	1.995	1.201	0.794	—
	Batchelor (2000) (one cylinder)	2.001	—	—	0.900
	Dennis <i>et al.</i> (1970)	2.045	1.233	0.812	0.94
	Stålberg <i>et al.</i> (2006)	2.051	1.229	0.823	0.90
	Fornberg (1980)	2.000	—	—	0.91
	Soares <i>et al.</i> (2005)	1.990	1.190	0.800	0.925

Table 4.2 Validations of the numerical algorithm; comparison study for flow over two side-by-side circular cylinder at $g = 14$ with flow over a single cylinder.

Re	Contribution	C_D	C_{D_p}	C_{D_f}	L_W/D
	Present study (81×81)	1.738	1.098	0.640	—
30	Juncu (2007)	1.655	1.044	0.611	—
	Takami <i>et al.</i> (1969)	1.717	—	—	1.611
	Soares <i>et al.</i> (2005)	1.670	1.040	0.630	1.600
	Present study (81×81)	1.590	1.050	0.541	2.15
	Sungnul and Moshkin (2006)	1.539	1.002	0.537	2.160
	Relf (1913) (one cylinder)	1.620	—	—	—
40	Tritton (1959) (one cylinder)	1.590	—	—	—
	Chung (2006) (one cylinder)	1.540	—	—	2.300
	Batchelor (2000) (one cylinder)	1.538	—	—	2.150
	Dennis <i>et al.</i> (1970)	1.522	0.998	0.524	2.35
	Stålberg <i>et al.</i> (2006)	1.530	0.994	0.536	2.13
	Soares <i>et al.</i> (2005)	1.490	0.960	0.530	2.275

The closest distance to the far boundary for this grid is located about 53 cylinder diameters away from the cylinder. The angle variable θ is zero at front stagnation point and increases in the clockwise direction in the left cylinder. The data from our simulations (* - sign for $Re = 20$ and \circ - sign for $Re = 40$) match the results of Dennis and Chang (1970), Thom and Apelt very well for $Re = 20$ and 40. Tables 4.1 and 4.2 summarize the quantities measured in our study and compare them with numerical and experimental results from other publications. The pressure, viscous and total drag coefficients, C_{D_p} , C_{D_f} , C_D defined by equations (2.22) are presented. The separation bubble length, L_W/D , is measured as the distance from

the rare stagnation point on the cylinder surface to the point where the streamwise velocity is zero and normalized with the cylinder diameter.

Figures 4.2-4.3 shows the steady-state streamlines, pressure fields, and iso-lines of temperature for two Reynolds numbers $Re = 20$ and 40 , $g = 14$, $Pr = 1$, 10 , and 20 . Due to the symmetry about the y -axis all patterns are presented only around the left cylinder. Dependence of main characteristics of flow (C_D , C_{D_f} , C_{D_p} , and \overline{Nu}) on the grid resolution is demonstrated in Table 4.3 for $Re = 20$, $g = 14$ and $Pr = 0.7$. Three grid sizes are investigated 21×21 ($\Delta\xi = 0.312$, $\Delta\eta = 0.332$), 41×41 ($\Delta\xi = 0.156$, $\Delta\eta = 0.166$), and 81×81 ($\Delta\xi = 0.078$, $\Delta\eta = 0.083$). The minimal distance from cylinder surface to the far boundary is about $10.5D$ for the coarse grid and about $53D$ for the fine grid.

Table 4.3 Effect of grid refinement upon C_D , C_{D_p} , C_{D_f} , and average Nusselt number Nu for $Re = 20$ and $g = 14$.

Source	C_D	C_{D_p}	C_{D_f}	$Nu (Pr = 0.7)$
Present study (21×21)	2.149	1.274	0.875	2.669
Present study (41×41)	2.112	1.274	0.838	2.481
Present study (81×81)	2.064	1.242	0.822	2.478
Soares <i>et al.</i> (2005)	1.990	1.190	0.800	2.430

The case of flow past a single cylinder was used to test the prediction of Nusselt number (Nu). For the range of $Re = 10$, 20 , and 40 and a Prandtl number $Pr = 0.7$ (corresponding to the flow of air) the numerical values of average Nusselt number for the constant temperature boundary condition were found to be in excellent agreement with previous results available in the literature (Table

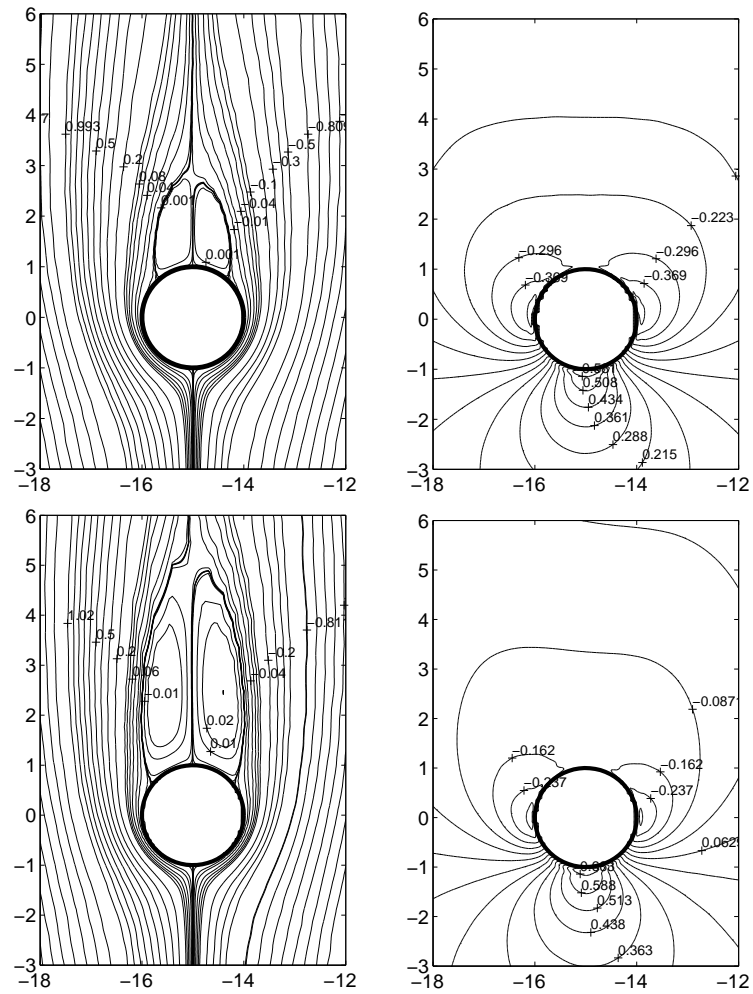


Figure 4.2 1st-column: Streamline patterns, 2nd-column: pressure fields of flow over two circular cylinders for $g = 14$, $\alpha = 0$ at 1st-row: $Re = 20$, 2nd-row: $Re = 40$.

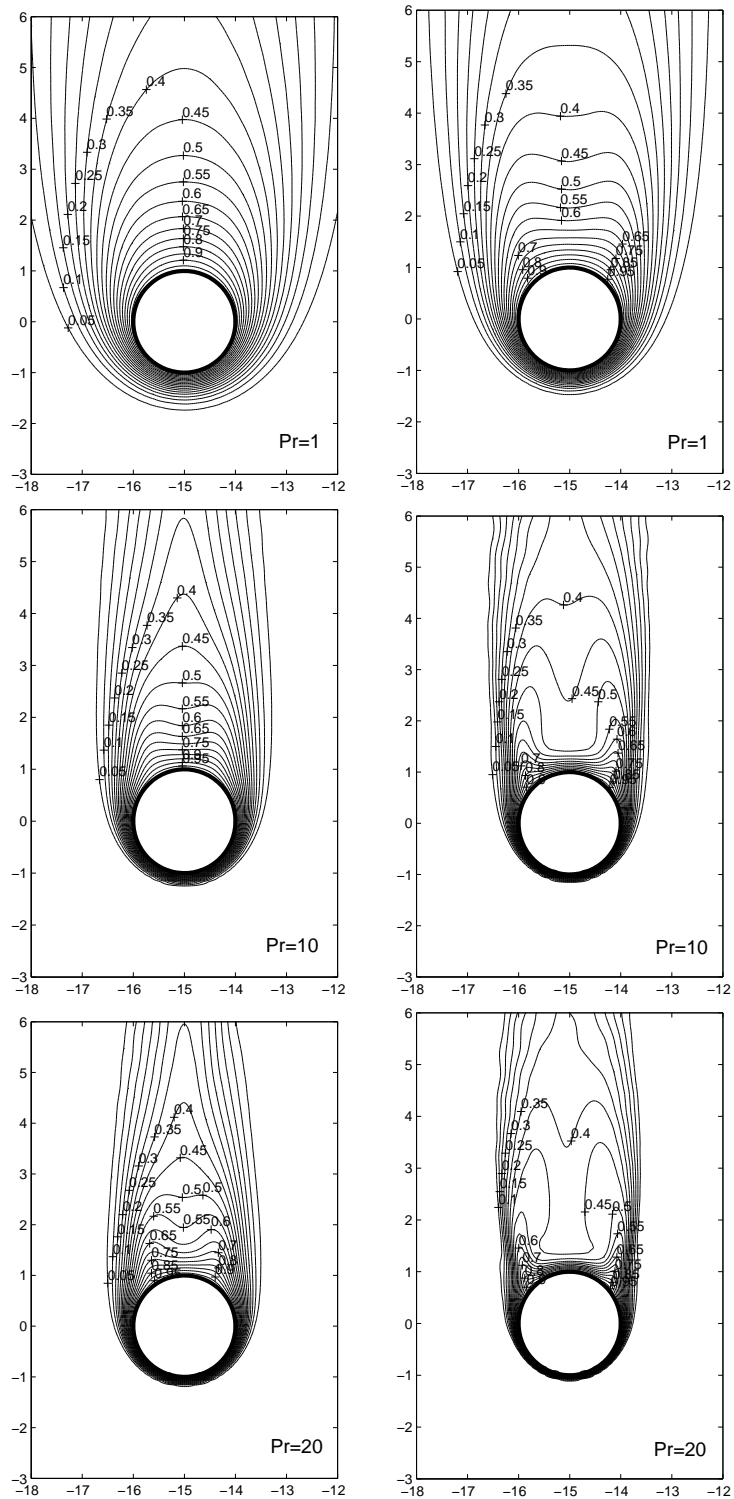


Figure 4.3 The temperature contours for 1st-column: $Re = 20$ and 2nd-column: $Re = 40$ of flow over two circular cylinders for $g = 14$, $\alpha = 0$ at 1st-row: $Pr = 1$, 2nd-row: $Pr = 10$, and 3rd-row: $Pr = 20$.

4.4)

Table 4.4 Comparison of the average Nusselt number at $Pr = 0.7$, $g = 14$, $\alpha = 0$ for grid 21×21 , 41×41 , and 81×81 with the values found in the literature.

Source	Nu		
	$Re = 10$	$Re = 20$	$Re = 40$
Present study (21×21)	1.892	2.670	3.796
Present study (41×41)	1.873	2.481	3.425
Present study (81×81)	1.850	2.478	3.333
Bharti <i>et al.</i> (2007)	1.862	2.465	3.282
Badr (1983)	—	2.540	3.480
Dennis <i>et al.</i> (1968)	1.867	2.521	3.431
Lange <i>et al.</i> (1998)	1.810	2.408	3.280
Soares <i>et al.</i> (2005)	1.860	2.430	3.200
Sparrow <i>et al.</i> (2004)	1.602	2.205	3.082

Table 4.5 summarizes our computations for large gap spacing, $g = 14$ between cylinders in stream perpendicular to line of the cylinder centers. The values of average Nusselt numbers (defined by equation (3.46)) for the range of Reynolds numbers $Re = 10, 20, 30$, and 40 and for the range of Prandtl numbers $Pr = 0.7, 1.0, 7.0, 10, 20$, and 50 are presented in Table 4.5.

Colburn j-factor analogy is probably the most successful and widely used analogy from heat, momentum, and mass transfer analogies. The basic mechanisms and mathematics of heat, mass, and momentum transport are essentially the same. Among many analogies (like Reynolds analogy and Prandtl analogy) developed to directly relate heat transfer coefficients, mass transfer coefficients,

Table 4.5 Comparison of the average Nusselt numbers for cylinders with constant temperature for $g = 14$.

Re	Pr	Nu			
		Present study	Bharti (2007)	Juncu (2007)	Soares (2005) Lange (1998)
10	0.7	1.850	1.862		1.862 1.810
	1	2.082	2.214	2.560	
	7	3.858	3.857		
	10	4.329	4.286	4.257	
	20	5.438	5.429		
	50	7.418	7.214		
20	0.7	2.478	2.465		2.465 2.408
	1	2.787	2.857	2.730	
	7	5.286	5.214		
	10	6.041	5.857	5.729	
	20	7.631	7.357		
	50	10.780	9.929		
30	0.7	2.936	2.929		
	1	3.310	3.357	3.229	
	7	6.397	6.286		
	10	7.294	7.071	6.937	
	20	9.605	9.000		
	50	13.141	12.214		
40	0.7	3.333	3.283		3.282 3.280
	1	3.773	3.714		
	7	7.533	7.214		
	10	8.727	8.214		
	20	11.471	10.357		
	50	17.401	14.286		

and friction factors, Colburn j -factor analogy proved to be the most accurate. As expected, the average Nusselt number increases with the Reynolds number and/or Prandtl number. Further analysis of our data demonstrate that the Nusselt number exhibits the classical dependence on Prandtl number, i.e. $Nu \propto Pr^{1/3}$. This allows the reconciliation of the results for different Prandtl number through use of j -factor as shown in Figure 4.5. The present results for $10 \leq Re \leq 40$ and $0.7 \leq Pr \leq 50$ compare with the expression

$$j = 0.6738 Re^{-0.5321} \quad (4.1)$$

by Bharti *et al.* (2007) (represent by dashed line in Figure 4.5) for the constant cylinder temperature.

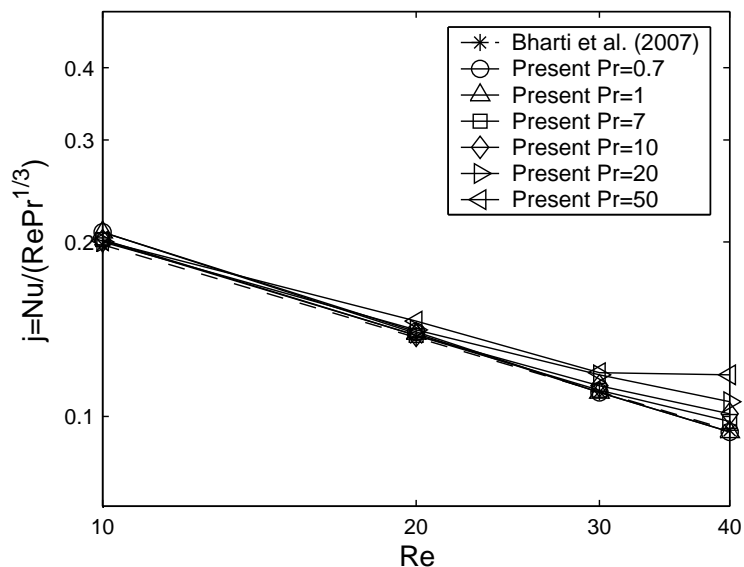


Figure 4.4 Colburn j -factor as a function of the Reynolds number at different Prandtl number.

The variation of the local Nusselt number on the surface of the left cylinder at $Re = 10, 20, 40$, $g = 14$ for a range of Prandtl numbers $0.7 \leq Pr \leq 50$ is shown in Figure 4.6. For comparison we plotted the data (Bharti *et al.* (2007)) for a single cylinder with a dotted line for $Pr = 1$, dash-dot line for $Pr = 10$

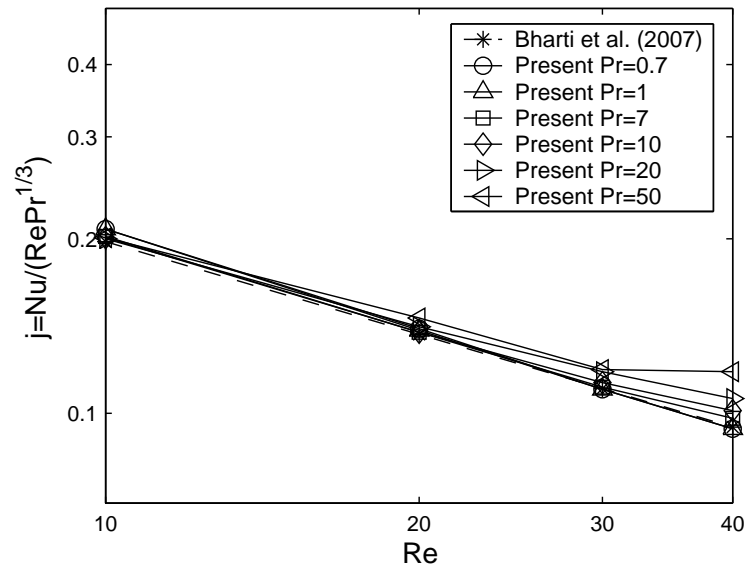


Figure 4.5 Colburn j -factor as a function of the Reynolds number at different Prandtl number.

and dashed line for $Pr = 20$. The variation of the local Nusselt number over the surface of the left cylinder at $Pr = 1$, $g = 14$ for the range of Reynolds numbers is shown in Figure 4.7.

Figure 4.8 shows the effect of grid size on the local Nusselt number on the surface of the left cylinder for $Re = 20$, $Pr = 1.0$, and $g = 14$. For comparison, the results from Bharti *et al.* (2007) are plotted by a solid line.

Since the present results of our simulation are in satisfactory agreement with other data available to the authors data, it is thus believed that the numerical parameters and algorithms used in this works are justified. The large discrepancy in average Nusselt number for large Prandtl number can be explained by increased value of heat diffusion, and as a result the presence of the second cylinder does not allow to assume similarity of heat transfer between flow over two side-by-side cylinder and one single cylinder.

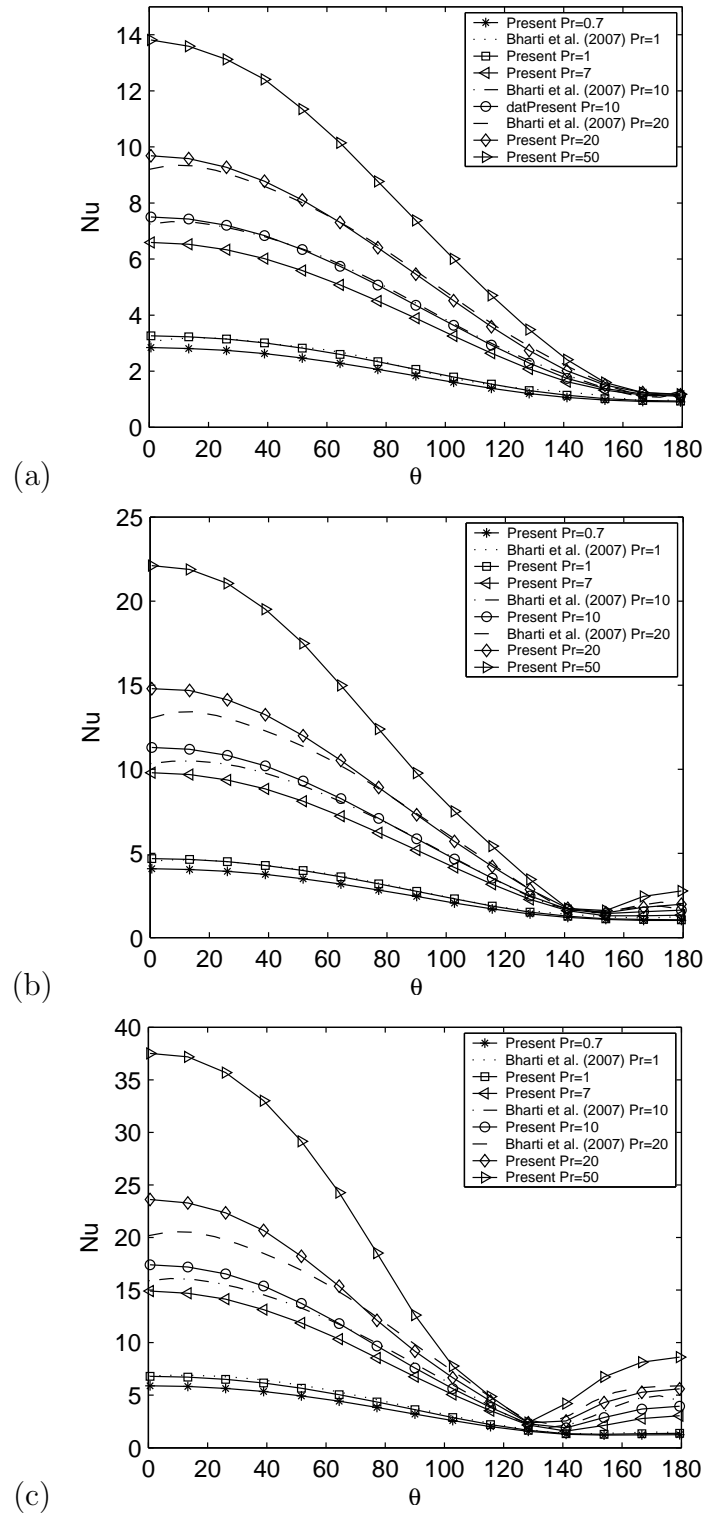


Figure 4.6 Local Nusselt number variation on the surface of the circular cylinders for $\alpha = 0$, $g = 14$, and (a) $Re = 10$, (b) $Re = 20$, (c) $Re = 40$ at various Prandtl numbers.

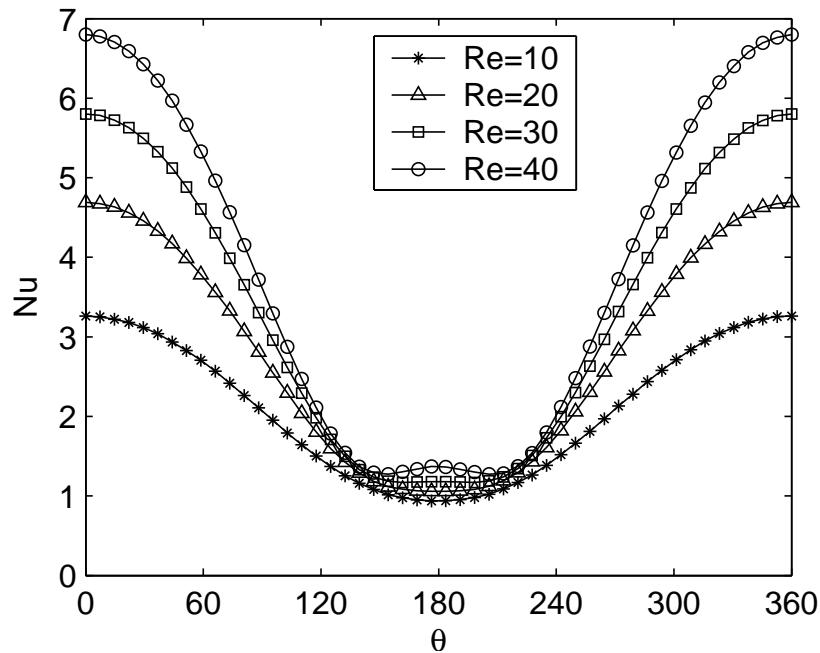


Figure 4.7 Local Nusselt number variation on the surface of the circular cylinders at $Pr = 1$, $g = 14$ at various Reynolds numbers.

4.2 Characteristics of flow and heat transfer over two rotating circular cylinders in large gap spacing

In this section, we present our numerical results for the flow past two rotating circular cylinders of equal radii in side-by-side arrangement for large gap spacing $g = 14$, range of Reynolds number $Re \leq 40$ and rate of rotation $0.1 \leq \alpha \leq 2$. The left cylinder rotates with constant angular velocity in clockwise direction and the right cylinder rotates with the same angular velocity in counterclockwise direction.

To the author's knowledge, there are very few published data of drag and lift coefficients at $Re \leq 40$ and non zero angular velocity even for flow past single cylinders. Table 4.6 shows the comparison of drag and lift coefficients at $Re = 20$ in range of $0.1 \leq \alpha \leq 2$ with those numerically obtained by Sungnul and

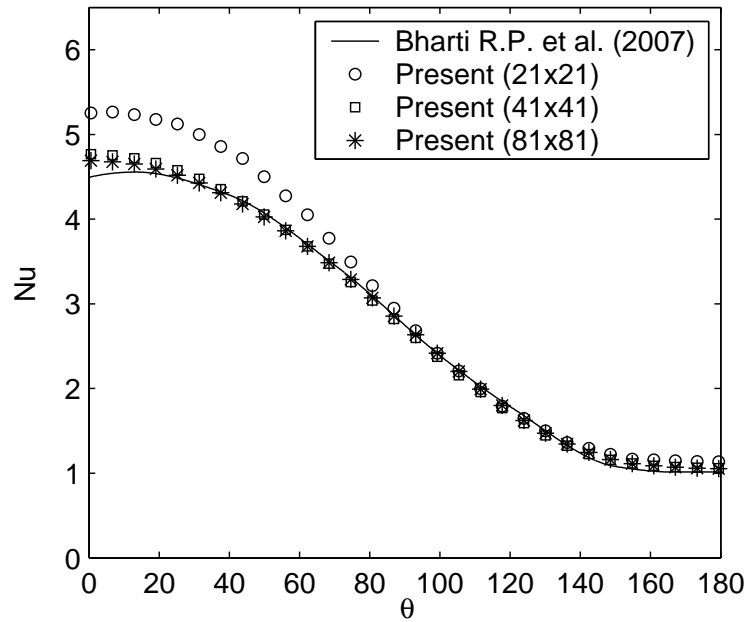


Figure 4.8 Local Nusselt number on the sequence of grids for $Re = 20$, $g = 14$, and $Pr = 1$.

Moshkin (2006), Badr *et al.* (1989), Ingham *et al.* (1990), and Chung (2006). The comparisons show that the present results are in a good agreement.

Due to symmetry we only represent the streamline, pressure fields and temperature contours around the left cylinder in Figure 4.9. From the previous studies by Batchelor (2000), M.H. Chung (2006), and Sungnul and Moshkin (2006), the streamline patterns at large gap spacing $g = 14$ of our results do not contradict the results in the flow behind a single cylinder.

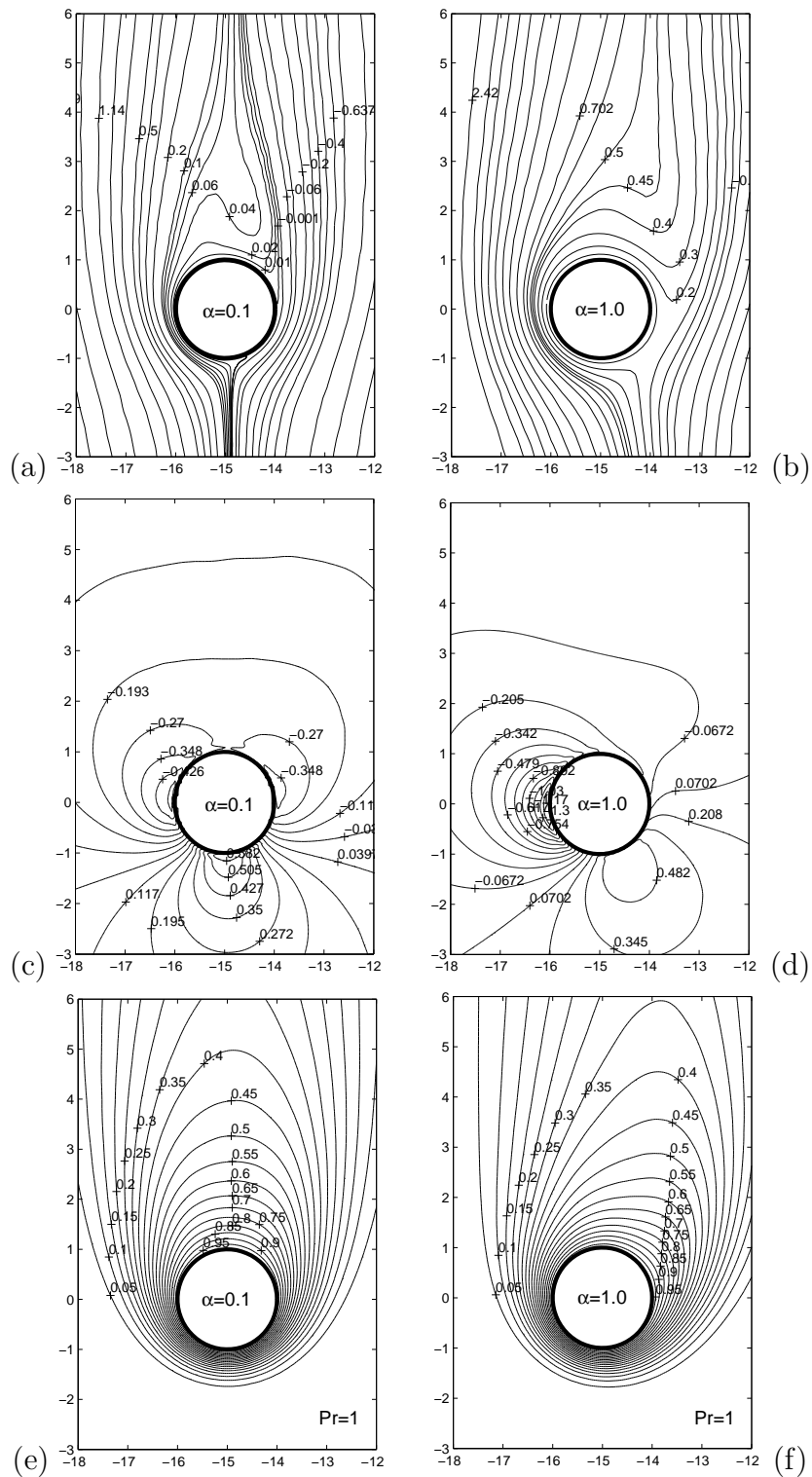


Figure 4.9 (a-b) Streamline patterns, (c-d) pressure fields and (e-f) temperature contours of flow over two circular cylinders at $Re = 20$, $g = 14$, and $Pr = 1.0$, left column: $\alpha = 0.1$, right column: $\alpha = 1.0$.

Table 4.6 Hydrodynamic parameters of flow over a rotating circular cylinder at $Re = 20$ with $g = 14$.

Contribution	C_D			C_L		
	$\alpha = 0.1$	$\alpha = 1.0$	$\alpha = 2.0$	$\alpha = 0.1$	$\alpha = 1.0$	$\alpha = 2.0$
Present study (21×21)	2.146	2.035	1.906	0.286	2.974	6.309
Present study (41×41)	2.108	1.897	1.410	0.288	2.864	6.030
Present study (81×81)	2.052	1.847	1.346	0.293	2.770	5.825
Sungnul and Moshkin (80×80)	2.120	1.887	1.363	0.291	2.797	5.866
Badr <i>et al.</i> (1989)	1.990	2.000	—	0.276	2.740	—
Ingham <i>et al.</i> (1990)	1.995	1.925	1.627	0.254	2.617	5.719
Chung (2006)	2.043	1.888	1.361	0.258	2.629	5.507

CHAPTER V

NUMERICAL RESULTS

The characteristics of heat transfer in two-dimensional laminar flow past two rotating circular cylinders of the same radius in a side-by-side arrangement at a various range of absolute rotation speed ($|\alpha| \leq 2.5$) for a variety of gap spacing were investigated. The results are represented in terms of isothermal patterns, distribution of local Nusselt number on the surface of the cylinders and the average Nusselt number for the ranges of parameters $10 \leq Re \leq 40$, $0.7 \leq Pr \leq 20$, and constant temperature boundary conditions. Due to the symmetry all results are presented for the left cylinder only. The left cylinder rotates with constant angular velocity in the clockwise direction and the right cylinder rotates with the same angular velocity in the counterclockwise direction as shown in Figure 2.1.

5.1 Effect of gap spacing (zero rotation)

For large gap spacing, $g = 14$ and $\alpha = 0$ the variation of the local Nusselt number for $Re = 10, 20$, and 40 for the range of Prandtl number $0.7 \leq Pr \leq 50$ is shown in Figures 4.6 - 4.8. As expected, the Nusselt number increases with an increase in the Reynolds number and/or Prandtl number. These figures show that the largest values of Nu correspond to the front stagnation point $\theta = 0$. The angle variable θ is zero at point $x = -d_L$, $y = -r_L$ (front stagnation point in the case of flow past cylinder without rotation) and θ increases in clockwise direction on the surface of the left cylinder. The value of the local Nusselt number decreases along the surface of the cylinder as θ increases in the clockwise direction. The minimum

value of $Nu(\theta)$ appears near the point of separation. A gradual increase in the values of the local Nusselt number can be observed with an increase in the Reynolds number and Prandtl number in the rear part of cylinder. The influence of the gap spacing on the heat transfer rate in terms of the local Nusselt number $Nu(\theta)$ is shown by Figure 5.1 for $Re = 20$, $\alpha = 0$, and $Pr = 0.7, 1, 10, \text{ and } 20$. This figure shows that a significant influence of the distance between cylinders on the local Nusselt number $Nu(\theta)$ is observed for $g \lesssim 5$. Another aspect that seems to be interesting is the decreasing $Nu(\theta)$ for $0^\circ < \theta < 360^\circ$ with decreasing g in the cases of $Pr = 0.7$ and 1.0 (rate of convection and conduction are almost equal). In the cases of $Pr = 10$ and 20 (convection is the dominant mechanism of heat transfer) $Nu(\theta)$ decreases with g decreasing for $0^\circ < \theta < 180^\circ$ and $270^\circ < \theta < 360^\circ$, and for $180^\circ < \theta < 270^\circ$ the values of $Nu(\theta)$ increases with g increasing. It must be mentioned that as g increases convergence of the local Nusselt number to the local Nusselt number for a single cylinder have been observed for all Prandtl numbers. This can be written in symbolic form as $\lim_{g \rightarrow \infty} Nu(\theta, g) = Nu(\theta, \infty)$. It is not surprising that the average Nusselt number for each individual cylinder increases with increasing gap spacing and tends to the average Nusselt number for a single cylinder. The average Nusselt number is obtained by averaging the local Nusselt number over the surface of cylinders (see Equation (2.34)). Table 5.1 and Figure 5.2 show the variation of the average Nusselt number with gap spacing between nonrotating cylinders at different Prandtl numbers and fixed Reynolds number $Re = 20$. As expected, the average Nusselt number for the cylinders increases with the Prandtl number.

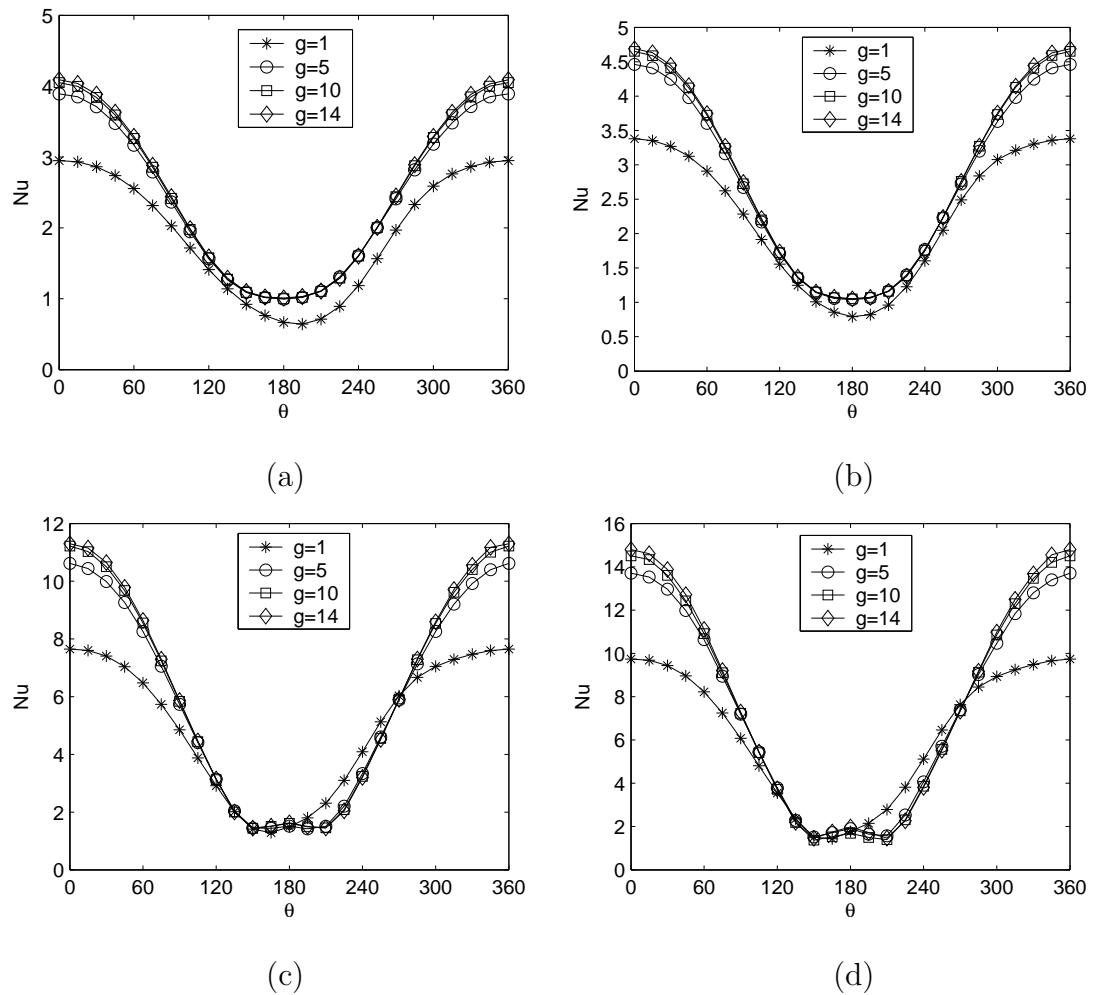


Figure 5.1 Local Nusselt number for different gap spacing at $Re = 20$, $\alpha = 0$, and (a) $Pr = 0.7$, (b) $Pr = 1$, (c) $Pr = 10$, and (d) $Pr = 20$.

5.2 Large gap spacing (effect of rotation)

The effect of steady rotation on heat transfer is discussed in this section for the case of large gap spacing, $g = 14$. Thus, the results of this paragraph can be considered as illustrating the influence of rotation on heat/mass transfer in the flow around single rotating circular cylinder. Cases with three Reynolds numbers, $Re = 10$, 20 , and 40 were selected for presentation. Prandtl numbers vary from 0.7 up to 20 to represent the range of moderate to high convection rate.

Figure 5.3 shows the effect of the rotation rate α on the local Nusselt number

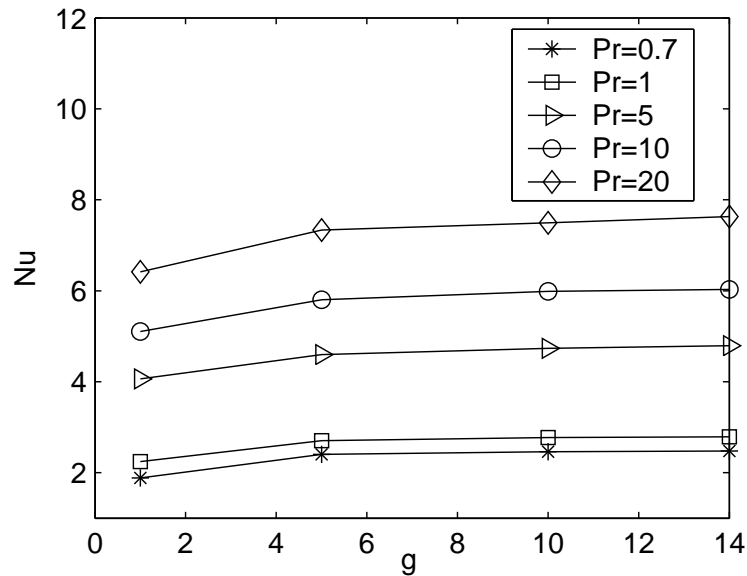


Figure 5.2 Average Nusselt number for different gap spacing at $Re = 20$, $\alpha = 0$.

Table 5.1 Variation of the average Nusselt number at $Re = 20$ and $\alpha = 0$.

	$Pr = 0.7$	$Pr = 1$	$Pr = 5$	$Pr = 10$	$Pr = 20$
$g = 1$	1.886	2.247	4.064	5.105	6.418
$g = 5$	2.403	2.703	4.598	5.802	7.335
$g = 10$	2.459	2.771	4.736	5.988	7.494
$g = 14$	2.478	2.787	4.792	6.041	7.631

at constant $Re = 20$. As α increases, the points of maximum and minimum of the local Nusselt number shift in direction of rotation. For the case of zero rotation, $\alpha = 0$, the maximum value of $Nu(\theta)$ is at $\theta = 0^\circ$ (the front stagnation point) and the minimum value of $Nu(\theta)$ is observed near the rear stagnation point, $\theta = 180^\circ$. For larger Pr numbers, $Pr = 10$ and 20 , there are two local minima which appear near the separation points. The non zero rotation substantially changes the flow field and temperature distribution in the vicinity of the cylinder. Without rotation, the flow field exhibits a asymmetric pair of standing vortices behind the

cylinder defining a closed recirculation region (see for example Figure ??). With an increasing rotation rate the flow becomes asymmetric, the vortex detaches from the cylinder and the stagnation point rotates in the direction opposite to the direction of the cylinder rotation departing from the surface of cylinder. The details of steady flow and thermal field are presented in Figures 5.4 - 5.5 (for the case $Re = 20$, $g = 14$, $Pr = 1$, and 20 , and $\alpha = 0.1$, 1.0 , and 2.0) in the form of streamlines and constant temperature contours. It is seen that the stagnation point for small speed of rotation $\alpha = 0.1$ is slightly shifted counter-clockwise and located in the interval $350^\circ < \theta < 359^\circ$ (see Figure 5.4). For larger speed of rotation $1 \leq \alpha \leq 2$, the stagnation point shift more significantly and is located in the interval $270^\circ < \theta < 340^\circ$. The point of maximum clustering of the temperature isotherms which indicates high temperature gradient (and thus highest local Nusselt number) shift in the clockwise direction and is located in the interval $0^\circ < \theta < 70^\circ$ at the “west” side of the cylinder surface (see Figure 5.5). The clustering of isotherms near the cylinder surface increases with an increase in the Prandtl number and/or α (compare first, second and third row in Figure 5.5). This behavior is quite expected due to the no-slip condition, the fluid layer adjacent to the cylinder surface wraps around the cylinder and rotates with almost the same angular velocity. When α increases, this layer becomes thinner and a larger amount of fluid rotates with the cylinders. For large Prandtl number $Pr = 10$ and 20 , convection is the dominant mechanism of heat transfer which explains the higher clustering of temperature isotherm for large Pr number.

Table 5.2 and Figure 5.6 show the dependence of the average Nusselt number on rotational speed for $Re = 10$, 20 , and 40 , $g = 14$, and $Pr = 0.7$, 1 , 5 , 10 , and 20 . The average Nusselt number decreases with increasing α as show in Table 5.2 and Figure 5.6. For example, in the case of $Re = 20$, the average Nusselt num-

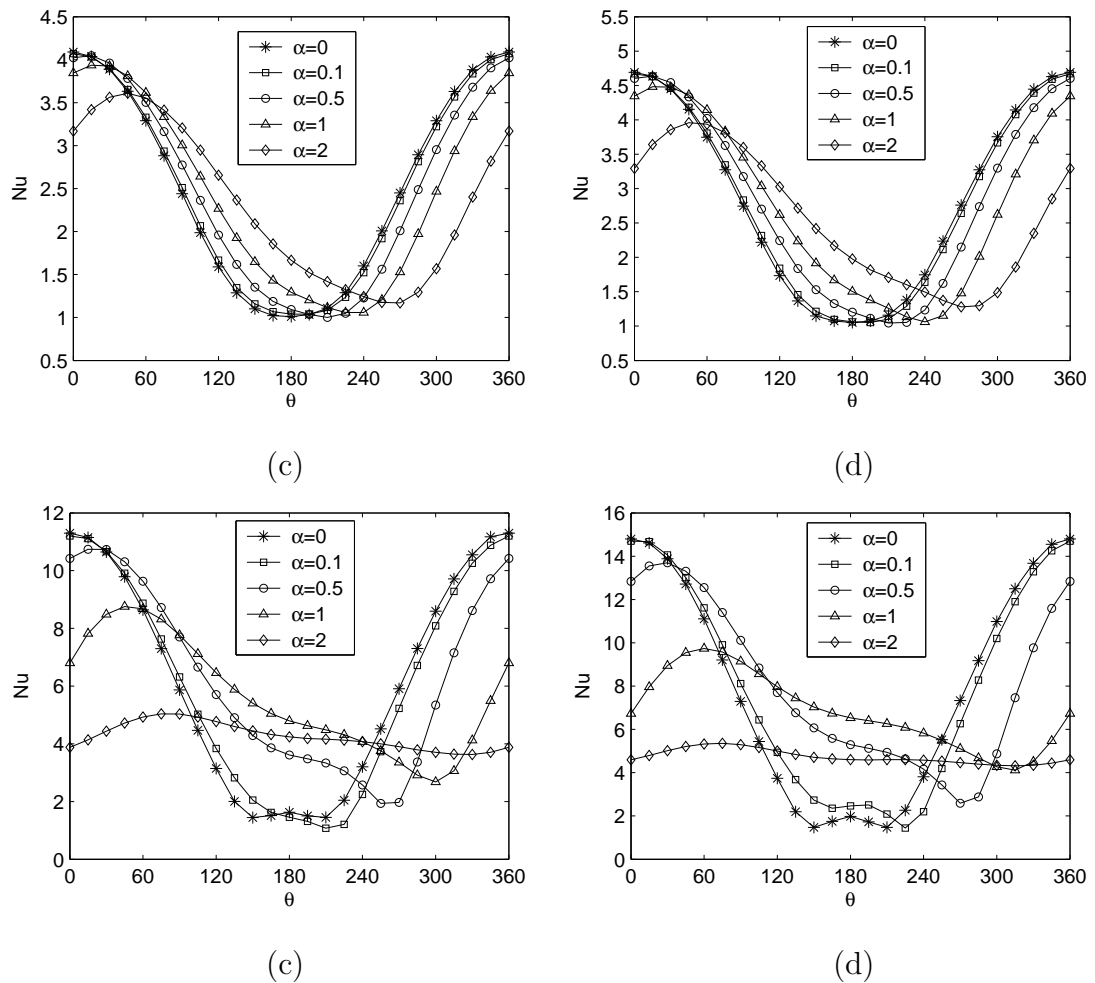


Figure 5.3 Local Nusselt number variation on the surface of the circular cylinders at $Re = 20$, $g = 14$, $\alpha = 0, 0.1, 0.5, 1$, and 2 for (a) $Pr = 0.7$, (b) $Pr = 1$, (c) $Pr = 10$, and (d) $Pr = 20$.

ber for $Pr = 1$ drops down by 10% and for $Pr = 20$, the average Nusselt number drops down by almost 50% when α increases from 0 up to 2. This behavior can be explained by the existence of a fluid buffering layer which wraps around the cylinder and rotates together with cylinder. For small rotational speed, $0 < \alpha < 0.5$, the average Nu number decreases slightly with increasing α (only by a few percentage points). For larger values of α , the average Nu number decreases almost linearly with α increase from 0.5 up to 2.0.

Table 5.2 Variation of average Nusselt number at $g = 14$.

Re	α	Pr				
		0.7	1	5	10	20
10	0.0	1.850	2.082	3.510	4.329	5.438
	0.5	1.849	2.069	3.487	4.389	5.579
	1.0	1.816	2.027	3.307	4.029	4.813
	1.5	1.787	1.983	3.095	3.654	4.195
	2.0	1.752	1.929	2.862	3.293	3.688
20	0.0	2.479	2.787	4.792	5.965	7.631
	0.1	2.472	2.774	4.790	5.915	7.678
	0.5	2.450	2.753	4.811	6.084	7.775
	1.0	2.412	2.686	4.579	5.514	6.767
	2.0	2.276	2.497	3.724	4.249	4.725
40	0.0	3.333	3.773	6.693	8.727	11.471
	0.5	3.308	3.752	6.718	8.707	11.287
	1.0	3.231	3.656	6.274	7.678	9.058
	1.5	3.120	3.487	5.585	6.456	7.418
	2.0	2.981	3.289	4.850	5.507	6.133

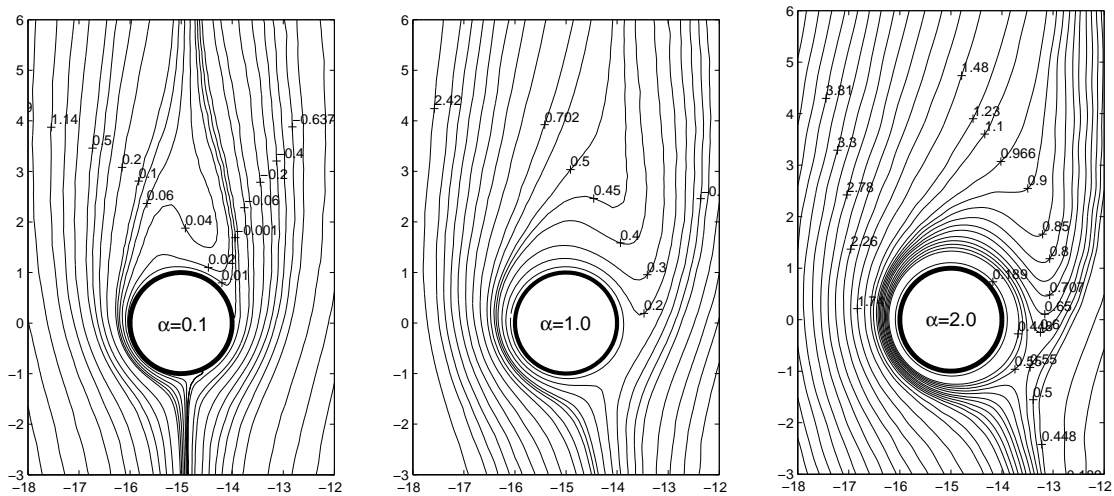


Figure 5.4 Streamline patterns at $Re = 20$, $g = 14$, $\alpha = 0.1, 1.0$, and 2.0 , and for $Pr = 1$.

5.3 Small gap spacing ($g \lesssim 3$) and non zero rate of rotation

The key quantities that influence the thermal interaction between two rotating circular cylinder in a uniform stream are the Reynolds number, the Prandtl number, the gap between cylinders, and the rate of rotation. As we mentioned previously (section 5.1) for $g > 5$ the temperature field around each of the two cylinders is similar to the temperature field around a single cylinder. To be more accurate, in Figure 5.7 we present the dependence of the local Nusselt number distribution for case of $Re = 20$, $\alpha = 1$, and $Pr = 1, 5, 10$, and 20 . The difference between local Nusselt number distributions on the gap spacing for the cases with $g > 3$ is not larger than 5% for all considered Pr number. It seems to be interesting that the minimum value of the local Nusselt number for fixed Prandtl number, $Pr \in [1, 10]$, and for $g > 1.5$ does not depend on the gap spacing. The location of this minimum shifts in clockwise direction (direction of rotation of the left cylinder) when Pr increases. For instance, for $Pr = 1$, the minimum occurs at $\theta \approx 240^\circ$, for $Pr = 5$ the minimum occurs at $\theta \approx 270^\circ$, for $Pr = 10$ the minimum

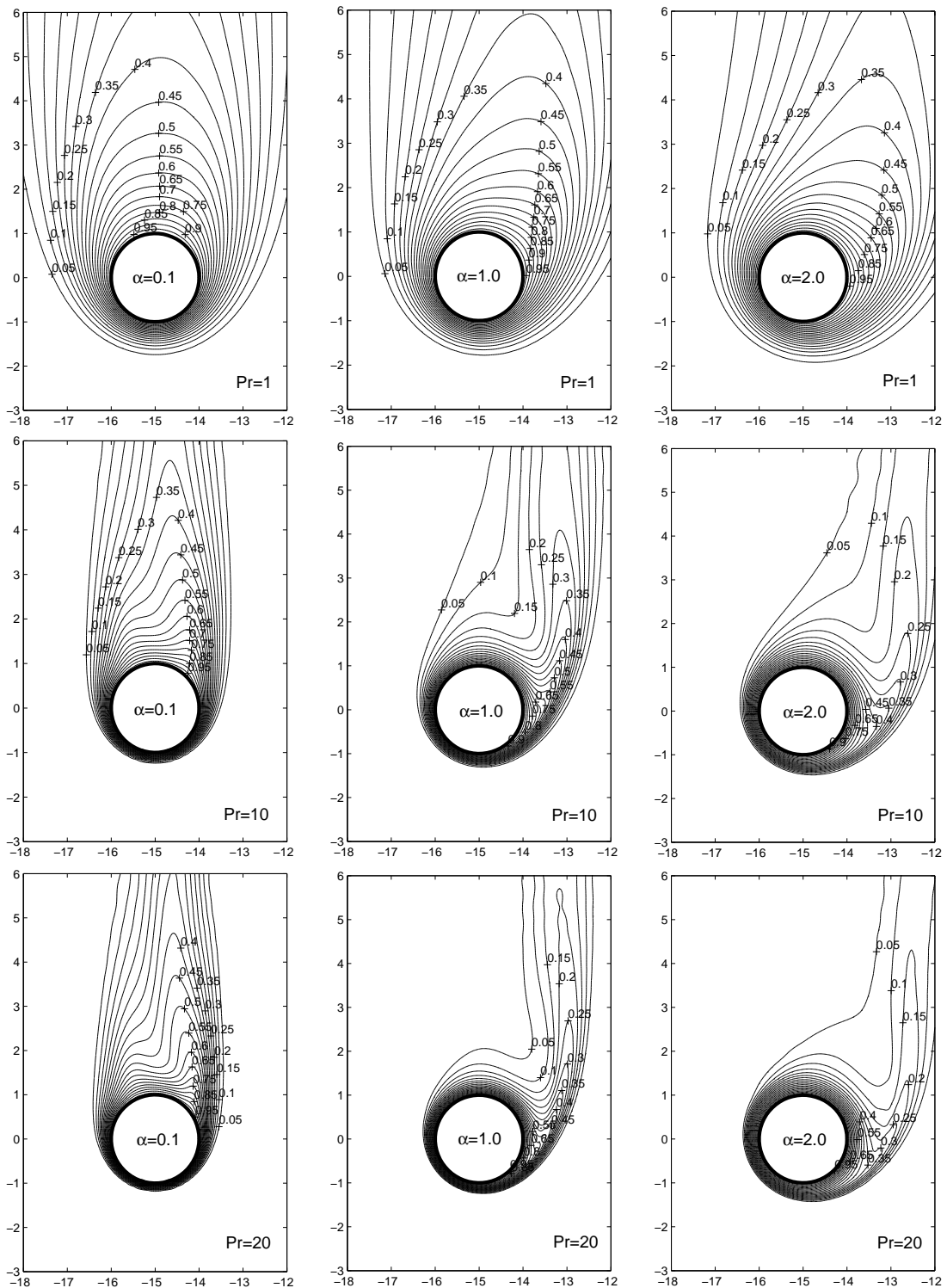


Figure 5.5 Temperature contours over two circular cylinders at $Re = 20$, $g = 14$, $\alpha = 0.1, 1.0, 2.0$, and for $Pr = 1, 10$, and 20 .

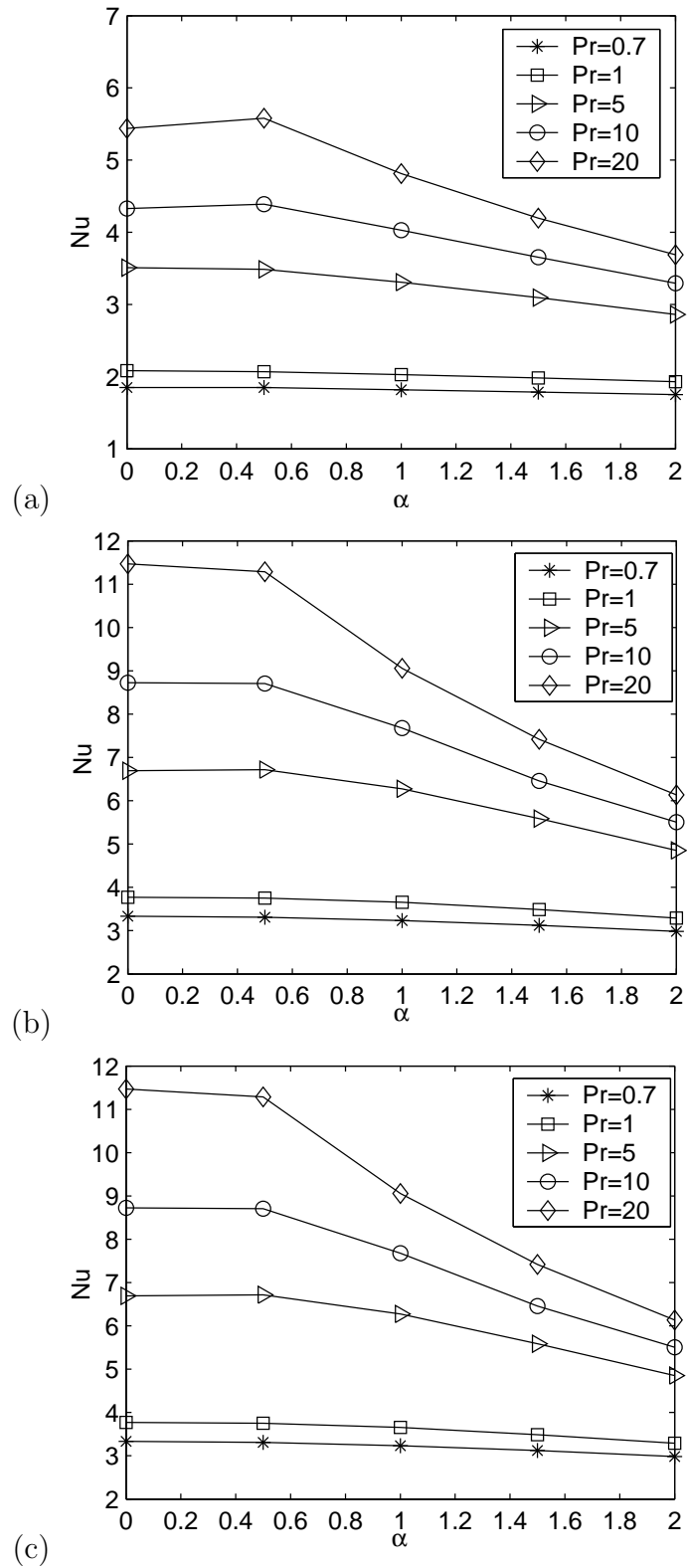


Figure 5.6 Nusselt number at (a) $Re = 10$, (b) $Re = 20$, and (c) $Re = 40$, and $g = 14$ for different Prandtl number Pr .

occurs at $\theta \approx 300^\circ$.

Figure 5.8 shows streamline patterns and isotherm contours for fixed Reynolds number $Re = 20$, $Pr = 1$, and $\alpha = 1$ for different gap spacing $g = 1, 2, 3, 4$, and 5 . The pattern of streamlines and isotherms around each cylinder is similar to the corresponding patterns around a single rotating cylinder in the case $g > 3$ (compare rows 3, 4, and 5 on Figure 5.8). For small gap spacing $g = 1$ (first row in Figure 5.8) streamlines edge two cylinders and main stream flows around fluid bubble. Within this fluid bubble there are two regions of fluid which rotate together with cylinders. The isotherms follow the streamline patterns. For large gap spacing, $g \gtrsim 3$ (see two last rows in Figure 5.8), there are two separate wake-shape regions of isotherms behind each cylinder. These regions are similar to the temperature field in the flow around a single rotating circular cylinder. For small gap spacing, the interaction between the cylinders in uniform flow become essential. There is a saddle critical point in the temperature field, which is located between the cylinders (see first row in Figure 5.8). Therefore, the results for $g < 3$ are addressed in this section.

The variation of the local Nusselt number on the surface of the left cylinder at fixed Reynolds number and rate of rotation, $Re = 20$, $\alpha = 1$, for the range of Prandtl number $0.7 \leq Pr \leq 20$ is shown in Figure 5.9. The maximum and minimum values of the local Nusselt number in all cases are represented in Figure 5.9. In the cases of moderate to low convection rate, $Pr = 0.7, 1$, and 5 , the increase in Pr increases the local heat transfer rate at all points of cylinder surface. For larger Pr and $g \gtrsim 2$ there is light decrease of $Nu(\theta)$ when Pr increases from 5 to 20 . This behavior is observed in the interval $300^\circ < \theta < 360^\circ$ in Figure 5.9.

The effect of the rotation rate and Prandtl number on the average Nusselt number is investigated for fixed gap spacing $g = 2$ and for several Reynolds number

as shown in Table 5.3 and Figure 5.10. In case of zero rotation, the increase of Prandtl number from 0.7 to 20 results in a considerable increases of the average Nusselt number, \overline{Nu} , that is almost three times. However in the non zero rotation cases, the Prandtl number has a smaller effect on \overline{Nu} since the rotating fluid layer adjacent to the cylinder surfaces acts as a buffer isolating the cylinder from the main stream and causing a decrease in the overall heat transfer rate. For instance, in the case of $Re = 10$ at $\alpha = 2$, the increase of Pr from 0.7 to 20 results in increase of \overline{Nu} only 2.0 times, compared with $\alpha = 0$, where \overline{Nu} increases by more than 3 times.

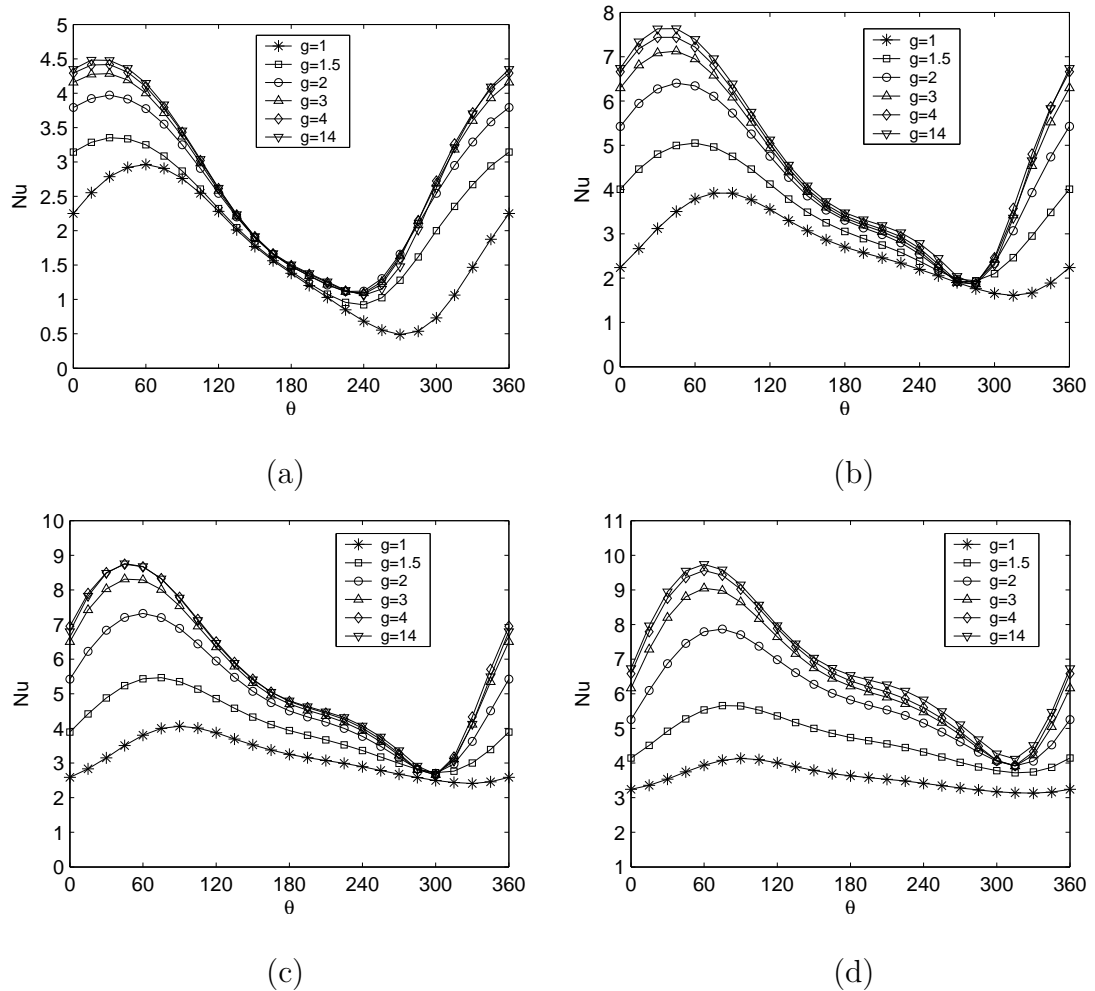


Figure 5.7 Local Nusselt number at $Re = 20$, $\alpha = 1$, and (a) $Pr = 1$, (b) $Pr = 5$, (c) $Pr = 10$, and (d) $Pr = 20$.

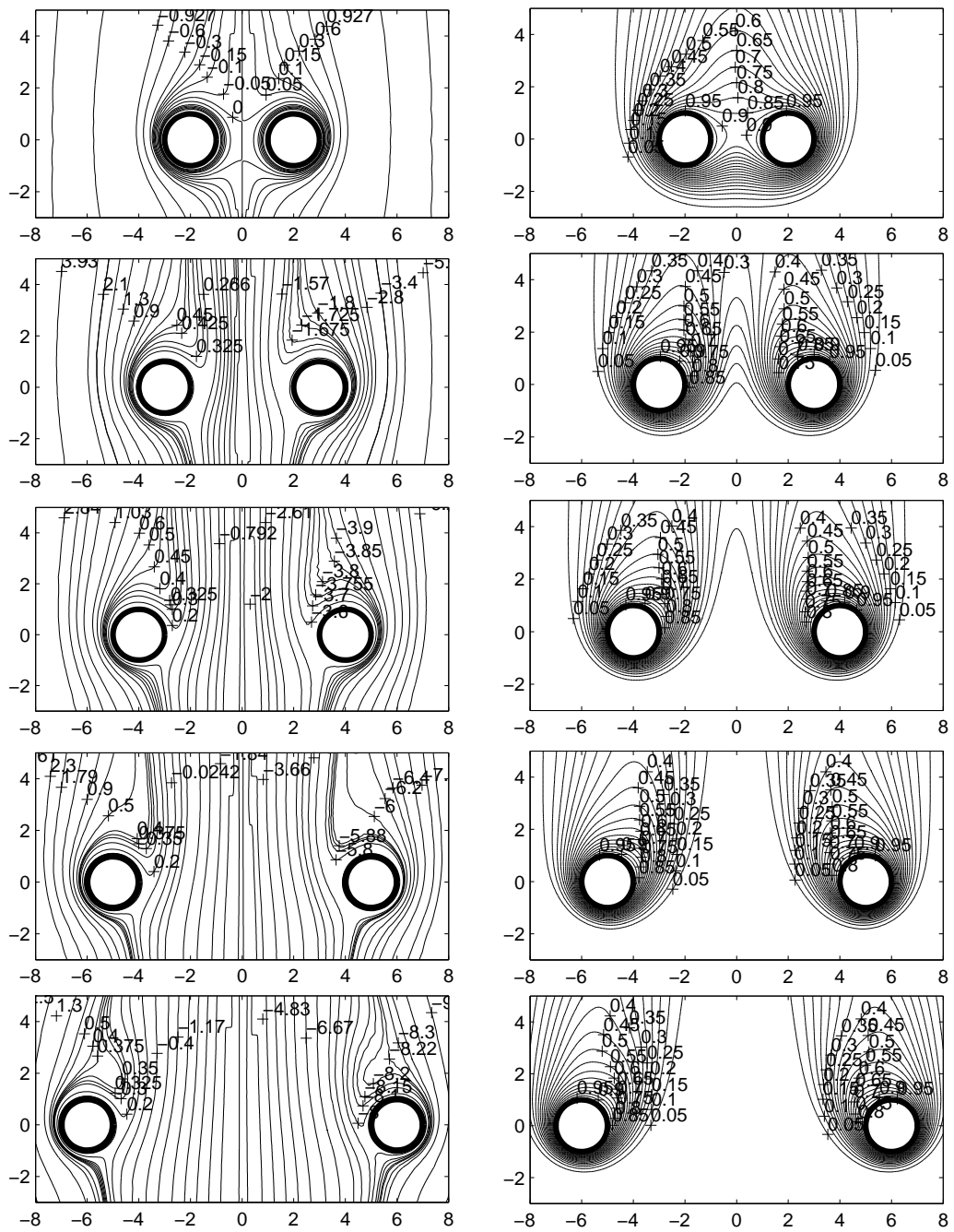


Figure 5.8 Streamline patterns (left column) and temperature contours (right column) of flow over two circular cylinders at $Re = 20$, $\alpha = 1$, and $g = 1$ - first row, $g = 2$ - second row, $g = 3$ - third row, $g = 4$ - fourth row, and $g = 5$ - fifth row.

Table 5.3 Variation of average Nusselt number at $g = 2$.

Re	α	Pr				
		0.7	1	5	10	20
10	0.0	1.630	1.866	3.147	3.936	4.934
	0.5	1.519	1.750	2.867	3.493	4.254
	1.0	1.353	1.556	2.482	2.937	3.458
	1.5	1.189	1.328	2.130	2.497	2.787
	2.0	1.121	1.248	1.872	2.101	2.273
20	0.0	2.223	2.503	4.223	5.299	6.658
	0.5	2.115	2.370	3.875	4.819	5.957
	1.0	1.989	2.211	3.402	4.095	4.889
	1.5	1.789	1.994	2.971	3.430	3.859
	2.0	1.596	1.786	2.677	2.962	3.195
40	0.0	2.973	3.351	5.752	7.300	9.292
	0.5	2.802	3.139	5.328	6.740	8.362
	1.0	2.589	2.865	4.558	5.546	6.509
	1.5	2.390	2.610	3.921	4.547	5.050
	2.0	2.261	2.474	3.485	3.858	4.190

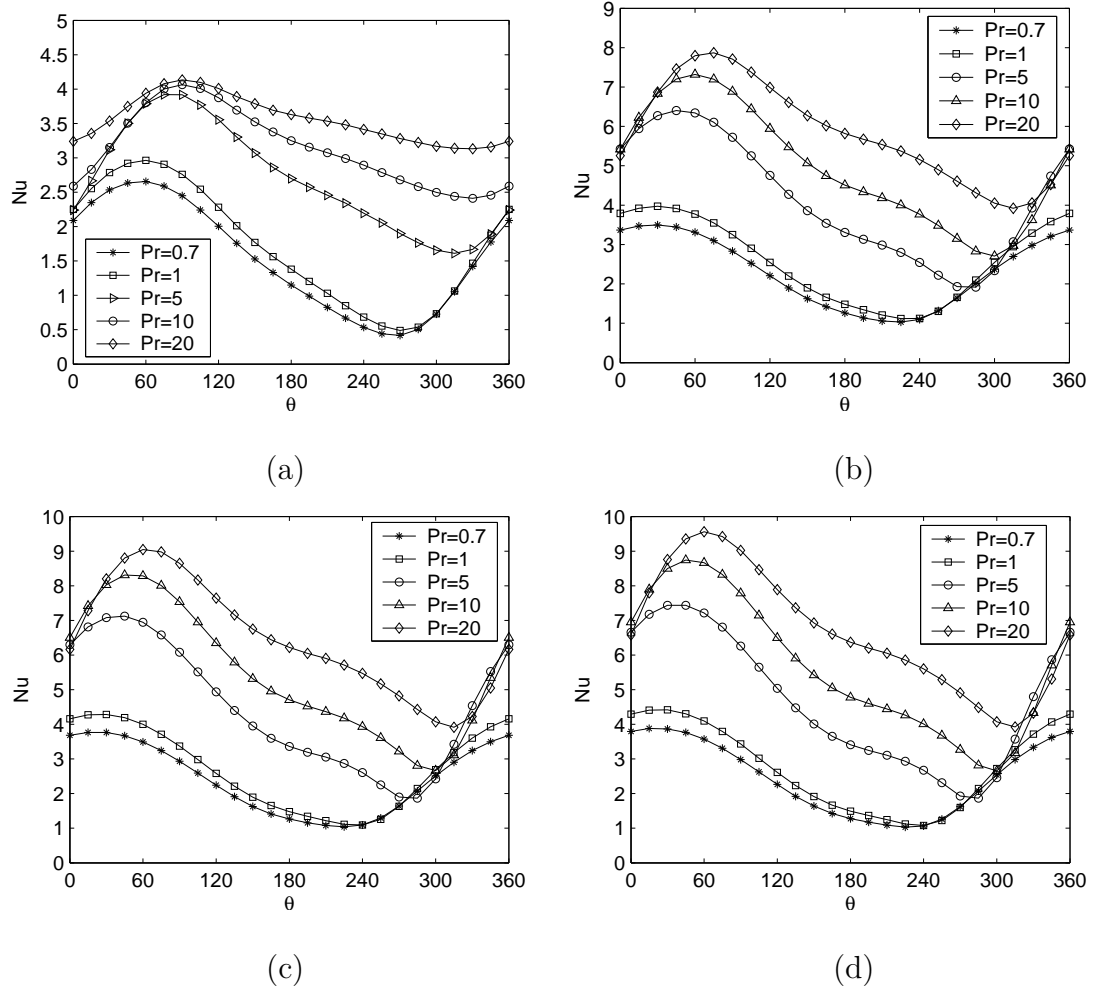


Figure 5.9 Local Nusselt number at $Re = 20$, $\alpha = 1$, and (a) $g = 1$, (b) $g = 2$, (c) $g = 3$, and (d) $g = 4$.

The variation of the local Nusselt number on the surface of the cylinders at $Re = 10, 20$, and 40 , $Pr = 1$ and $g = 1$ for a range of rotational rate $0 < \alpha < 2.5$ is shown in Figure 5.11. The variation of local Nusselt number with rotation rate is not as straightforward as in the case of large gap spacing. One of the interesting features is that as α increases, the value of $Nu(0)$ ($\theta = 0^\circ$) decreases to not more than minimal value. For example, in case of $Re = 10$, this value is $Nu(0) \approx 0.75$, for $Re = 20$ this is $Nu(0) \approx 1.0$, and for $Re = 40$ this is $Nu(0) \approx 2.0$. The points of maximum and minimum local Nusselt numbers shift in the direction of cylinder rotation. The maximum value of $Nu(\theta)$ decreases as α increases. The minimum

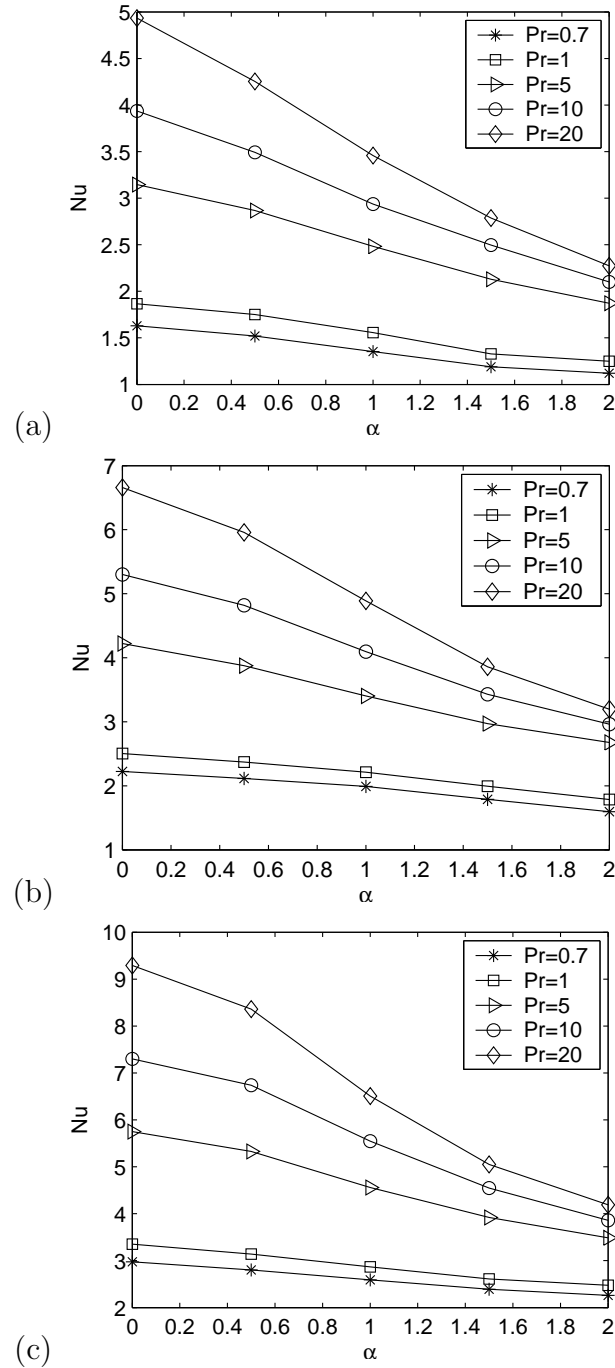


Figure 5.10 Nusselt number at (a) $Re = 10$, (b) $Re = 20$, and (c) $Re = 40$, and $g = 2$ for different Prandtl number Pr .

value of $Nu(\theta)$ decreases as α increases, up to the rate of rotation when the two fluid layers adjacent to the cylinder surfaces merge.

The details of the steady flow and thermal fields are presented in Figures 5.12-5.14 in the form of streamlines and constant temperature contours. At $Re = 10$ and $\alpha = 0.5$, the streamlines edge the two cylinders (see Figure 5.12, left column). As can be seen from Figures 5.13 the temperature gradient is low along the line between the cylinder centers (very rare clustering isotherms). This is the reason of minimum value of $Nu(\theta)$ at $\theta \approx 270^\circ$. At $Re = 20$, similar behavior of streamline patterns and temperature field corresponds to the rotation rate $\alpha \approx 1.0$. However, at $Re = 20$ and $\alpha = 0.5$, fluid from the main stream flows through the gap spacing between the cylinders. Let us denote by α^* the rate of rotation when the two layers of fluid adjacent to the cylinder surfaces merge with each other for the first time. If the rate of rotation is $\alpha > \alpha^*$ then the minimum value of the local Nusselt number increases as α increases. The location of the minimum value correlates with the location of the saddle critical point in the temperature field. For instance, for $Re = 10$, $\alpha = 1$ this minimum is located near $\theta = 300^\circ$ and the line between cylinder center and saddle critical point corresponds to the same direction $\theta = 300^\circ$ (see second row in Figure 5.13). As the Prandtl number increases, the clustering of the temperature isotherms near the cylinder surfaces increases, which indicates increasing temperature gradient (and thus higher local Nusselt number). This can be seen in Figures 5.13 and 5.14 (compare first, second, and third columns). Comparison of the isotherms in Figures 5.13 and 5.14 shows that an increase in the Prandtl and/or Reynolds number makes the wake-shape region of the temperature field more narrow. It is interesting to point out that the rate of rotation does not significantly affect the size of the wake shape region. For instance, in Figure 5.13 for case $Pr = 10$, $\alpha = 1.0, 1.5,$ and 2.0 , the width

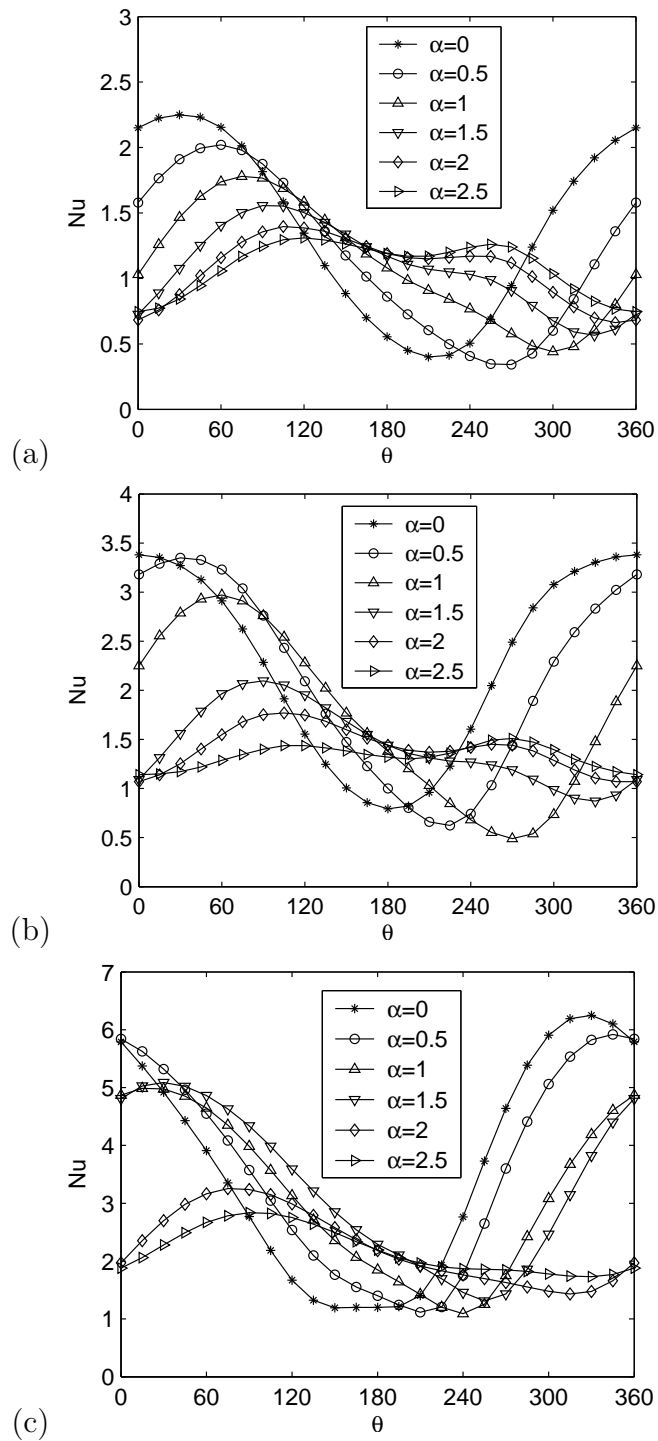


Figure 5.11 Local Nusselt number variation on the surface of the circular cylinders at $Pr = 1$, $g = 1$, $\alpha = 0, 0.5, 1, 1.5, 2$, and 2.5 for (a) $Re = 10$, (b) $Re = 20$, and (c) $Re = 40$.

(in x -direction) of the wake-shape region at $y = 5$ is approximately 6 and in case $Pr = 20$, $\alpha = 1.0$, 1.5, and 2.0 the width of the wake-shape region is approximately 4. A similar effect can be seen in Figure 5.14 for $Re = 20$. If we compare the size of wake-shape region of the temperature field in the cases $Re = 10$, $Pr = 10$, $\alpha = 1.5$ and $Re = 10$, $Pr = 10$, $\alpha = 2.0$ (see second column of Figure 5.13), we can observe that the size of the wake-shape region at $y = 5$ does not change significantly.

Another interesting observation concerns the saddle critical point in the temperature field. When $\alpha = \alpha^*$ this critical point lies in the line connecting the cylinder centers. When $\alpha > \alpha^*$ this saddle critical point is pushed down (negative direction of y -axis) by the fluid layers which rotate together with the cylinders. Recall here that the left cylinder rotates in the clockwise direction and the right one in the counterclockwise direction. Another aspect that appear to be important is the similarity of the isotherm patterns in the cases $Re = 10$, $\alpha = 1.5$, $Pr = 20$, and $Re = 10$, $\alpha = 2.0$, $Pr = 20$ (or in the cases of $Re = 20$, $\alpha = 1.5$, $Pr = 20$, and $Re = 20$, $\alpha = 2.0$, $Pr = 20$). This is easily explained by comparison of the streamline patterns for the same cases. The patterns of isotherm are very similar to the pattern of streamlines. Finally, it is appropriate to analyse the variation of the average Nusselt number with the variation of other parameters such as α , Re , and Pr . The results for the surface average Nusselt number are shown in Table 5.4 in tabular form and in Figure 5.15 in graphic form. An increase of the Prandtl number results in a considerable increase of the average Nusselt number, \overline{Nu} , for small rotation rate $\alpha \lesssim 1$. For larger values of α , $\alpha > 1$, \overline{Nu} still increases but by a smaller amount. An increase of rotation rate α results in a decrease of the average Nusselt number \overline{Nu} . This behavior is related with the rotating fluid layers adjacent to the cylinder surfaces. Such layers act as a buffer isolating cylinders

from the main stream, and causing a decrease in the overall heat transfer rate.

The heat transfer through these layers is mostly due to conduction.

Table 5.4 Variation of average Nusselt number at $g = 1$.

Re	α	Pr				
		0.7	1	5	10	20
10	0.0	1.051	1.258	2.765	3.545	4.455
	0.5	0.873	0.967	1.519	1.902	2.359
	1.0	0.848	0.947	1.589	1.857	2.078
	1.5	0.879	1.003	1.575	1.761	1.933
	2.0	0.926	1.057	1.541	1.706	1.861
20	0.0	1.886	2.247	4.064	5.105	6.418
	0.5	1.602	1.909	3.454	4.087	4.944
	1.0	1.258	1.413	2.433	2.990	3.469
	1.5	1.181	1.336	2.021	2.241	2.423
	2.0	1.238	1.387	1.902	2.075	2.224
40	0.0	3.345	3.781	6.527	8.253	10.407
	0.5	3.124	3.514	5.964	7.440	9.199
	1.0	2.510	2.815	4.489	5.452	6.553
	1.5	2.554	2.833	4.563	5.448	6.298
	2.0	1.830	2.044	3.100	3.403	3.646

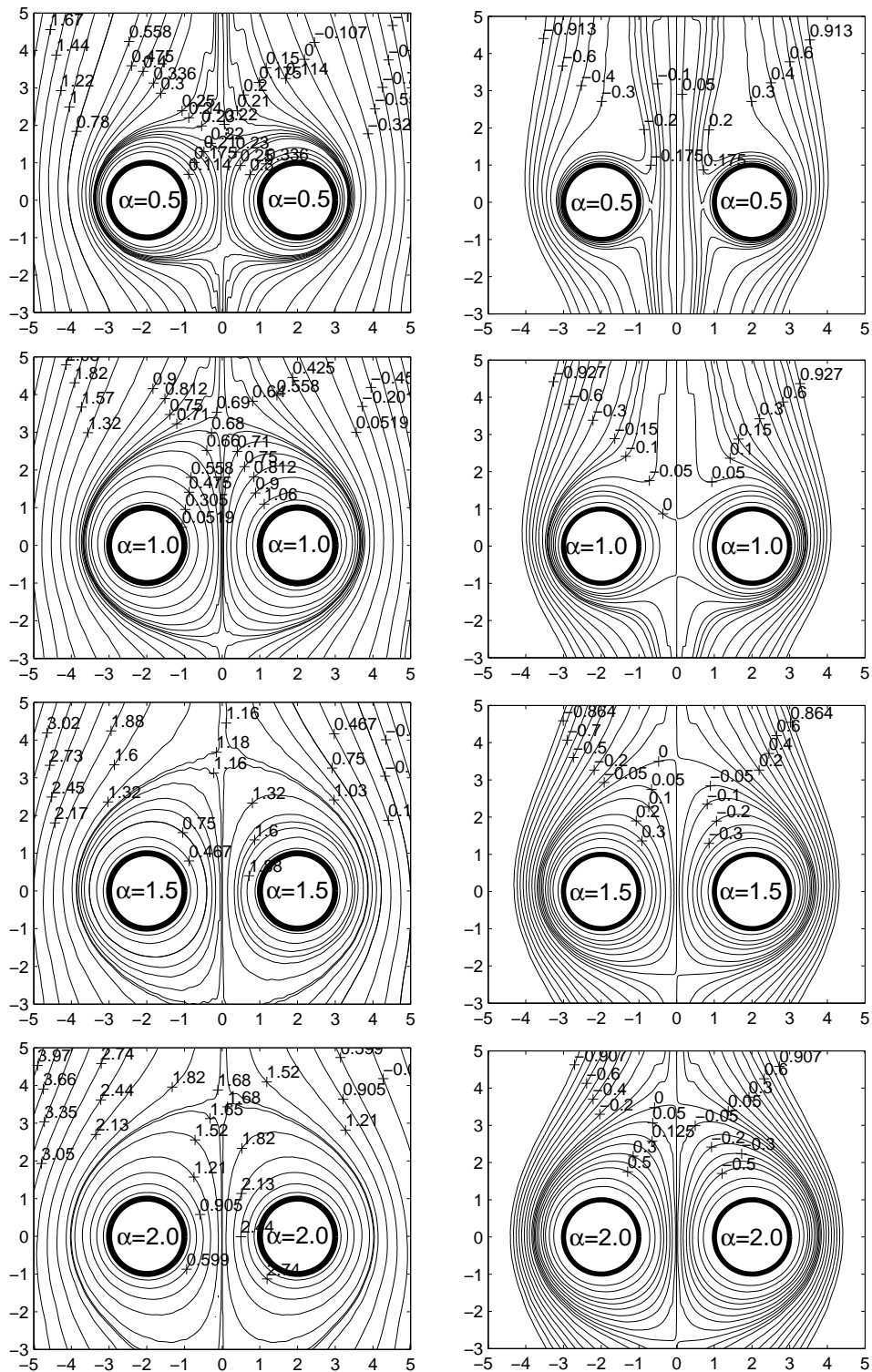


Figure 5.12 Streamlines contours over two circular cylinders at $Re = 10$ (left column), and $Re = 20$ (right column), $Pr = 1$, $g = 1$, and $\alpha = 0.5, 1.0, 1.5$, and 2.0 .

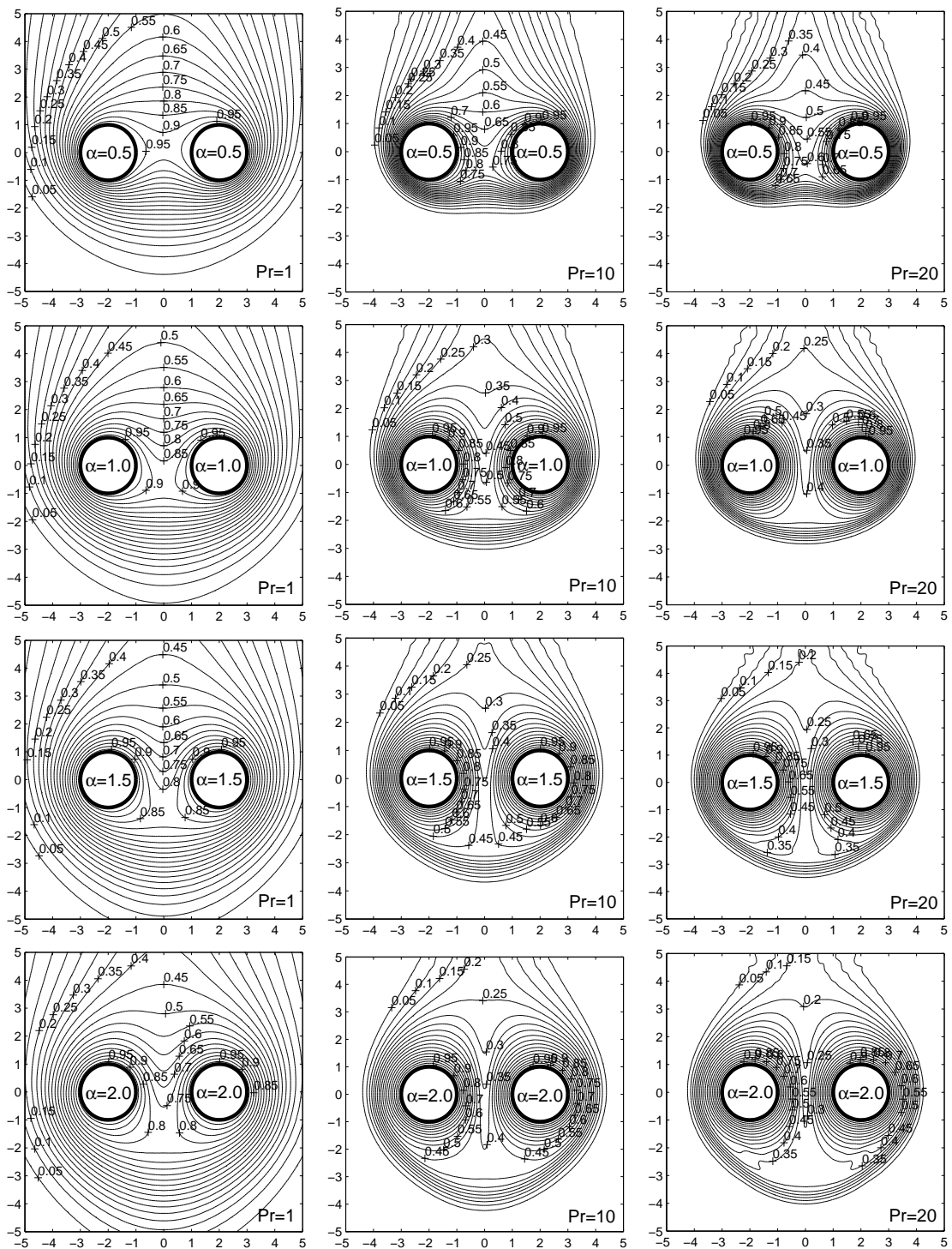


Figure 5.13 Temperature contours over two circular cylinders at $Re = 10$, $g = 1$, $Pr = 1, 10, 20$, and $\alpha = 0.5, 1.0, 1.5$, and 2.0 .

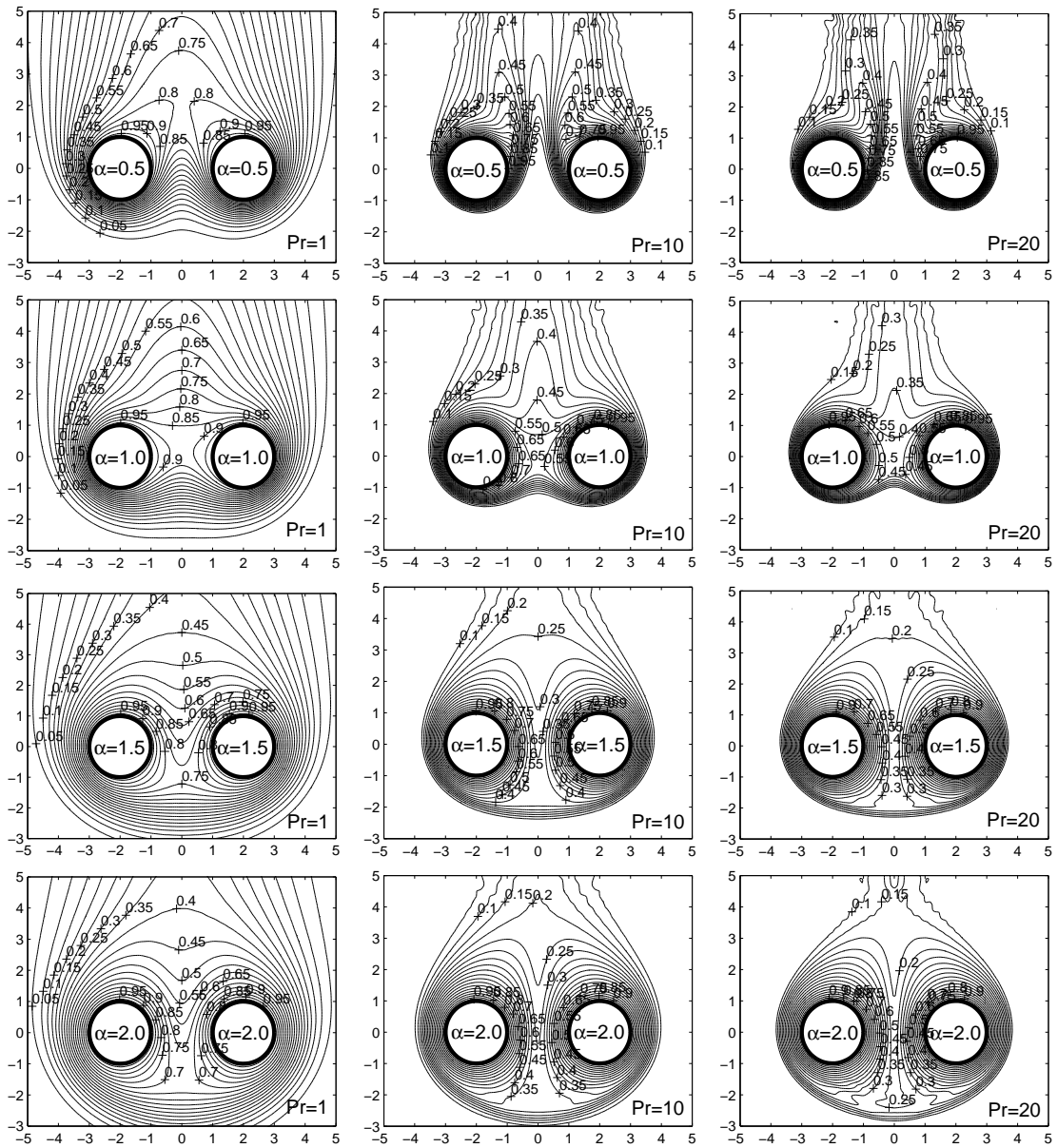


Figure 5.14 Temperature contours over two circular cylinders at $Re = 20$, $g = 1$, $Pr = 1, 10, 20$, and $\alpha = 0.5, 1.0, 1.5$, and 2.0 .

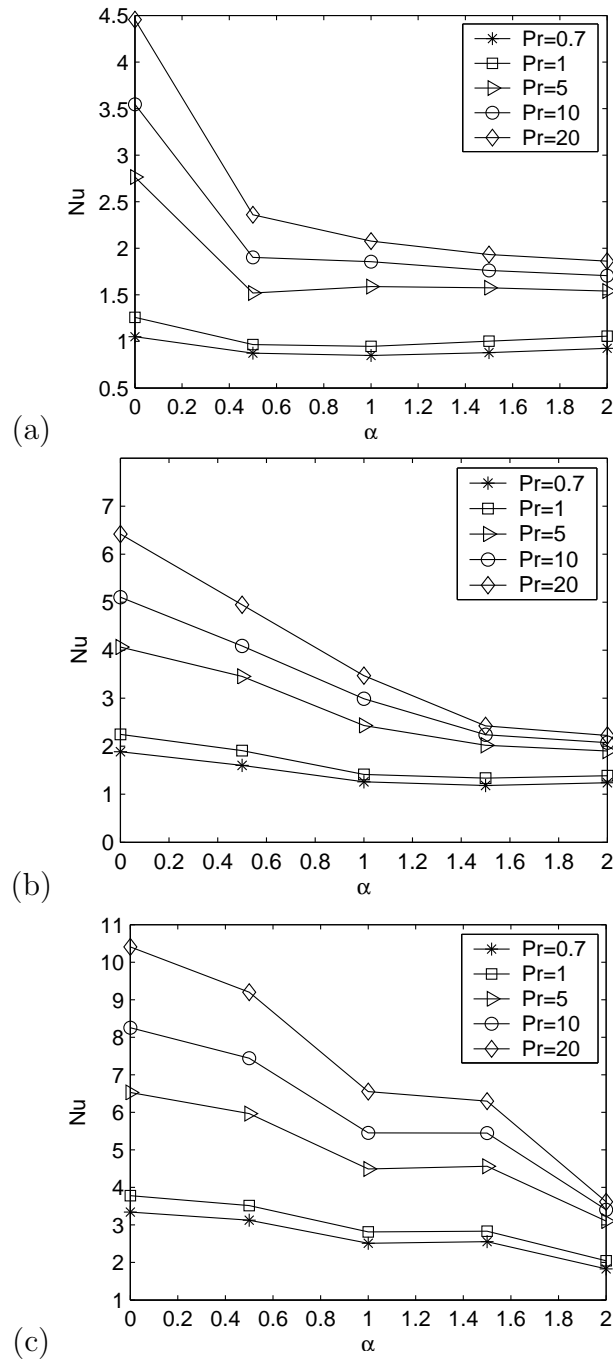


Figure 5.15 Nusselt number at (a) $Re = 10$, (b) $Re = 20$, and (c) $Re = 40$, and $g = 1$ for different Prandtl number Pr .

CHAPTER VI

CONCLUSIONS

The present study has numerically investigated the characteristics of two-dimensional heat transfer in laminar flow past two rotating circular cylinder in a side-by-side arrangement at various ranges of absolute rotation speed ($|\alpha| \leq 2.5$), Reynolds number ($10 \leq Re \leq 40$), Prandtl number ($0.7 \leq Pr \leq 20$), and for gap spacings ($1 \leq g \leq 14$).

We summarize the numerical results obtained in this work as follows:

- ▶ Numerical algorithms and computer codes have been developed and validated.
- ▶ For large gap spacing ($g = 14$), an increase in rotational speed leads to a displacement of the maximum and minimum values of the local Nusselt number ($Nu(\theta)$) in the direction of rotation. The maximum value of $Nu(\theta)$ decreases with increased speed of rotation and the minimum value of $Nu(\theta)$ slightly increases with increasing rotation.
- ▶ For small gap spacing ($g = 1$), the maximum value of $Nu(\theta)$ shifts in the direction of the cylinders rotation and decreases when the speed of rotation increases. For $\alpha = 2.5$ the distribution of $Nu(\theta)$ becomes almost uniform.
- ▶ The average Nusselt number for each individual cylinder increases with increasing gap spacing and tends to the average Nusselt number for a single cylinder.
- ▶ For large gap spacing (case of single cylinder) the average Nusselt number decreases with increasing speed of rotation. For $Pr = 20$ average Nusselt number

drops down by almost 50% when α increases from 0 to 2.

► In case of small gap spacing, $g = 1$, the main drop of the average Nusselt number occurs as α increases from 0 up to 1.

► An increase in the Reynolds number, Prandtl number and rotational rate α increases the asymmetry and complexity of the temperature contours. The increase in the Prandtl and/or Reynolds numbers increases the compactness of isotherms toward the downstream direction. This behavior can be explained by the increasing the role of convection in the mechanism of heat transfer with increasing Re and/or Pr number.

Based on this numerical study, the following recommendations for future research can be made. We should be able to study the flow past two cylinders of different radii which rotate at different angular velocities. It is possible to study the case in which the cylinders are in tandem arrangement. Future work should include simulations in the cases of higher Reynolds number, $Re > 45$.

REFERENCES

REFERENCES

- Antontsev, S.N., Kazhikhov, A.V., and Monakhov, V.N. (1990). **Boundary Value Problems in Mechanics of Nonhomogeneous Fluids**. New York: Elsevier Science Publishing Company Inc.
- Badr, H.M., Dennis, S.C.R., and Young, P.J.S. (1989). Steady flow past a rotating circular cylinder at low Reynolds numbers. **Comput. Fluids** 17:579-609.
- Batchelor, G.K. (2000). **Introduction to Fluid Dynamics**. Cambridge: Cambridge University Press.
- Bearman, P.W., and Wadcock, A. J. (1973). The interaction between a pair of circular cylinders normal to a stream. **J. Fluid Mech.** 61:499-511.
- Bharti, R.P., Chhabra, R.P., and Eswaran, V. (2007). A numerical study of the steady forced convection heat transfer from an unconfined circular cylinder. **Heat Mass Transfer** 43:639-648.
- Chang, K., and Song, C. (1990). Interactive vortex shedding from a pair of circular cylinders in a transverse arrangement. **Int. J. Numerical Methods in Fluids** 11:317329.
- Chorin, A.J. (1968). Numerical solution of the Navier-Stokes equations. **Math. Comp.** 22:745-762.
- Chorin, A.J. (1969). On the convergence of discrete approximations to the Navier-Stokes equations. **Math. Comp.** 23:341-353.

- Chung, M-H. (2006). Cartesian cut cell approach for simulating incompressible flows with rigid bodies of arbitrary shape. **Computer & Fluids** 35:607-623.
- Fang, L.C., Nicolaou, D., and Cleaver, J.W. (1999). Transient removal of a contaminated fluid from a cavity. **Int. J. Heat Fluid Flow** 20:605-613.
- Fornberg, B. (1980). A numerical study of steady viscous flow past a circular cylinder. **J. Fluid Mech.** 98(4):819-855.
- Gshwendtner, M.A. (2004). Optical investigation of the heat transfer from a rotating cylinder in a cross flow. **Heat and Mass Transfer** 40:561-572.
- Ingham, D.B., and Tang, T. (1990). A numerical investigation into the steady flow past a rotating circular cylinder at low and intermediate Reynolds number. **J. Comput. Phys.** 87:91-107.
- Joucaviel, M., Gosselin, L., and Bello-Ochende, T. (2008). Maximum heat transfer density with rotating cylinders aligned in cross-flow. **Int. Comm. Heat Mass Transfer** 35:557-564.
- Juncu, G. (2006). Unsteady forced convection heat/mass transfer around two spheres in tandem at low Reynolds numbers. **Int. J. Thermal Sciences** 46:1011-1022.
- Juncu, G. (2007a). A numerical study of momentum and forced convection heat transfer around two tandem circular cylinders at low Reynolds numbers. Part I: Momentum transfer. **Int. J. Heat Mass Transfer** 50:3788-3798.
- Juncu, G. (2007b). A numerical study of momentum and forced convection heat transfer around two tandem circular cylinders at low Reynolds numbers.

- Part II: Forced convection heat transfer. **Int. J. Heat Mass Transfer** 50:3799-3808.
- Kang, S., Choi, H., and Lee S. (1999). Laminar flow past a rotating circular cylinder. **Physics of Fluids** 11(11):3312-3321.
- Kang, S. (2003). Characteristics of flow over two circular cylinder in a side-by-side arrangement at low Reynolds numbers. **Physics of Fluids** 15(9):2486-2498.
- Lange, C.F., Durst, F., and Breuer M. (1998). Momentum and heat transfer from cylinders in laminar crossflow at $10^{-4} \leq Re \leq 200$. **Int. J. Heat Mass Tran.** 41:3409-3430.
- Mahfouz, F.M., and Badr, H.M. (1999a). Heat convection from a cylinder performing steady rotation or rotary oscillation - Part I: Steady rotation. **Heat and Mass Transfer** 34:365-373.
- Mahfouz, F.M., and Badr, H.M. (1999a). Heat convection from a cylinder performing steady rotation or rotary oscillation - Part II: Rotary oscillation. **Heat and Mass Transfer** 34:375-380.
- Mandhani, V.K., Chhabra, R.P., and Eswaran, V. (2002). Forced convection heat transfer in tube banks in cross flow. **Chemical Engineering Science** 57:379-391.
- Meneghini, J.R., Saltara, F., Siqueira, C.L.R., and Ferrari Jr. J.A. (2001). Numerical simulation of flow interference between two circular cylinders in tandem and side-by-side arrangements. **Journal of Fluid and Structures** 15:327-350.

- Meng-Hsuan, C. (2006). Cartesian cut cell approach for simulating incompressible flows with rigid bodies of arbitrary shape. **Computers & Fluids** 35:607-623.
- Mittal, S., Kumar, V., and Raghuvanshi A. (1997). Unsteady incompressible flows past two cylinders in tandem and staggered arrangements. **Int. J. Numerical Methods in Fluids** 25:1315-1344.
- Mittal, S., and Kumar, B. (2003). Flow past a rotating cylinder. **J. Fluid Mech.** 476:303-334.
- Morgan, V.T. (1975). The overall convective heat transfer from smooth circular cylinders. **Adv. Heat Transfer** 11:199-264.
- Moshkin, N., and Yambangwi, D. (2009). Steady viscous incompressible flow driven by a pressure difference in a planar T-junction channel. **International Journal of Computational Fluid Dynamics** 23(3):259-270.
- Patil, R.C., Bharti, R.P., and Chhabra R.P. (2008). Steady flow of power law fluids over a pair of cylinders in tandem arrangement. **Ind. Eng. Chem. Res.** 47:1660-1683.
- Samarskii, A.A., and Nikolaev, E.S. (1989). **Numerical Methods for Grid Equations**. Basel: Birkhäuser Verlag.
- Soares, A.A., and Ferreira, J.M. (2005). Flow and forced convection heat transfer in crossflow of non-newtonian fluid over a circular cylinder. **Ind. Eng. Chem. Res.** 44(15):5815-5827.
- Stålberg, E., Brüger, A., Lötstedt, P., Johansson, A.V., and Henningson, D.S. (2006). High order accurate solution of flow past a circular cylinder. **J. Sci. Comp.** 27:431-441.

- Stojković, D., Breuer, M., and Durst, F. (2002). Effect of high rotation rates on the laminar flow around a circular cylinder. **Physics of Fluids** 14(9):3160-3178.
- Sungnul, S. (2006). **Numerical simulation of fluid flow past self-propelled body**. Ph.D. Dissertation, Suranaree University of Technology, Thailand.
- Sungnul, S., and Nikolay M. (2006). Numerical simulation of steady viscous flow past two rotating circular cylinders. **Suranaree J. Sci. Technol.** 13(3):219-233.
- Temam, R. (1969). Sur l'approximation de la solution des equations de Navier-Stokes par la méthode des pas fractionnaires II. **Arch. Rational Mech. Anal** 33:377-385.
- Temam, R. (1977). **Navier-Stokes equations. Theory and numerical analysis. Studies in Mathematics and its Applications**. North-Holland: Amsterdam.
- Williamson, C.H.K. (1985). Evolution of a single wake behind a pair of bluff bodies. **J. Fluid Mech.** 159:1-18.
- Yanenko, N.N. (1971). **The method of Fractional Steps: The Solution of Problems of Mathematical Physics in Several Variables**. Translated by M. Holt. New York: Springer-Verlag.
- Yoon, H.S., Kim, J.H., Chun, H.H., and Choi, H.J. (2007). Laminar flow past two rotating circular cylinders in a side-by-side arrangement. **Physics of Fluids** 19(12):128103:1-4
- Yoon, H.S., Chun, H.H., Kim, J.H., and Park, I.L.R. (2009). Flow characteristics

of two rotating side-by-side circular cylinder. **Computers & Fluids** 38:466-474.

Zdravkovich, M.M. (1985). Forces on a circular cylinder near a plane wall. **Applied Ocean Research** 7:197-201.

Zdravkovich, M.M. (1997). **Flow around circular cylinders: Fundamentals**. Oxford, U.K.: Oxford University Press.

Zdravkovich, M.M. (2003). **Flow around circular cylinders: Applications**. Oxford, U.K.: Oxford University Press.

APPENDICES

APPENDIX A

THE ELIMINATION METHOD FOR THREE-POINT EQUATIONS

We will begin the study of the elimination method with the case of a scalar equation. Suppose we want to solve the following system of three-point equations

$$\begin{aligned}
 c_0 y_0 - b_0 y_1 &= f_0, & i = 0, \\
 -a_i y_{i-1} + c_i y_i - b_i y_{i+1} &= f_i, & 1 \leq i \leq N-1, \\
 -a_N y_{N-1} + c_N y_N &= f_N, & i = N,
 \end{aligned} \tag{A.1}$$

or, in vector form,

$$\mathcal{A}Y = F \tag{A.2}$$

where $Y = (y_0, y_1, \dots, y_N)^T$ is the vector of unknowns, $F = (f_0, f_1, \dots, f_N)^T$ is the right hand side vector, and \mathcal{A} is the square $(N+1) \times (N+1)$ matrix with real or complex coefficients.

$$\mathbf{A} = \begin{pmatrix}
 c_0 & -b_0 & 0 & 0 & \cdots & 0 & 0 & 0 & 0 \\
 -a_1 & c_1 & -b_1 & 0 & \cdots & 0 & 0 & 0 & 0 \\
 0 & -a_2 & c_2 & -b_2 & \cdots & 0 & 0 & 0 & 0 \\
 \cdot & \cdot & \cdot & \cdot & \cdots & \cdot & \cdot & \cdot & \cdot \\
 0 & 0 & 0 & 0 & \cdots & -a_{N-2} & c_{N-2} & -b_{N-2} & 0 \\
 0 & 0 & 0 & 0 & \cdots & 0 & -a_{N-1} & c_{N-1} & -b_{N-1} \\
 0 & 0 & 0 & 0 & \cdots & 0 & 0 & -a_N & c_N
 \end{pmatrix}$$

Systems of the form (A.1) arise from a three-point approximation to a boundary-value problem for second-order ordinary differential equations with con-

stant and variable coefficients, and also when realizing difference schemes for equations with partial derivatives.

Following the idea of Gauss' method, we carry out the elimination of the unknown in (A.1). We introduce the notation $\alpha_1 = b_0/c_0, \beta_1 = f_0/c_0$ and write (A.1) in the following form

$$\begin{aligned} y_0 - \alpha_1 y_1 &= \beta_1, & i = 0, \\ -a_i y_{i-1} + c_i y_i - b_i y_{i+1} &= f_i, & 1 \leq i \leq N-1, \\ -a_N y_{N-1} + c_N y_N &= f_N, & i = N, \end{aligned} \quad (\text{A.3})$$

Take the first two equations of the system (A.3)

$$y_0 - \alpha_1 y_1 = \beta_1, \quad -a_1 y_0 + c_1 y_1 - b_1 y_2 = f_1.$$

Multiplying the first equation by a_1 and adding it to the second equation, we obtain $(c_1 - a_1 \alpha_1) y_1 - b_1 y_2 = f_1 + \alpha_1 \beta_1$ or, after dividing by $c_1 - a_1 \alpha_1$

$$y_1 - \alpha_2 y_2 = \beta_2, \quad \alpha_2 = \frac{b_1}{c_1 - \alpha_1 a_1}, \quad \beta_2 = \frac{f_1 + \alpha_1 \beta_1}{c_1 - \alpha_1 a_1}.$$

All the remaining equations of the system (A.3) do not contain y_0 , therefore this stage of the elimination process is completed. As a result we obtain a new "reduced" system

$$\begin{aligned} y_1 - \alpha_2 y_2 &= \beta_2, & i = 1, \\ -a_i y_{i-1} + c_i y_i - b_i y_{i+1} &= f_i, & 2 \leq i \leq N-1, \\ -a_N y_{N-1} + c_N y_N &= f_N, & i = N, \end{aligned} \quad (\text{A.4})$$

which does not contain the unknown y_0 and which has a structure analogous to (A.3). When this system has been solved, the unknown y_0 is found from the formula $y_0 = \alpha_1 y_1 + \beta_1$. We can apply the above described elimination procedure to the system (A.4). At the second stage, the unknown y_1 is eliminated, at the third y_2 , and so forth. At the end of the l^{th} stage we obtain a system for the

unknowns y_l, y_{l+1}, \dots, y_N

$$\begin{aligned} y_l - \alpha_{l+1}y_{l+1} &= \beta_{l+1}, & i = 1, \\ -a_i y_{i-1} + c_i y_i - b_i y_{i+1} &= f_i, & l+1 \leq i \leq N-1, \\ -a_N y_{N-1} + c_N y_N &= f_N, & i = N, \end{aligned} \quad (\text{A.5})$$

and formulas for finding y_i for $i \leq l-1$

$$y_i = \alpha_{i+1}y_{i+1} + \beta_{i+1}, \quad i = l-1, l-2, \dots, 0. \quad (\text{A.6})$$

The coefficients α_i and β_i , clearly, are found from the formulas

$$\alpha_{i+1} = \frac{b_i}{c_i - \alpha_i a_i}; \quad \beta_{i+1} = \frac{f_i + a_i \beta_i}{c_i - \alpha_i a_i}; \quad i = 1, 2, \dots; \quad \alpha_1 = \frac{b_0}{c_0}, \quad \beta_1 = \frac{f_0}{c_0}.$$

Substituting $l = N-1$ in (A.5), we obtain a system for y_N and y_{N-1}

$$y_{N-1} - \alpha_N y_N = \beta_N, \quad -a_N y_{N-1} + c_N y_N = f_N \quad (\text{A.7})$$

from which we find $y_N = \beta_{N+1}$, $y_{N-1} = \alpha_N y_N + \beta_N$.

Combining these equations with (A.6) ($l = N-1$), we obtain the final formulas for finding the unknowns

$$\begin{aligned} y_i &= \alpha_{i+1}y_{i+1} + \beta_{i+1}, & i = N-1, N-2, \dots, 0, \\ y_N &= \beta_N + 1, \end{aligned} \quad (\text{A.8})$$

where α_i and β_i are found from the recurrence formulas

$$\begin{aligned} \alpha_{i+1} &= \frac{b_i}{c_i - a_i \alpha_i}, & i = 1, 2, \dots, N-1, & \alpha_i = \frac{b_0}{c_0}, \\ \beta_{i+1} &= \frac{f_i + a_i \beta_i}{c_i - a_i \alpha_i}, & i = 1, 2, \dots, N, & \beta_i = \frac{f_0}{c_0} \end{aligned} \quad (\text{A.9})$$

Thus, the formulas (A.8)-(A.9) describe Gauss' method which, when applied to the system (A.1), is given a special name - the *elimination method*. The coefficients α_i and β_i are called the *elimination coefficients*, formulas (A.9) describe the *forward elimination path*, and (A.8) the *backward path*. Since the values y_i are found

sequentially in reverse order, the formulas (A.8)-(A.9) are sometimes called the *right-elimination formulas*.

An elementary count of the arithmetic operations in (A.8)-(A.9) shows that realizing the elimination method using these formulas requires $3N$ multiplications, $2N + 1$ divisions and $3N$ additions and subtractions. If there is no difference between arithmetic operations, the total number of operations required for the elimination method is $Q = 8N + 1$. Of this total, $3N - 2$ operations are used for computing α_i , and $5N + 3$ operations for computing β_i and y_i .

Notice that the coefficients α_i do not depend on the right-hand side of the system (A.1), but are determined solely by the coefficients a_i, b_i, c_i of the difference equations. Therefore, if we must solve a series of problems (A.1) with different right-hand sides, but with the same matrix \mathbf{A} , then the elimination coefficients α_i are only computed for the first problem of the series. Thus solving the first problem in the series costs $Q = 8N + 1$ operations, but solving each of the remaining problems only costs $5N + 3$ operations.

In conclusion, we indicate the order of the computations for the formulas of the elimination method. Beginning with α_1 and β_1 , we calculate and store α_i and β_i using (A.9). Then the solutions y_i are found using (A.8).

APPENDIX B

THE CYCLIC ELIMINATION METHOD

Let us consider the following system,

$$-a_i y_{i-1} + c_i y_i - b_i y_{i+1} = f_i, \quad i = 0, \pm 1, \pm 2, \dots, \quad (\text{B.1})$$

the coefficients and right-hand side of which are periodic with period N :

$$a_i = a_{i+N}, \quad b_i = b_{i+N}, \quad c_i = c_{i+N}, \quad f_i = f_{i+N}. \quad (\text{B.2})$$

Systems of the type (B.1), (B.2) arise, for example, from three-point difference schemes designed to find periodic solutions of second-order ordinary differential equations, and also when approximating the solutions of equations with partial derivatives in Cylindrical bipolar coordinate,

A solution of the system (B.1) satisfying the conditions (B.2) will, if it exists, also be periodic with period N , i.e.,

$$y_i = y_{i+N}. \quad (\text{B.3})$$

Therefore it is sufficient to find the solution at, for example, $i = 0, 1, \dots, N - 1$.

In this case, the problem (B.1)-(B.3) can be written as:

$$-a_0 y_{N-1} + c_0 y_0 - b_0 y_1 = f_0, \quad i = 0 \quad (\text{B.4})$$

$$-a_i y_{i-1} + c_i y_i - b_i y_{i+1} = f_i, \quad 1 \leq i \leq N - 1,$$

$$y_N = y_0. \quad (\text{B.5})$$

We have appended the condition (B.5) to the system (B.4) so that the equations for $i = N - 1$ would not include y_N , it having been replaced by y_0 . This allows us to retain a unique form for the equations (B.4) for $i = 1, 2, \dots, N - 1$.

If we introduce the vector of unknowns $Y = (y_0, y_1, \dots, y_{N-1})^T$ and the right-hand side $F = (f_0, f_1, \dots, f_{N-1})^T$, then (B.4)-(B.5) can be written in the vector form $\mathbf{A}Y = F$ where

$$\mathbf{A} = \begin{pmatrix} c_0 & -b_0 & 0 & 0 & \cdots & 0 & 0 & -a_0 \\ -a_1 & c_1 & -b_1 & 0 & \cdots & 0 & 0 & 0 \\ 0 & -a_2 & c_2 & -b_2 & \cdots & 0 & 0 & 0 \\ \cdot & \cdot & \cdot & \cdot & \cdots & \cdot & \cdot & \cdot \\ 0 & 0 & 0 & 0 & \cdots & c_{N-3} & -b_{N-3} & 0 \\ 0 & 0 & 0 & 0 & \cdots & -a_{N-2} & c_{N-2} & -b_{N-2} \\ -b_{N-1} & 0 & 0 & 0 & \cdots & 0 & -a_{N-1} & c_{N-1} \end{pmatrix}$$

is the matrix of the system (B.4), (B.5). The presence of the non-zero coefficients a_0 and b_{N-1} in (B.4) does not allow us to solve this system using the elimination method described in the previous section. To find the solution of the system (B.4), (B.5) we construct a variant of the elimination method called the *cyclic elimination method*

The solution of the problem (B.4), (B.5) will be found in the form of a linear combination of the grid functions u_i and v_i

$$y_i = u_i + y_0 v_i, \quad 0 \leq i \leq N, \quad (\text{B.6})$$

where u_i is the solution of the non-homogeneous three-point boundary-value problem

$$\begin{aligned} -a_i u_{i-1} + c_i u_i - b_i u_{i+1} &= f_i, & 1 \leq i \leq N-1, \\ u_0 &= 0, \quad u_N = 0 \end{aligned} \quad (\text{B.7})$$

with homogeneous boundary conditions, and v_i is the solution of the homogeneous three-point boundary-value problem

$$\begin{aligned} -a_i v_{i-1} + c_i v_i - b_i v_{i+1} &= f_i, & 1 \leq i \leq N-1, \\ v_0 &= 1, \quad v_N = 1 \end{aligned} \quad (\text{B.8})$$

with non-homogeneous boundary conditions.

We now find under what conditions y_i from (B.6) is the desired solution. Multiplying (B.8) by y_0 , adding it to (B.7), and taking into account (B.6), we find that the equations in (B.4) can be satisfied for $i = 1, 2, \dots, N - 1$. From the boundary conditions for u_i and v_i it follows that (B.5) will be satisfied. Thus, if y_i satisfied the remaining unused equation at $i = 0$ in (B.4), the problem would be solved. Substituting (B.6) in this equation, we obtain

$$-a_0u_{N-1} - a_0y_0v_{N-1} + c_0y_0 - b_0u_1 - b_0y_0v_1 = f_0. \quad (\text{B.9})$$

Thus, if we choose y_0 from the formula

$$y_0 = \frac{f_0 - a_0u_{N-1} + b_0u_1}{c_0 - a_0v_{N-1} - b_0v_1}, \quad (\text{B.10})$$

then (B.9) will be satisfied, and consequently the solution of the problem (B.4), (B.5) can be found from (B.6).

We are left with solving (B.7) and (B.8). They are particular cases of the three-point systems of equations solved in the previous section using the elimination method. For (B.7) and (B.8), the elimination formulas have the following form:

$$\begin{aligned} u_i &= \alpha_{i+1}u_{i+1} + \beta_{i+1}, & i &= N - 1, N - 2, \dots, 1, & u_N &= 0, \\ v_i &= \alpha_{i+1}v_{i+1} + \gamma_{i+1}, & i &= N - 1, N - 2, \dots, 1, & v_N &= 1, \end{aligned} \quad (\text{B.11})$$

where the elimination coefficients α_i, β_i and γ_i are found from the following formulas

$$\alpha_{i+1} = \frac{b_i}{c_i - a_i\alpha_i}, \quad i = 1, 2, \dots, N, \quad \alpha_1 = 0, \quad (\text{B.12})$$

$$\beta_{i+1} = \frac{f_i + a_i\beta_i}{c_i - a_i\alpha_i}, \quad i = 1, 2, \dots, N, \quad \beta_1 = 0, \quad (\text{B.13})$$

$$\gamma_{i+1} = \frac{a_i\gamma_i}{c_i - a_i\alpha_i}, \quad i = 1, 2, \dots, N, \quad \gamma_1 = 1, \quad (\text{B.14})$$

Let us transform (B.10). From (B.11) we obtain $u_{N-1} = \alpha_N u_N + \beta_N = \beta_N$, $v_{N-1} = \gamma_N + \alpha_N$. We substitute these expressions in (B.10) and take into account (B.2), (B.12)-(B.14):

$$y_0 = \frac{f_N + a_N \beta_N + \beta_N u_1}{c_N - a_N \alpha_N - a_N \gamma_N - b_N v_1} = \frac{\beta_{N+1} + \alpha_{N+1} u_1}{1 - \gamma_{N+1} - \alpha_{N+1} v_1}.$$

We have constructed an algorithm for solving problem (B.4), (B.5) called the method of cyclic elimination:

$$\begin{aligned} \alpha_2 &= b_1/c_1, & \beta_2 &= f_1/c_1, & \gamma_2 &= a_1/c_1, \\ \alpha_{i+1} &= \frac{b_i}{c_i - a_i \alpha_i}, & \beta_{i+1} &= \frac{f_i + a_i \beta_i}{c_i - a_i \alpha_i}, & \gamma_{i+1} &= \frac{a_i \gamma_i}{c_i - a_i \alpha_i}, \quad i = 2, 3, \dots, N; \\ u_{N-1} &= \beta_N, & v_{N-1} &= \gamma_N + \alpha_N, \\ u_i &= \alpha_{i+1} u_{i+1} + \beta_{i+1}, & v_i &= \alpha_{i+1} v_{i+1} + \gamma_{i+1}, \quad i = N-2, N-3, \dots, 1; \\ y_0 &= \frac{\beta_{N+1} + \alpha_{N+1} u_1}{1 - \gamma_{N+1} - \alpha_{N+1} v_1}, & y_i &= u_i + y_0 v_i, \quad i = 1, 2, \dots, N-1. \end{aligned} \tag{B.15}$$

An elementary computation indicates that the algorithm requires $6(N-1)$ multiplications, $5N-3$ additions and subtractions, and $3N+1$ divisions. If no distinction is made among arithmetic operations, the total number is $Q = 14N - 8$.

CURRICULUM VITAE

NAME: Jakgrit Sompong. **GENDER:** Male. **NATIONALITY:** Thai.

DATE OF BIRTH: September 22, 1977. **MARITAL STATUS:** Married.

EDUCATIONAL BACKGROUND:

- B.Sc. in Mathematics, Chiang Mai University, Chiang Mai, Thailand, 2000.
- M.Sc. in Mathematics, Chiang Mai University, Chiang Mai, Thailand, 2003.

WORK EXPERIENCE:

- Lecturer in Mathematics Department, Naresuan University, Phitsanulok, Thailand since 2003.
- J. Sompong and N.P. Moshkin, "A numerical study of the flow and heat transfer around two rotating circular cylinders in side-by-side arrangements", The 13th Annual National Symposium on Computational Science and Engineering, 2009, Kasetsart University, Bangkok, Thailand.

SCHOLARSHIPS:

- The Ministry of University Affairs of Thailand (MUA), 2004-2006.